TECHNISCHE
UNIVERSITÄT
WIEN
Vienna University of Technology

Diese Dissertation haben begutachtet:

_____   _____
Prof. Dr. Kai-Thomas Brinkmann   Prof. Dr. Nikolaos Mavromatos

DISSERTATION

Test of the Pauli Exclusion Principle for Electrons in the Gran Sasso Underground Laboratory

Ausgeführt zum Zwecke der Erlangung des akademischen Grades eines Doktors der technischen Wissenschaften unter Leitung von

Priv.-Doz. Dr. Johann Marton
Stefan-Meyer-Institut für subatomare Physik
der Österreichischen Akademie der Wissenschaften
und Atominstitut der Technischen Universität Wien

eingereicht an der Technischen Universität Wien Fakultät für Physik

von
Dipl.Ing. Andreas Pichler
Matr.-Nr. 00442851
Keramikstrasse 459, 3511 Furth

_____   _____
Ort, Datum   Unterschrift

There is nothing like looking,
if you want to find something.
You certainly usually find something, if you look,
but it is not always quite the something you were after.

- Thorin Oakenshield, The Hobbit

Kurzfassung

Das Pauli-Prinzip ist ein fundamentales Gesetz in der Physik, welches das Verhalten von fermionischen Teilchen bestimmt. Wegen seiner Wichtigkeit muss es so präzise wie möglich getest werden. In einem bahnbrechendem Experiment haben Ramberg und Snow einen elektrischen Strom durch ein Kupfertarget geleitet, und haben nach Pauli-Prinzip verletzenden atomaren Übergängen von "neuen" Elektronen des elektrischen Stroms gesucht. Da diese Übergänge nur erwartet werden wenn der Strom an ist, kann man mit Hilfe der Differenz der Spektren mit und ohne Strom ein oberes Limit für die Wahrscheinlichkeit einer Verletzung des Pauli-Prinzips bestimmen. Das Experiment hat nach verbotenen Kα Übergängen gesucht, welche eine etwas niedrigere Übergangsenergie aufweisen als normale Übergänge. Dadurch können Photonen von diesen verbotenen Übergängen aufgrund ihrer Energie identifiziert werden. Das VIP (VIolation of the Pauli Priniciple) Experiment konnte mit dieser Methode ein verbessertes oberes Limit für die Wahrscheinlichkeit der Verletzung des Pauli-Prinzips von 4.7×10^{-29} angeben. Das VIP2 Experiment hat zum Ziel, diese Limit zu senken, indem wichtige Komponenten des Experiments verbessert werden.

Die zentrale Komponente des VIP2 Setups sind Silizium Drift Detektoren (SDDs), welche Photonen von möglichen verbotenen Übergängen detektieren. Diese Detekoren wurden im Labor des Stefan-Meyer-Instituts getestet, zusammen mit der für die Erzeugung der Betriebstemperatur der Detektoren von 100 K notwendigen Argon Kühlung. Ihre Energie- und Zeitauflösung wurde während dieser Tests bestimmt. Eine andere zentrale Komponente des Setups sind 32 Plastikszintillatoren, die jeweils von zwei Silizium Photoelektronenvervielfachern ausgelesen werden. Die Zeitauflösung diese Systems wurde bestimmt. Die Plastikszintillatoren wurde um die SDDs montiert, um Events in den SDDs, welche von externer Strahlung verursacht werden, aussortieren zu können. Die Detektionwahrscheinlichkeit dieses aktiven Vetos für 500 MeV Elektronen wurde an der Beam Test Facility am Laboratori Nazionali di Frascati (LNF) getestet. Ausserdem wurde die Detektionwahrscheinlichkeit für kosmische Strahlung am Stefan-Meyer-Institut untersucht.

Nach diesen Tests wurde das Setup in das Gran Sasso Untergrundlabor (LNGS) in Italien gebracht. Dort wurden von Februar 2016 bis November 2017 Daten genommen. Es wurden ungefähr 142 Tage ohne Strom und 81 Tage mit 100 A Strom aufgenommen. Der Vergleich der Daten mit Geant4 Simulationen zeigte, dass ein Großteil des Backgrounds durch γ Strahlung von radioaktiven Isotopen aus dem Gestein der umgebenden Berge kommt. Die Energieauflösung der SDDs um 8 keV, wo die Pauli-Prinzip verletzenden Übergänge erwartet werden, wurde

für die Spektren mit und ohne Strom gemessen. Verschiedene Analysetechniken wurde angewendet, um die Wahrscheinlichkeit einer Verletzung des Pauli-Prinzips aus der Differenz der Spektren mit und ohne Strom zu errechnen. Diese beinhalten die Standard Technik des Subtraktion der Spektren, einen simultanen Fit der beiden Spektren und Techniken aus der Bayes Statistik. Aus der Subtraktion der Spektren im Energiebereich des verbotenen Übergangs folgt ein neues oberes Limit für die Wahrscheinlichkeit einer Verletzung des Pauli-Prinzips für Elektronen von 1.87×10^{-29}. Das ist eine Verbesserung im Vergleich mit dem VIP Experiment um einen Faktor 2.5.

Abstract

The Pauli Exclusion Principle (PEP) is a fundamental principle in physics, governing the behavior of fermionic particles. Due to its importance, it needs to be tested as precisely as possible. In a pioneering experiment, Ramberg and Snow supplied an electric current to a Cu target, and searched for PEP violating atomic transitions of "fresh" electrons from the current. As these transitions are only expected when the current is on, the difference between the spectra with and without current can be used to set an upper limit for the probability for the violation of the PEP. Specifically, the experiment searched for forbidden Kα transitions, which have a slightly lower transition energy than the normal transitions. Photons from these transitions can therefore be distinguished by their energy. The VIP (VIolation of the Pauli Exclusion Principle) experiment could set this upper limit to 4.7 $\times$ 10^{-29} with the described method. The VIP2 experiment wants to improve this limit by upgrading crucial components of the setup.

The central component of the VIP2 setup are the Silcion Drift Detectors (SDDs) which record possible photons from PEP violating transitions. These detectors were tested in the laboratory of the Stefan Meyer Institute together with argon cooling, which keep the working temperature at around 100 K. Their energy and time resolution were assessed during these tests. Another essential component of the setup are the 32 plastic scintillator bars read out by two Silicon Photo Multipliers each. The time resolution of this system was successfully tested. It was installed to veto events in the SDDs caused by external ionizing radiation. The detection probability of this active veto for 500 MeV electrons was tested at the beam test facility at Labroratori Nazionali di Frascati (LNF). Furthermore, the detection probability for cosmic radiation was assessed at the Stefan Meyer Institute (SMI).

After exhaustive tests, the setup was transported to the underground laboratory of Gran Sasso (LNGS). Data was taken from February 2016 until November 2017. An amount of approximately 142 days of data without current and 81 days with 100 A current were taken. Comparison of the data to Geant4 simulations showed that the majority of the background is induced by γ radiation originating from radioactive isotopes of the rocks of the mountain. The energy resolution around 8 keV, where events from the PEP-violating transition are expected, was measured for the spectra with and without current. Several analysis techniques for investigating the difference of the two energy spectra, and calculating the probability for a violation of the Pauli Exclusion Principle, were applied. These include the standard technique of spectral subtraction, a simultaneous fit of both spectra and methods using Bayesian statistics. The standard analysis of subtraction of the

spectra in a region of interest defined around the expected energy of the forbidden transition yields a new upper limit of 1.87×10^{-29}. This is an improvement to the value set by the VIP experiment by a factor of 2.5.

Acknowledgement

A big thanks also belongs to my friends here at the Stefan Meyer Institute. I want to thank: Sebastian L., Bernadette, Aaron, Lukas, Stefan, Dominik, Manfred, Sebastian Z., Carina, Markus, Daniel, Martin, Amit etc. Thank you for all those long conversations, the nights spent playing Nintendo 64 (sorry for always beating you - not!) and drinking beer, the proofreading of important documents, the help with physics and programming problems and all the life advice. I am going to miss all of you! Also I want to thank the staff of the Stefan Meyer Institute like: Doris, Leo, Mark, Herbert, Julia, Fiona and Peter for all their help and advice.

Last but definitely not least I wish to thank my family, who supported me financially and emotionally through all my life. I will never be able to express my gratitude with words. I want to specifically mention my nephew Paul and my niece Emma, who have the gift of always making me smile when nobody else can.

Contents

1. Introduction

The Pauli Exclusion Principle (PEP) is a fundamental principle in physics, valid for identical-fermion systems. It was formulated in 1925 by the austrian physicist Wolfgang Pauli. It states that two fermions (particles with half integer spin) can not occupy the same quantum state simultaneously. Examples of fermionic particles are elementary particles such as quarks, leptons (electron, muon and tauon) and neutrinos. Composite particles can also be fermions (e.g. protons and neutrons). Electrons, which make up the electronic shell of atoms, are fermions and therefore obey the PEP. For the case of electronic shells, the PEP is equivalent to the statement that two electrons cannot have the same principal quantum number n, angular momentum quantum number l, magnetic quantum number m_l and spin quantum number m_s at the same time. This means that two electrons can share the quantum numbers n, l and m_l, as long as they have different spin quantum number m_s ($\pm$ ½).

The PEP forms the basis of the periodic table of elements, as it prevents all electrons in a shell to condense into the ground state. Therefore, it is responsible for the occupation of the electronic shells and the chemical properties of elements. It also stabilizes neutron stars, as the neutron degeneracy pressure, which is caused by the PEP, prevents them from collapsing under their own gravitational pressure.

Due to the fundamental place of the PEP in quantum field theory, many researches were interested in testing it. In the year 1948, the PEP was tested by Goldhaber and Scharff-Goldhaber [1]. Their experiment was designed to determine if the particles making up β radiation were the same as electrons, but it was later interpreted as a test of the Pauli Exclusion Principle. The experiment was done by shining electrons from a β source onto a block of lead. The authors thought, if these β particles were different from electrons, they could be captured by the lead atoms and cascade down to the ground state without being subject to the PEP. The non-existence of X-rays emitted during this cascading process was used to set an upper bound for the probability that the PEP is violated. Another test was conducted in 1988 by E. Ramberg and G. A. Snow [2]. They introduced a current into a copper conductor. The electrons of the current then had a chance to be

captured by the copper atoms and form a new quantum state. The experimenters searched for states having a symmetric component in an otherwise antisymmetric state. These states were identified by the X-rays they emitted during de-excitation to the ground state. Photons from these forbidden transitions were identified by their energy, which is slightly shifted with respect to normal transitions. The same principle was later employed in the VIP experiment, which was able to set a new upper limit for the probability for the violation of the Pauli Exclusion Principle (parametrized in the literature by $\frac{\beta^2}{2}$) of

$$\frac{\beta^2}{2} \leq 4.7 * 10^{-29}$$

([3], [4]). The follow-up experiment VIP2 was taking data in the Laboratori Nazionali del Gran Sasso (LNGS) from February 2016 until November 2017 and is currently (February 2018) undergoing maintenance.

This thesis is organised in the following way. The next chapter 2 explains the physics of the VIP2 experiment. It includes a short explanation of spin and fermionic and bosonic statistics, as well as the indistinguishability of identical particles and its consequences. Furthermore, theories for the violation of Spin-Statistics will be presented and tests of the PEP will be categorized and explained. In chapter 3, the VIP2 measurement setup will be explained in detail. This includes an explanation of the Silicon Drift Detectors (SDDs) as well as the active shielding system. In chapter 4 follows an analysis of the results of Geant4 simulations. Here, the expected background from γ radiation and from cosmic muons are evaluated. Furthermore, the detection efficiency for photons from PEP-violating transitions is calculated.

In chapter 5, the test measurements at Laboratori Nazionali di Frascati and at the Stefan Meyer Institute are described. Results are presented for the energy and time resolution of the SDDs and the detection probability of cosmic radiation of the active shielding, among other things. The following chapter 6 gives details about the data taking at LNGS and explains the procedure to arrive at the final SDD energy spectra with and without current. Here, the core part is the energy calibration procedure from ADC channels into electronvolts. Finally in chapter 7, four different methods are described for calculating a new upper limit for the probability of a violation of the PEP from these spectra. In chapter 8, important results are summed up and a short outlook is given.

2. Physics of the VIP2 experiment

2.1. Physics Basics

2.1.1. The Pauli Exclusion Principle

To explain the spectra of alkali atoms recorded with a magnetic field (Zeemann effect), Wolfgang Pauli postulated a 4th quantum number for electrons in the early 1920s. The new quantum number was an addition to the quantum numbers already known at that time, which are nowadays called the principal quantum number n, the angular momentum quantum number l and the magnetic quantum number m_l. He named it a "two-valuedness not describable classically" [5]. This 4th quantum number was later called the electron's spin. Another problem he was working on at that time was the series of integer numbers 2, 8, 18, 32, etc., which was determining the lengths of the lines in what we call the periodic table of elements. Furthermore, it was known to him that the number of electronic energy levels in an alkali atom were the same as the number of electrons in the closed shell of the rare gas with the same principal quantum number. He used this information to formulate the Pauli Exclusion Principle: The number of electrons in closed subgroups can be reduced to one, if the division of the groups (by giving them values of the four quantum numbers) is carried so far that every degeneracy is removed. An entirely non-degenerate level is closed, if it is occupied by a single electron [5]. This is equivalent to saying that every state corresponding to a set of quantum numbers n, l, m_l and m_s can only be occupied by one electron. Wolfgang Pauli won the Nobel Prize in physics for the formulation of the Pauli Exclusion Principle in 1945. It was first formulated for electrons, but later on extended to all fermions.

2.1.2. Quantum Mechanical Angular Momenta

From a classical point of view, angular momentum is defined as: $\vec{L} = \vec{r} \times \vec{p}$, where $\vec{L}$ is the angular momentum, $\vec{r}$ is the vector to the particle from the origin and $\vec{p}$

is the momentum of the particle. The magnetic moment of a particle with charge q moving in a circle with radius r is defined as $\mu = I\, A$. Here μ is the magnetic moment, $A = r^2\pi$ is the area that the particle's movement is encircling and I is the current. The current the particle generates can be written as

$$I = \frac{q}{T} = \frac{q}{\frac{2r\pi}{v}} = \frac{qv}{2r\pi}, \tag{2.1}$$

where v is the particle's velocity and T is the time it needs for one full circle. The magnetic moment can be written as

$$\mu = IA = \frac{qv}{2r\pi}r^2\pi = \frac{qvr}{2} = \frac{q}{2m}rvm = \frac{q}{2m}L, \tag{2.2}$$

where $\frac{q}{2m} = \frac{\mu}{L}$ is called the gyromagnetic ratio. For electrons formula 2.2 is often rewritten in the form

$$\mu_e = g\mu_B\frac{L}{\hbar} \quad \text{with} \quad \mu_B = \frac{e\hbar}{2m_e}, \quad \hbar = 1.054571800(13) \times 10^{-34}[\frac{\text{m}^2\ \text{kg}}{\text{rad s}}], \tag{2.3}$$

where μ_e is the magnetic moment of the electron, m_e is the electron mass and μ_B is the Bohr magneton. The Bohr magneton is the expected ratio between the magnetic moment μ_e and the dimensionless value $\frac{L}{\hbar}$. The *g-factor* parametrizes deviations from the expected value $g = 1$, which could arise if, for example for an arbitrary distribution of electrons, the charge density distribution is different from the mass density distribution.

In analogy to classical mechanics, the angular momentum can be written in quantum mechanics as a cross product of the position operator $\hat{x}$ and the momentum operator $\hat{p}$: $\hat{L} = \hat{x} \times \hat{p}$. In position basis this can be written as

$$\hat{L} = \hat{x} \times \hat{p} = \frac{\hbar}{\imath}(\vec{x} \times \vec{\nabla}) \quad \text{with} \quad \vec{\nabla} = \begin{pmatrix} \frac{\partial}{\partial x} \\ \frac{\partial}{\partial y} \\ \frac{\partial}{\partial z} \end{pmatrix}. \tag{2.4}$$

In index notation, this operator can be written as follows: $\widehat{L}_i = \epsilon_{ijk}\widehat{x_j}\widehat{p_k}$ with ϵ_{ijk} being the antisymmetric Levi-Civita tensor. The indices i, j, k correspond to the three spatial dimensions. $\widehat{L}_i$ and $\widehat{L}_j$ do not commute as

$$[\widehat{L}_i, \widehat{L}_j] = \imath\hbar\epsilon_{ijk}\widehat{L}_k \quad \text{with} \quad [\widehat{X}, \widehat{Y}] = \widehat{X}\widehat{Y} - \widehat{Y}\widehat{X}. \tag{2.5}$$

Here $[\widehat{X}, \widehat{Y}]$ denotes the commutator of $\widehat{X}$ and $\widehat{Y}$. For readability, the hats of operators will be omitted from now on. The entries L_i of the angular momentum

operator commute with the rotationally invariant form $L^2 = L_x^2 + L_y^2 + L_z^2$. This operator is the squared norm of the angular momentum. Since L_i and L^2 commute, they can be measured simultaneously. This also means that

$$[L_i, L^2] = 0. \tag{2.6}$$

For any given system, the following relations for the eigenvalues of these operators hold:

$$L_i \, |\phi\rangle = \hbar m_l \, |\phi\rangle \qquad m_l \in \dots -2, -1, 0, 1, 2, \dots \quad , \tag{2.7}$$

$$L^2 \, |\phi\rangle = \hbar^2 l(l+1) \, |\phi\rangle \qquad l \in 0, 1, 2, \dots \tag{2.8}$$

with $|m_l| \leq l$. Considering particles without spin and a Hamiltonian symmetric under rotations of the form $H = \frac{p^2}{2m} + V(r)$ (like the hydrogen atom), the angular momentum is conserved and commutes with the Hamiltonian

$$[H, L_i] = [H, L^2] = [L_i, L^2] = 0. \tag{2.9}$$

Therefore, L_i and L^2 are conserved quantities. For systems without spin, H, L^2 and L_i form a complete set of commuting observables with the corresponding quantum numbers n (principal quantum number), l (angular momentum quantum number) and m_l (magnetic quantum number). Introducing the rotationally invariant Coulomb potential $V(r)$ of a positive point charge q

$$V(r) = \frac{1}{4\pi\epsilon_0} \frac{q}{r}, \tag{2.10}$$

one finds that angular momentum quantum number l always needs to be smaller than the principal quantum number n ($l < n$). Only considering a pure Coulomb interaction, the eigenstates with principal quantum number n belonging to the eigenvalue E_n are n^2-fold degenerate.

2.1.3. The Spin

The spin is an intrinsic type of angular momentum carried by most elementary particles. It has a definitive and non-modifiable magnitude for each particle type. This is in contrast to the section 2.1.2, where the angular momenta, described by the quantum number l, could change in magnitude. Wolfgang Pauli was the first to propose the concept of a "two-valuedness not describable classically", which would later be identified as spin. Analogous to the relation between angular momentum and magnetic moment 2.3, the relation between spin and magnetic moment can

be written as

$$\mu_s = g\mu_B \frac{S}{\hbar} \quad \text{with} \quad \mu_B = \frac{e\hbar}{2m}, \tag{2.11}$$

where μ_s is the magnetic moment of a particle due to its spin and S is the magnitude of this spin. Unlike for angular momenta described in 2.1.2, the value for $g \neq 1$. From the Dirac equation, a value of $g = 2$ can be obtained. Corrections for example from Quantum Electrodynamics further alter this value on the %-level.

Analogous to equations 2.5 and 2.6, commutation relations can be derived for the spin:

$$[S_i, S_j] = \imath\hbar\epsilon_{ijk}S_k, \tag{2.12}$$

$$[S_i, S^2] = 0, \tag{2.13}$$

where S_i are the spin components in the three spatial directions and S^2 is the squared norm of the spin. Furthermore, analogous to equations 2.7 and 2.8, the following relations hold for the spin:

$$S^2 \ket{\phi} = \hbar^2 s(s+1) \ket{\phi} \qquad s \in 0, \frac{1}{2}, 1, ... \ , \tag{2.14}$$

$$S_i \ket{\phi} = \hbar m_s \ket{\phi} \qquad \mid m_s \mid \leq s, \tag{2.15}$$

where s is the spin quantum number and m_s is the spin projection quantum number. The big difference between s and its analogue l from section 2.1.2 is that s can also take half-integer values. Another difference is, that s, unlike l, cannot be changed and is intrinsic for each particle type. Particles with half-integer spin quantum number are called *fermions*, and particles with integer spin are called *bosons*. In particular leptons, such as electrons, have $s = \frac{1}{2}$ and therefore m_s can take the values $\pm \frac{1}{2}$. For a system containing particles with spin, n, l, m_l and m_s form a complete set of commuting observables. The total angular momentum $\vec{J}$ can be defined as the sum of the orbital angular momentum and spin $\vec{J} = \vec{L} + \vec{S}$. Analogous expressions to equations 2.5 - 2.9 hold for the total angular momentum $\vec{J}$ in systems containing particles with spin.

Considering a particle with $s = \frac{1}{2}$. The basis in which S^2 and S_z are diagonal consists of two states $\ket{s, m_s} = \ket{\frac{1}{2}, \pm\frac{1}{2}}$. These states can be identified with the basis vectors $e_1 = \begin{pmatrix} 1 \\ 0 \end{pmatrix}$ and $e_2 = \begin{pmatrix} 0 \\ 1 \end{pmatrix}$ and are often referred to as "spin-up" and "spin-down" relative to a defined z-direction. The action of operators on these states is as

$$S^2 \ket{\frac{1}{2}, \pm\frac{1}{2}} = \hbar^2 \frac{1}{2}(\frac{1}{2} + 1) \ket{\frac{1}{2}, \pm\frac{1}{2}}, \tag{2.16}$$

$$S_z \, |\tfrac{1}{2}, \tfrac{1}{2}\rangle = \hbar \tfrac{1}{2} \, |\tfrac{1}{2}, \tfrac{1}{2}\rangle, \tag{2.17}$$

$$S_z \, |\tfrac{1}{2}, -\tfrac{1}{2}\rangle = -\hbar \tfrac{1}{2} \, |\tfrac{1}{2}, -\tfrac{1}{2}\rangle, \tag{2.18}$$

$$S_+ \, |\tfrac{1}{2}, \tfrac{1}{2}\rangle = 0 \qquad S_- \, |\tfrac{1}{2}, \tfrac{1}{2}\rangle = \hbar \, |\tfrac{1}{2}, -\tfrac{1}{2}\rangle, \tag{2.19}$$

$$S_+ \, |\tfrac{1}{2}, -\tfrac{1}{2}\rangle = \hbar \, |\tfrac{1}{2}, \tfrac{1}{2}\rangle \qquad S_- \, |\tfrac{1}{2}, -\tfrac{1}{2}\rangle = 0. \tag{2.20}$$

The *ladder operators* $(S_\pm)$ were used in equations 2.19 and 2.20. A ladder operator increases (S_+) or decreases (S_-) the quantum number m_s of a state. For an angular momentum $\vec{J}$ with quantum numbers j and m_j it is defined as

$$J_\pm \, |j, m_j\rangle = \hbar \sqrt{(j \mp m_j)(j \pm m_j + 1)} \, |j, m_j \pm 1\rangle. \tag{2.21}$$

In the mentioned basis, the operators S_x, S_y and S_z can be written as

$$S_x = \frac{\hbar}{2} \begin{pmatrix} 0 & 1 \\ 1 & 0 \end{pmatrix}, \qquad S_y = \frac{\hbar}{2} \begin{pmatrix} 0 & -i \\ i & 0 \end{pmatrix}, \qquad S_z = \frac{\hbar}{2} \begin{pmatrix} 1 & 0 \\ 0 & -1 \end{pmatrix}. \tag{2.22}$$

These are the so called *Pauli matrices*.

2.1.4. Indistinguishability, Symmetrization Postulate and Superselection Rule

The following section is loosely based on [6]. Considering a state $\phi = \phi(1, 2,..., i,..., j,...N)$, where the variables 1,2,... denote the spatial and the spin degrees of freedom of N particles. The action of the permutation operator $P_{i,j}$ on this state is defined as

$$P_{i,j}\phi(1, 2, .., i, ..., j, ...N) = \phi(1, 2, .., j, ..., i, ...N). \tag{2.23}$$

The indistinguishability of identical particles implies that states that differ only by a permutation of identical particles can not be distinguished by any measurement. In quantum mechanics, a measurement is expressed as the expectation value of a

hermitian [1] operator A. This statement can be expressed for a state ϕ as

$$\langle\phi|A|\phi\rangle = \langle\phi|P^\dagger A P|\phi\rangle. \tag{2.24}$$

It follows, that the permutation operator commutes with every observable, as it holds for every state ϕ and it follows that $P^\dagger A P = A$. Therefore, $PA = AP$ which implies that the two operators commute. Specifically, the energy of a quantum mechanical system must not depend on the permutation of identical particles. From above considerations it follows that

$$[P, H] = 0, \tag{2.25}$$

where H is the Hamiltonian.

An infinitesimal time evolution δt of a state is given by the Schrödinger equation

$$\partial_t |\phi(t)\rangle = \frac{1}{\imath\hbar} H |\phi(t)\rangle \Rightarrow |\phi(t + \delta t)\rangle = (1 + \frac{\delta t}{\imath\hbar} H + O(\delta t^2)) |\phi(t)\rangle. \tag{2.26}$$

For a time-independent Hamiltonian H, $n \to \infty$ infinitesimal time steps between a start time t_0 and time t give the time evolution operator $U(t - t_0)$:

$$|\phi(t)\rangle = U(t - t_0) |\phi(t_0)\rangle \quad \text{with} \quad U(t - t_0) = e^{-\frac{\imath}{\hbar}(t - t_0)H} \tag{2.27}$$

As the permutation operator commutes with the Hamiltonian, it also commutes with the time evolution operator U:

$$[P, U] = 0, \tag{2.28}$$

because of equation 2.27. Therefore, the permutation symmetry of a state is conserved. This is called the *Messiah-Greenberg (MG) superselection rule*. It is important to note that the above considerations are only viable for systems where the number of particles is conserved and that the permutation symmetry of a system is not necessarily preserved in systems with a non-constant particle number (see for example [7]).

Considering a system of two particles, in which the state $\phi(1, 2)$ is a solution of the Schrödinger equation

$$H |\phi(1, 2)\rangle = E |\phi(1, 2)\rangle. \tag{2.29}$$

---

[1] A hermitian or self-adjoint operator is an operator for which the relation $A^\dagger = A$ holds. The hermitian conjugation † corresponds to transposition combined with complex conjugation. A hermitian operator has real eigenvalues and eigenvectors for different eigenvalues are orthogonal.

As the Hamiltonian commutes with the permutation operator, $P_{12} |\phi(1,2)\rangle = |\phi(2,1)\rangle$ is also a solution to this equation with the same Hamiltonian H and the same eigenvalue E. All linear combinations of these two functions are also solutions of the equation. The linear combinations $|\Phi\rangle = |\phi(1,2)\rangle \pm |\phi(2,1)\rangle$ represent solutions corresponding to positive (+) and negative (-) symmetry with respect to particle exchange.

The situation is a bit more complex for a system with three particles. Given the state $|\phi(1,2,3)\rangle$ solves the Schrödinger equation, the linear combination

$$|\phi(1,2,3)\rangle + |\phi(1,3,2)\rangle - |\phi(3,2,1)\rangle \tag{2.30}$$

also solves the Schrödinger equation. For an exchange of particles 1 and 2, this state becomes

$$|\phi(2,1,3)\rangle + |\phi(2,3,1)\rangle - |\phi(3,1,2)\rangle . \tag{2.31}$$

The state is not an eigenstate of the permutation operator P_{12}, as it is not the same as the one given in 2.30. Therefore, not all solutions of the Schrödinger equation need to be eigenfunctions of the permutation operator. A special case are the linear combinations with negative

$$|\phi(1,2,3)\rangle - |\phi(1,3,2)\rangle - |\phi(2,1,3)\rangle + |\phi(2,3,1)\rangle + |\phi(3,1,2)\rangle - |\phi(3,2,1)\rangle \tag{2.32}$$

and positive

$$|\phi(1,2,3)\rangle + |\phi(1,3,2)\rangle + |\phi(2,1,3)\rangle + |\phi(2,3,1)\rangle + |\phi(3,1,2)\rangle + |\phi(3,2,1)\rangle \tag{2.33}$$

symmetry with respect to particle exchange. These linear combinations are called completely antisymmetric (equation 2.32) and symmetric (equation 2.33). This means that an application of the permutation operator for any pair of particles gives a negative or positive sign for the state $P |\Phi\rangle = \pm |\Phi\rangle$.

For a general system of N particles, the symmetry of different linear combinations of wave functions are described by *Young diagrams* (see e.g. [8]). A Young diagram represents an irreducible representation of the permutation group [2]. Examples of such diagrams of the S_3 group are shown in figure 2.1. Each box of a Young diagram symbolizes a particle and the spatial relation of two boxes symbolizes the permutation symmetry of the state with respect to the exchange of the particles in the boxes. Two boxes arranged vertically represent an antisymmetric exchange symmetry and two boxes aligned horizontally correspond to symmetric exchange

---

[2]The permutation group S_N is a group whose elements are the permutations of a set with N elements.
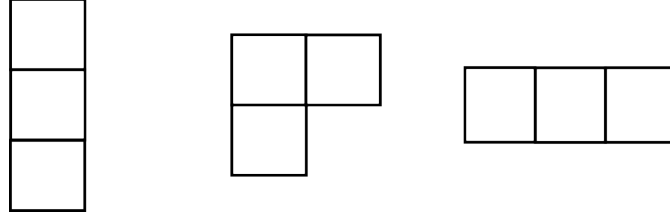
9

Figure 2.1.: Young diagrams of the S_3 permutation group for antisymmetric (left), mixed (middle) and symmetric (right) permutation symmetry.

symmetry. From the description of this kind it follows that all states described by a Young diagram are eigenstates of the permutation operator. In figure 2.1 different exchange symmetries for systems with three particles are shown. It is important to note that there is not only the completely (anti-)symmetric exchange symmetry (left/right side), but also the state with a positive symmetry for the exchange of one pair of particles and negative symmetry for another pair. This state is called a mixed-symmetry state.

The *symmetrization postulate* states that from the three different permutation symmetries in figure 2.1, only the left and the right ones are realised in nature [7]. Due to their form they are called the one-dimensional representation of the permutation group. The usual proof of this postulate is as follows:

From the indistinguishability of identical particles follows that a permutation of two particles should only multiply the wave function by an insignificant phase factor $e^{i\alpha}$ with α being a real constant:

$$P_{12} \left| \phi(1,2) \right\rangle = \left| \phi(2,1) \right\rangle = e^{i\alpha} \left| \phi(1,2) \right\rangle. \tag{2.34}$$

One more application of the permutation operator gives

$$P_{12} P_{12} \left| \phi(1,2) \right\rangle = \left| \phi(1,2) \right\rangle = e^{i\alpha} e^{i\alpha} \left| \phi(1,2) \right\rangle = e^{2i\alpha} \left| \phi(1,2) \right\rangle, \tag{2.35}$$

or

$$e^{2i\alpha} = 1 \Rightarrow e^{i\alpha} = \pm 1. \tag{2.36}$$

This proof is incorrect, as it is shown in [8]. One argument against this proof is that the indistinguishability of identical particles only requires the squared norm of the wave function to be invariant under permutations:

$$P_{12} \mid \left| \phi(1,2) \right\rangle \mid^2 = \mid \left| \phi(1,2) \right\rangle \mid^2. \tag{2.37}$$

For a function to satisfy this relation it is sufficient that it changes under permu-

tations as

$$P_{12} \left| \phi(1,2) \right\rangle = e^{\imath \alpha(1,2)} \left| \phi(1,2) \right\rangle, \tag{2.38}$$

where 1 and 2 are the space and the spin coordinates of the two particles. Thus, the phase factor can be a function of the permutation and of the coordinates. Therefore, in general, equations 2.35 and 2.36 do not hold. Consequently, the symmetrization postulate corresponds to the fact, that only the one-dimensional representations of the permutation group, meaning the fully (anti-)symmetric states, have yet been observed in nature. Nevertheless, the solution of the Schrödinger equation can belong to any representation of the permutation group, not only the one-dimensional ones.

2.1.5. Fermions, Bosons and the Spin-Statistics Connection

As mentioned in section 2.1.3, different particle types have different intrinsic spin, which cannot be altered. As was shown in 1940 by Wolfgang Pauli [9], the spin of a particle determines which of the two possible representations of the permutation group it belongs to.

Particles with integer spin ($s = 0,1,2, ...$) have symmetric wave functions with respect to particle exchange. These particles are called *bosons* (after Indian physicist Satyendra Nath Bose). Their corresponding Young diagram is of the type on the right side of figure 2.1. Elementary bosonic particles are, for example, the force carrier particles of the strong, weak and electromagnetic interactions: the gluon, the W and Z bosons and the photon. Another example of an elementary boson is the Higgs particle. Composite bosons can be made up out of particles with half integer or with integer spin. An example of a composite boson are mesons, which are made up out of a quark and an antiquark with $s = \frac{1}{2}$ each.

The occupation number of bosons follows the Bose-Einstein statistics. The expected number of particles in an energy state is in this case:

$$N(E) = \frac{1}{e^{\frac{E-\mu}{kT}} - 1}, \tag{2.39}$$

where E is the energy of the state, μ is the chemical potential, k is the Boltzmann constant and T is the absolute temperature. A consequence of this statistics is that more than one bosonic particle can occupy the same quantum state. The commutation relations of creation ($a^\dagger$) and annihilation (a) operators for bosonic

particles in states X and Y are:

$$[a_X, a_Y] = 0, \qquad [a_X^\dagger, a_Y^\dagger] = 0, \qquad [a_X, a_Y^\dagger] = \delta_{X,Y}. \tag{2.40}$$

Particles with half-integer spin ($s = \frac{1}{2}, \frac{3}{2}, ...$) have antisymmetric wave functions with respect to particle exchange. Therefore, changing the position of two particles multiplies the wave function with a minus sign. These particles are called *fermions* (after the italian physicist Enrico Fermi). Their corresponding Young diagram is of the type on the left side of figure 2.1. Fermions can be elementary particles like quarks and leptons (e.g. electrons), but also composite particles like neutrons, protons or even atoms.

The occupation number of fermions follows the Fermi-Dirac statistics. The expected number of particles in an energy state is in this case:

$$N(E) = \frac{1}{e^{\frac{E-\mu}{kT}} + 1}. \tag{2.41}$$

As the exponential function is always positive, the expected occupation number is always smaller or equal to one. This means that any energy state can only be occupied by one fermion. This is known as the *Pauli Exclusion Principle* (see also section 2.1.1).

Furthermore, it can be seen that particles with purely fermionic exchange symmetry cannot be in the same state by considering a system consisting of two fermionic particles with two possible states. The unnormalized antisymmetric wave function is:

$$|\Phi_a\rangle = |\phi(1,2)\rangle - |\phi(2,1)\rangle. \tag{2.42}$$

The wave function for the two fermionic particles being in the same state is (in this case in state 1):

$$|\Phi_a\rangle = |\phi(1,1)\rangle - |\phi(1,1)\rangle = 0. \tag{2.43}$$

So the antisymmetric wave function of two particles being in the same state is equal to zero. Therefore, two fermionic particles can not be in the same state.

The anticommutation relations of creation ($a^\dagger$) and annihilation (a) operators for fermionic particles in states X and Y are:

$$\{a_X, a_Y\} = 0, \qquad \{a_X^\dagger, a_Y^\dagger\} = 0, \qquad \{a_X, a_Y^\dagger\} = \delta_{X,Y}. \tag{2.44}$$

From 2.44 it can be seen that adding or removing two particles from a state results in zero (as for example $\{a_X, a_Y\} = a_X a_Y + a_Y a_X = 0$). Consequently, not more

than one particle can be in a given state for fermions. The action of these operators for fermionic particles on the unoccupied vacuum state $|0\rangle$ and the state occupied by one particle $|1\rangle$ can be written as

$$a\,|0\rangle = 0, \qquad a\,|1\rangle = |0\rangle\,, \qquad a^\dagger\,|0\rangle = |1\rangle\,, \qquad a^\dagger\,|1\rangle = 0. \qquad (2.45)$$

The relation described above between a particle's spin and its statistics is called the *Spin-Statistics connection*.

In the literature many proofs for the Spin-Statistic connection exist (e.g. [9], [10]). A clear set of assumptions for this proof was presented by Lüders and Zumino in [11]. The authors present five postulates plus gauge invariance as a foundation of their proof:

- Invariance with respect to the proper inhomogeneous Lorentz group (which contains translations, but no reflections)

- Locality: two operators of the same field separated by a spacelike interval either commute or anticommute

- The vacuum is the state of the lowest energy

- The metric of the Hilbert space is positive definite

- The vacuum is not identically annihilated by a field

It is worth noting that the mentioned proof also holds for interacting fields. Another interesting point is that the Spin-Statistics connection does not hold for two spatial dimensions. The concept of *anyons*, a class of particles which does not follow bosonic or fermionic statistics, was presented in [12] in this context.

2.2. Theories of Violation of Spin-Statistics

There have been many attempts to find a theory of quantum mechanics which is consistent with a violation of Spin-Statistics. Some of the most important ones will be discussed in the following section.

2.2.1. Parastatistics

The first proper quantum statistical generalization of Fermi and Bose statistics was done by Green [13], [14]. He noticed that the commutator of the occupation number operator of the state X, defined as $N_X = a_X^\dagger a_X$ with the annihilation and creation operators is the same for fermions and bosons:

$$[N_X, a_Y^\dagger] = \delta_{X,Y}\, a_Y^\dagger. \tag{2.46}$$

As a result, the number operator can be written as

$$N_X = \frac{1}{2}[a_X^\dagger, a_X]_\pm + const. \tag{2.47}$$

The $\pm$ sign denotes the (anti-)commutator for the (bosonic) fermionic case. The expression for the transition operator $N_{X,Y}$, which annihilates a particle in state Y and creates a particle in state X, leads to the trilinear commutation relation [3] for parabose and parafermi statistics:

$$[[a_X^\dagger, a_Y]_\pm, a_Z^\dagger] = 2\,\delta_{Y,Z}\, a_X^\dagger. \tag{2.48}$$

These relations have an infinite set of solutions, each of them corresponding to an integer p. The integer p is the order of the parastatistics and gives the number of particles that can be in an antisymmetric state in the case of parabosons and the number of particles that can be in a symmetric state in case of parafermions. The case $p = 1$ corresponds to normal fermionic or bosonic statistics. It was shown that the squares of all norms are positive for states satisfying Green's trilinear commutation relation. Nevertheless, the violations introduced by these statistics is large and no precision experiments are needed to rule them out.

2.2.2. The Ignatiev and Kuzmin Model and Parons

In 1987, A. Ignatiev and V. Kuzmin constructed a model of one oscillator with three possible states: a vacuum state with no occupancy, a one particle state and, with a small amplitude parametrized by β, a state occupied by two particles [15]. The creation and annihilation operators connect these three states (analogous to 2.45) as:

$$a\,|0\rangle = 0, \quad a\,|1\rangle = |0\rangle, \quad a\,|2\rangle = \beta\,|1\rangle, \tag{2.49}$$

---

[3]A trilinear form is a function of three arguments, in which every argument enters only to first order.

$$a^\dagger \ket{0} = \ket{1}, \quad a^\dagger \ket{1} = \beta \ket{2}, \quad a^\dagger \ket{2} = 0. \tag{2.50}$$

They were able to give trilinear commutation relations for these oscillators. It is worth noting that the authors calculated that the oscillations violating the PEP are suppressed by a factor proportional to β^2 compared to oscillations that do not violate the PEP. These oscillations vanish for $\beta = 0$. Following these ideas, Mohapatra and Greenberg ([14]) described this model as a modified version of the order-two Green ansatz. They introduced a parameter β giving a deformation of Green's trilinear commutators (see 2.48). For $\beta \to 1$ the relations reduce to those of the p = 2 parafermi field. For $\beta \to 0$ on the other hand, double occupancy is completely suppressed and Fermi theory is obtained. Particles described by this theory were called *parons*. A state of two paronic electrons has the probability to be in a double occupancy state of $\frac{\beta^2}{2}$. This model is the origin of the convention in the literature to parametrize a violation of the PEP by $\frac{\beta^2}{2}$. It was shown by A. Govorkov in [16] that every alteration of Green's commutation relation (like the one discussed here) must have states with negative squared norms. Thus, the model of Igantiev and Kuzmin cannot be extended to become a true field theory [6].

2.2.3. Quons

The idea of a class of particles violating the Spin-Statistics relation called *quons* was described by O. W. Greenberg [17]. The commutator algebra of quons can be obtained as the convex sum of the Fermi and Bose commutator algebras

$$\frac{1+q}{2}[a_X, a_Y^\dagger] + \frac{1-q}{2}\{a_X, a_Y^\dagger\} = \delta_{X,Y}, \tag{2.51}$$

or

$$a_X a_Y^\dagger - q a_Y^\dagger a_X = \delta_{X,Y}. \tag{2.52}$$

In equations 2.51 and 2.52 the parameter q was introduced, which interpolates between a fermionic (q = -1) and a bosonic (q = 1) commutation relation. For the quonic states to have positive squared norms, this parameter needs to be within -1$\leq q \leq 1$. For q deviating from $\pm$ 1, the multidimensional representations of the permutation group, which correspond to Young diagrams with more than one row/column, smoothly become more heavily weighted and have a non-zero probability of being realised. That means that for a state with two particles, for which only completely symmetric and antisymmetric wave functions are possible,

a density matrix [4] can be given to represent the mixture of the possible states in the form:

$$\rho = \frac{1+q}{2} |\phi_s\rangle \langle\phi_s| + \frac{1-q}{2} |\phi_a\rangle \langle\phi_a| .$$ (2.53)

For fermionic quons, the factor q would be close to and slightly larger than -1. For bosonic quons, the factor q would be close to and slightly smaller than 1. When the theory of quonic fermions is related to paronic fermions, where the probability of a state with double occupancy is $\frac{\beta^2}{2}$, it follows that

$$\frac{\beta^2}{2} = \frac{1+q_F}{2} \Rightarrow q_F = \beta^2 - 1.$$ (2.54)

Quonic particles clearly violate the Spin-Statistics connection. It is worth noting nevertheless, that several properties of relativistic theories do hold, like the CPT theorem for example. But as the Spin-Statistics connection does hold for relativistic theories with the usual properties (see section 2.1.5), some property has to fail. This is the property of locality. It turns out that in this framework, observables separated by spacelike separation [5], do not commute.

2.3. Tests of the Pauli Exclusion Principle

2.3.1. Remarks on Testing the Pauli Exclusion Principle

Why should the PEP and thereby the Spin-Statistics connection be tested, if it can not be violated in a relativistic theory with the usual properties given in [11]. O. W. Greenberg gives in [14] several "external motivations" which could lead to a possible violation of Spin-Statistics, namely:

- violation of CPT

- violation of locality

- violation of Lorentz invariance

- extra space dimensions

---

[4]A density matrix describes a statistical ensemble of several quantum states. This is in contrast to a quantum mechanical mixture of a pure state, described by a state vector.

[5]Points with spacelike separation are not connected by a lightcone and are therefore not causally connected.

- discrete space and/or time

- noncommutative spacetime

As these items are objects of active research, it is natural to experimentally test the Spin-Statistics connection. A model for CPT and Lorentz invariance violation is for example presented in [18]. In the framework of superstring theory, which includes more than three spatial dimensions, a possible violation of Spin-Statistics was described in [19]. In quantum-gravity models decoherence effects can lead to intrinsic CPT violation and to a tiny violation of the PEP [20]. The level of a possible violation, if it is occurring, is presently unknown. Another important point when testing the PEP is that one does not search for fermions which are "a bit" different. If this kind of slightly different fermions would exist, the lowest order pair production cross section would double [14]. This is clearly ruled out by experiments. Because of the indistinguishability of identical particles, all fermions should have the same possibility for an admixture of a symmetric state. This is reflected in the use of the density matrix for the description of states in the case of quons.

2.3.2. Experiments for Testing the Pauli Exclusion Principle

According to S. R. Elliott, the various experiments testing the Pauli Exclusion Principle can be grouped into three classes [21], with respect to the kind of fermionic interaction they are investigating:

- Type 1: interactions between a system of fermions and a fermion that has not yet interacted with any other fermion

- Type 2: interactions between a system of fermions and a fermion that has not yet interacted with this given system

- Type 3: interactions between a system of fermions and a fermion within this system

These distinctions between different types of interactions are necessary due to the MG superselection rule (see also section 2.1.4). This rule forbids changes of the permutation symmetry of a quantum state in a system where the number of particles is constant. The important difference among these classes is that in a type 3 interaction, the superselection rule forbids a change in permutation symmetry as the investigated fermions already have a defined permutation symmetry with the

surrounding system and the number of particles in the system does not change. Therefore, the outcome of experiments of type 1 and type 2 can not be compared to the outcome of type 3 experiments. Subsequently the different types of experiments will be discussed and some examples will be given:

Type 1 experiments:

The typical experiment of this type uses newly created fermions and lets them interact with the system under investigation. In 1948 Goldhaber and Scharff-Goldhaber [1] used new electrons from a β source and let them be captured on Pb atoms. The idea of the authors was that if the particles from the β source are not subject to the PEP in the electron shell of the Pb atoms, they could cascade to the ground state and thereby emit photons which would be detected. The lack of these photons was later used to set an upper limit on the probability for the violation of the PEP. The fundamental point is that the electrons from the β source have not yet interacted with any system and are therefore new to the electronic system of the Pb atoms. As they are new to this system, they do form new quantum states with the Pb atoms. Forming states with a symmetric admixture is not forbidden by the MG superselection rule in this case. This is also true if the electronic state of the atom has previously been in a completely antisymmetric state. Other sources of recently produced fermions can also be pair-production processes and nuclear reactions.

Type 2 experiments:

In these experiments, fermions are brought from outside a system to interact with it. The typical experiment is the one conducted by Ramberg and Snow [2]. In this experiment, electrons were introduced to a copper conductor via a current. These current electrons had no previous interactions with the atoms in the conductor and are considered as "new" to them. Therefore, the same arguments apply as for the type 1 experiments and the formation of a state with an admixture of symmetric exchange symmetry between the atoms of the conductor and a conduction band electron is not forbidden by the MG superselection rule.

In the case of a symmetric admixture in a quantum state formed between an atom in the conductor and the current electrons, the current electron could cascade to the 1s ground state, resulting in three electrons in this state. During the cascading process, photons would be emitted. The lack of detected photons is used to set an

upper limit on the probability for the violation of the PEP. An interesting point is the precise origin of the electrons in the conduction band. In an optimal setup, they are coming from a battery. This would guarantee the newness of the electrons. The drawback is that a high current is hard to maintain in this way. If the power of the current source comes from an AC grid the electrons in the conduction band of the conductor will comprise electrons from the conductor itself and the circuitry connecting it to the power supply.

An interesting idea was put forward by E. Corinaldesi [22], who suggested that the PEP is not a kinematic principle but rather a time-dependent effect of interactions and that newly formed systems may undergo PEP violating transitions, whose rate decreases with time. This suggestion could be tested with a type 2 experiment. In [23] it was suggested that this hypothesis can be tested by crossing an electron and a Ne^+ ion beam, and by monitoring potential photons from PEP violating transitions.

Type 3 experiments:

A type 3 experiment searches for a PEP violating transition in a stable fermionic system where the number of particles is constant. Notably, the considered systems need to change their permutation symmetry in order to undergo these transitions. Therefore, type 3 experiments violate the MG superselection rule and their outcome can not be compared to type 1 and type 2 experiments.

Nevertheless, many experiments of this kind have been conducted. Pioneers in this kind of experiment were Reines and Sobel [24]. They were looking for transitions of L-shell electrons to the already occupied K-shell in iodine atoms. The DAMA/LI-BRA experiment conducted an analysis of their data regarding the same process [25]. Nuclear processes were also investigated regarding PEP-violating transitions, for example in [26] by the Borexino collaboration. The experimenters were looking for non-Paulian transitions of nucleons from the 1p to the 1s nuclear shell.

Anomalous Structure

Another type of experiment is to look for anomalous nuclear and atomic structures. In [27] an experiment is reported where atomic states with three electrons in the K-shell are searched. Non-Paulian atomic states of Be are explored in [28].

Some limits on the probability of a violation of the PEP are summed up in ta-

Process	Type	$\frac{\beta^2}{2}$ limit	Reference
anomalous atomic transition	1	3×10^{-2}	[1]
anomalous atomic transition	2	4.7×10^{-29}	[4]
anomalous atomic transitions	3	1.28×10^{-47}	[25]
anomalous nuclear transitions	3	2.2×10^{-57}	[26]
anomalous atomic structure	Anomalous Structure	2×10^{-21}	[27]

Table 2.1.: Limits on the PEP violation probability from different experiments.

ble 2.1.

The most stringent limit prior to the VIP2 experiment in a system circumventing the MG superselection rule (type 1 + 2 experiments) is set by the VIP experiment [4]. It has to be stressed again, that the experiments of type 3 can not be compared with other experiments, as they search for transitions which are not in accordance with the MG superselection rule. The experimental method of the VIP and VIP2 experiments will be described in the next section.

2.4. The VIP2 Experimental Method

As mentioned in section 2.3.2, the change of the permutation symmetry of a quantum state is not forbidden by the MG superselection rule, when a fermion, which is new to the studied system (e.g. atom, nucleus), interacts with it. These types of experiments were classified as type 1 and type 2. To the best of our knowledge, the most feasible way to introduce a large number of fermions into a system is by introducing a current into a conductor. The number of electrons introduced in this way is for 1 A $\sim 10^{19}$ per second. While moving through the conductor with a velocity influenced by the applied electric potential, these electrons have a certain probability to interact with the atoms in the conductor. Due to this interaction, the electrons from the conduction band can form a new quantum state with the electrons in the atoms. It is important to mention that the electrons in the conduction band did not have a defined symmetry with respect to the atomic electrons before this interaction happens, as they come from the current source outside of the conductor. The formation of a new quantum state is the reason why this kind of experiment does not violate the MG superselection rule. After the formation of a new state, the former current electron can have symmetric permutation symmetry with respect to particle exchange with the other electrons in the electron shell if the PEP can be violated. This electron sees all the states occupied

by the atomic electrons as empty and can occupy them. Therefore, it will cascade down into the 1s ground state of the atom, emitting photons as it loses energy.

Photons, possibly from PEP-violating transitions, are collected for some time close to the conductor with and without a current flowing through this conductor. As there are no new electrons introduced to the system during the measurement without current, there are also no photons from PEP-violating transitions expected in this time. This measurement is used to determine the background in the energy spectrum. From the difference between the energy spectra in the energy regions where photons from the PEP violating transitions are expected, the probability for a violation of the Pauli Exclusion Principle can be calculated, or upper bounds for this probability can be set.

For the VIP2 experiment the conducting material is copper (Cu). It has the atomic number 29 and is part of the group 11 in the periodic table of elements, together with for example silver (atomic number 47) and gold (atomic number 79). A common feature of these elements is that they are good conductors for electrical currents. Copper has a resistivity at room temperature of 1.68×10^{-8} Ω m, silver has 1.59×10^{-8} Ω m and gold has 2.44×10^{-8} Ω m, making silver the best conductor of them. Copper was the obvious choice for this experiment, as the SDD detectors are sensible to X-rays in the energy region of the Cu Kα transition, which is not true for silver and gold. The mentioned elements are good conductors due to the unpaired electron in the outermost s-shell. The electronic configuration for copper for example is [Ar] $3d^{10}4s^1$. The Fermi energy [6] overlaps the 4s orbital [29]. It is a broad band [7] which resembles the dispersion relation of free electrons. At finite temperature the electrons of the 4s orbital can move freely in this band (i.e. change their momentum) and be the carrier of the current.

The energies of the PEP violating cascading process were calculated for copper atoms in [30] using a self-consistent multiconfiguration Dirac-Fock (MCDF) approach. In this case self-consistent is best explained with the help of figure 2.2. It means after calculating the potential from a charge density at any step and solving the Schrödinger equation with it, the charge density calculated from the Schrödinger equation needs to be the same as the initial charge density. The term "multiconfiguration" comes from the fact that the total wave function is described as a linear combination of configuration state functions, which are related to a specific configuration of electrons. Using the Dirac-Fock approach as opposed to

---

[6]The Fermi energy is the energy of the highest occupied energy state of a system at a temperature of 0 K.

[7]An energy band in a solid is a region of allowed states in a E($\vec{k}$) diagram. Here E is the energy and $\vec{k}$ is the wave vector.
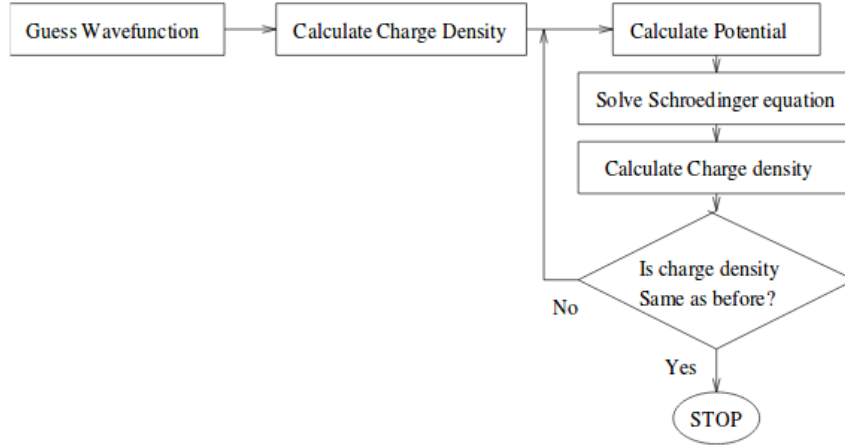
Figure 2.2.: A self-consistent algorithm for calculating the energy of atomic states.

the Hartree-Fock means that relativistic effects are accounted for. The relativistic Breit-Dirac Hamiltonian is used, which takes into account all electromagnetic interactions of spin $\frac{1}{2}$ particles, including spin-orbit coupling and retardation effects. Furthermore, the Lamb shift and radiative corrections (vacuum polarization and self-energy) are included. In the whole procedure the "no pair" approximation is applied which explicitly excludes electron positron pairs.

The original code for this calculation, which was later adapted for the use of the VIP2 experiment, was described in [31]. The code is available on the website [32]. It calculates the energies of atomic states in an electronic shell in which all but one electron have antisymmetric exchange symmetry. These states violate the PEP. The working principle of the calculation was described as a three step process in [33]:

- Step 1: The functional form of the wave function is selected and defined as a linear combination (using a number of parameters) of certain functions (mostly hydrogen-like wave functions).

- Step 2: An expression for the total energy is derived in terms of these functions and parameters.

- Step 3: The variational principle is applied and equations are derived for the valid solutions that are the functions that leave the total energy stationary. In this step self-consistency is checked.

The total wave function must then also obey the Hartree-Fock assumptions, mean-

ing that the wave function is antisymmetric, with the exception of the one electron which has a symmetric exchange symmetry. Furthermore, the total wave function needs to be an eigenfunction of the L^2, L_z, S^2 and S_z operators. The main uncertainty in the calculation is not the atomic calculation itself, but effects from the environment of solid state copper. The results of these calculations for copper are summed up in table 2.2.

Transition	Transition energy - PEP violating (eV)	Transition energy - normal (eV)	Radiative transition rate (s^{-1})	Energy Difference (eV)
$2p_{\frac{3}{2}} \to 1s_{\frac{1}{2}}$ $(K\alpha_1)$	7747	8048	2.64×10^{14}	301
$2p_{\frac{1}{2}} \to 1s_{\frac{1}{2}}$ $(K\alpha_2)$	7729	8028	2.57×10^{14}	299
$3p_{\frac{3}{2}} \to 1s_{\frac{1}{2}}$ $(K\beta_1)$	8532	8905	2.68×10^{13}	373

Table 2.2.: Transition rate and energies for PEP violating transitions in copper calculated with the MCDF algorithm [30]. In the last column, the calculated energy difference between normal and PEP-violating transitions is shown.

It is interesting to note, that the rate of forbidden transitions is highest for the $K\alpha_1$ transition, similar to the rate of normal transitions, even though the difference is not as high. This is why for future calculations the energy value of the PEP forbidden $K\alpha_1$ line of 7747 eV will be used. Furthermore, as the transition rate of the $K\beta$ is lower by one order of magnitude, the primary focus of the analysis will be on the $K\alpha$ transitions. Due to the angular momentum selection rules [8], the 2s - 1s transition is forbidden, which also holds true for PEP forbidden transitions.

The difference in the transition energies between the normal K-lines and the PEP forbidden K-lines listed in table 2.2 can be illustrated with figure 2.3. On the left side of the figure a normal 2p to 1s transition is shown. In this transition an electron from the 2p shell fills a vacancy in the 1s ground state, thereby losing 8048 eV of

---

[8]The conservation of angular momentum demands $|J_i - J_f| \leq \lambda \leq J_i + J_f$, where $J_{i,f}$ are the initial and final total angular momenta and λ is the photons angular momentum. $\lambda = 0,1,2,..$ for electric and magnetic monopole, dipole, quadrupole, ... transitions. The change of parity for electric transitions is $(-1)^\lambda$ and for magnetic transitions it is $(-1)^{\lambda+1}$, which ensures the conservation of overall parity. The parity of a state is $(-1)^L$, so it does not change from 2s to 1s. As for electric dipole transitions the parity needs to change, it is electric dipole forbidden.
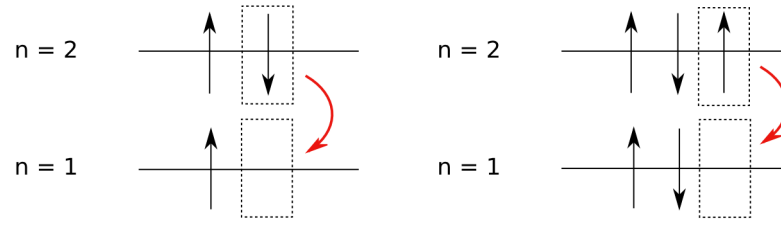
Figure 2.3.: Scheme of normal 2p to 1s transition (left) and a 2p to 1s transition which is violating the PEP (right).

energy in the form of a photon. On the right side the corresponding PEP violating transition is shown. The electron undergoing the transition cascades down from the 2p into the 1s shell, but in this case, the 1s shell is occupied with two electrons. This is only possible because of the symmetric admixture in the symmetry of the wave function. The two electrons in the 1s ground state shield the core potential more than the one electron in the case of the normal transition. Thereby they reduce the effective nuclear charge, which causes the transition energy to be lower for this transition. In the case of the Kα transition for copper, the difference in energy is around 300 eV.

3. The VIP2 Measurement Setup

As mentioned in chapter 2, the core functionality of the VIP2 experiment is to measure energy spectra in the energy region where the PEP violating Kα transition is expected. For this purpose Silicon Drift Detectors are used. They offer an energy resolution good enough to separate the possible PEP-violating Kα transitions from the normal transitions, which are 300 eV more energetic in copper. Furthermore, the SDDs offer a time resolution < 1 μs, which allows the use of an active shielding system, consisting of 32 plastic scintillator bars arranged around the copper target and the SDDs. The scintillation light output is read out by Silicon Photomultipliers. The working temperature of the SDDs is around 100 K. Their temperature is kept constant by a system composed of a helium compressor liquefying argon, which in turn cools the detectors. A data acquisition and a slow monitor system are in place to collect data and monitor crucial parameters of the experiment. The SDDs and the active shielding system are mounted inside a 55 cm $\times$ 40 cm $\times$ 32.8 cm vacuum chamber made out of 15 mm thick AlMg4,5Mn. A schematic drawing of the experiment is shown in figure 3.1. All the components of the setup will be described in detail in the following sections.
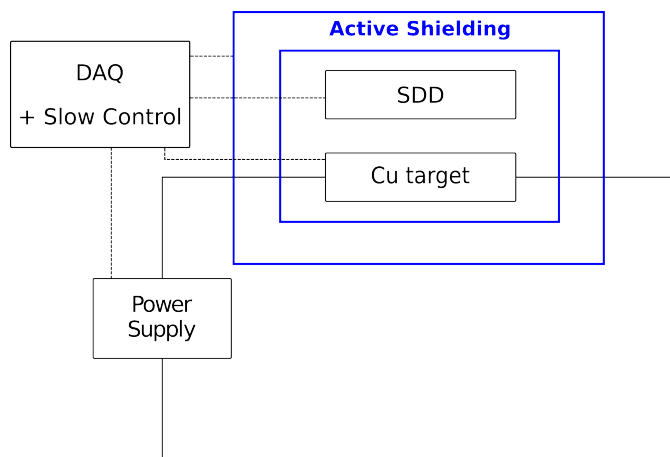

Figure 3.1.: Schematic drawing of the VIP2 experiment.

3.1. Silicon Drift Detectors and Copper Target

Silicon Drift Detectors are used in the VIP2 experiment as X-ray detectors. They are mounted as close as 5 mm away from the Cu target in the setup, to maximise solid angle coverage.

The Cu target consists of two strips with a length of 7.1 cm, a width of 2 cm and a thickness of 50 μm. The strips are connected to a current supply via Cu connectors. Between the two strips runs a water cooling line made out of stainless steel (supply tubes) and aluminum (cooling pad) to keep them at a constant temperature even with a high current flowing through them. The water cooling pad is attached to the Cu strips by non-conductive thermal glue. One SDD array with three individual cells is mounted on each side of the target strips. The SDDs detect possible photons from PEP violating transitions in the Cu target introduced by the high current flowing through this target.

3.1.1. Working Principle

The working principle of Silicon Drift Detectors is based on sideward depletion, which was first introduced in [34]. A schematic drawing of an SDD used for the VIP2 experiment is shown in figure 3.2. On a cylindrical n-type [1] silicon wafer
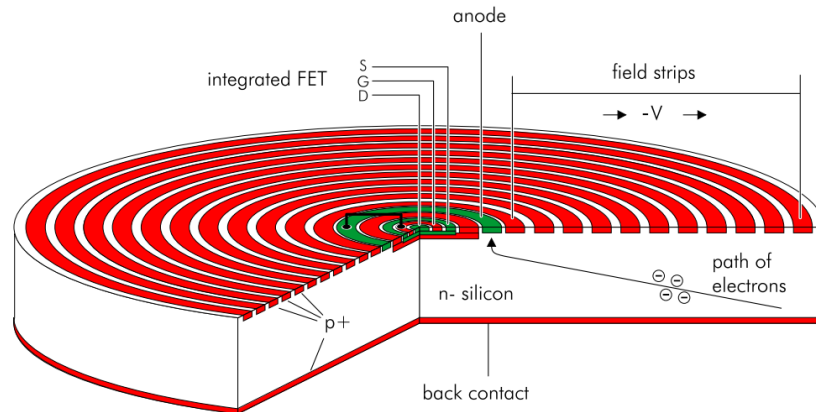

Figure 3.2.: Scheme of a Silicon Drift Detector [35].

circular p$^+$-type silicon contacts are implanted on one flat surface. These contacts are used to apply an increasing reverse bias in order to fully deplete the wafer. The radiation entrance window is on the opposite side of the concentric contacts and consists of a homogeneous shallow junction, which gives homogeneous sensitivity over the whole surface. When photons or charged particles hit the silicon wafer, electron-hole pairs are generated. The free electrons fall to the lowest point of the potential produced by the concentric electrodes. This lowest point is the anode consisting of a ring close to the middle of the wafer. The amount of electrons generated in the wafer and collected by the anode is proportional to the energy of the radiation. By measuring the amount of charge collected this energy can be determined. The small size of the anode ensures a small anode capacitance, which is almost independent of the size of the detector [36] and only proportional to the anode's size. As some sources of noise are proportional to the capacitance [37], this reduces the noise and allows shorter shaping times [2], which in turn allows high count rates. As a first stage of amplification, a field effect transistor (FET) [3] is integrated in the chip and connected to the anode by a metal strip. Thereby the capacitance between detector and amplifier is minimised and electric pickup noise is mostly avoided. The anode is discharged continuously. This avoids regular dead times of the detector by a repeating reset mechanism.

3.1.2. SDD Specifications for the VIP2 Experiment

The manufacturer of the employed detectors (PNSensors) produced a manual, from which the information in this section is reported [35]. The SDDs employed in the VIP2 experiment consist of two arrays with three detector cells each. Each cell has an active area of 1 cm^2 shaped like a "rounded square" with a diameter of 10.3 mm and a corner radius of 2 mm. The maximum drift path length for electrons originating in a corner is 6.4 mm. The cells have a thickness of 450 μm, which ensures an absorption of $\sim$ 99 % of 8 keV (Cu Kα line) X-rays. The three cells in an array share a common outermost strip (Rx), a common bulk contact (outer substrate - Os) and common guard ring systems on both sides of the chips. Each cell has a readout structure in its center and individual back contact (Bc) and separation mesh (back frame, Bf) contacts. The bonding and the way the voltages

---

[1]n-type semiconductors are doped with elements that are pentavalent, like phosphorus. This results in an excess of electrons. p-type semiconductors are doped with trivalent elements like boron, which results in an excess of holes.

[2]Long shaping times can be used in order to cancel out noise.

[3]A field effect transistor controls the conductivity between the source (S) and the drain (D) via an electric field between the body and the gate (G) of the device.

were adjustable were modified slightly for the VIP2 experiment, with respect to the scheme reported in [35]. The important contacts and the way the respective voltages are adjustable (all SDDs common, all SDDs in an array, each individual SDD cell) are shown in table 3.1. Plots of the front and the back side of the arrays are shown in 3.3 and 3.4. There is a total number of 74 concentric electrodes,
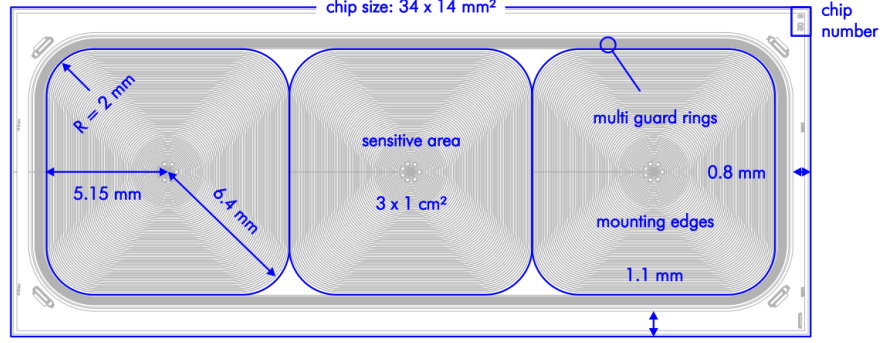
Figure 3.3.: Front side of the SDD array of the VIP2 experiment [35].
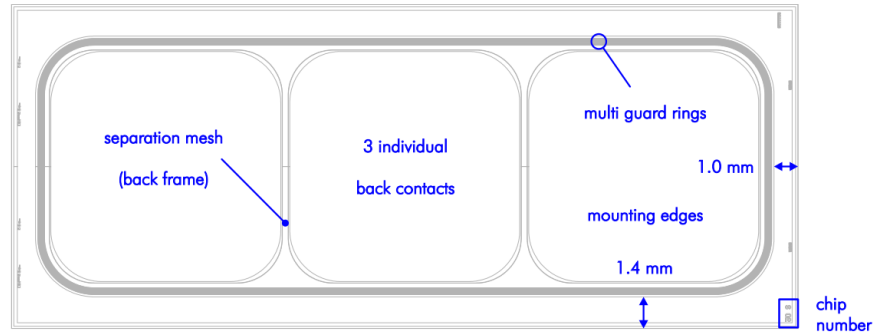
Figure 3.4.: Back side of the SDD array of the VIP2 experiment [35].

where the innermost 23 are circular and the ones closer to the outside are linear in vertical and horizontal direction with rounded edges. The first and the last ring are biased externally, the others are connected via a resistive voltage divider.

The detectors are mounted on a ceramic material made out of aluminum oxide for bonding. This material has low electrical and a high thermal conductivity. The mounting frame is made out of aluminum. As the transition energy of a Kα transition in aluminum is around 1.5 keV, X-rays in the energy region around 8 keV which is interesting for VIP2 can be avoided by this choice of the material. The SDDs together with their support structure, readout and cooling are shown in figure 3.7.

Contact Name	Abbreviation	Bonding	Nominal Value [35]
Outermost strip	Rx	Common	-240 V
Innermost strip	R1	Common	-15 V
Outer substrate	Os	Common	GND
Inner substrate	Is	Common	GND
Entrance Window	Bc	Cell	-120 V
Separation Mesh	Bf	Array	-140 V

Table 3.1.: Some important contacts of the Silicon Drift Detectors used for the VIP2 experiment.

3.1.3. Silicon Drift Detectors Performance Characteristics

The energy and time resolution, as well as scale linearity, are crucial factors in the performance of the SDDs. The possibility of a high event rate would be another point to consider, but as this is not an issue for the VIP2 experiment with count rates of ∼2 Hz, this point will not be discussed.

The detector linearity is the ratio between produced electron-hole pairs and deposited energy, as a function of energy. If the whole energy of the incident radiation is deposited in the detector and no losses occur during the charge transport, the number of electrons arriving at the anode only depends on the energy. Consequently, the detector response should be perfectly linear, assuming a linear response of the readout system.

An advantage of semiconductor detectors with respect to gaseous detectors is the lower energy needed to create an electron-hole pair. At 77 K, this energy is 3.81 eV [37] for silicon, which is independent of the type and energy of the incident radiation. The amount of charge carriers produced by the same radiation will therefore be one order of magnitude higher than in gaseous detectors. Therefore, semiconductors provide a greatly enhanced energy resolution. On the other side, the energy resolution is limited by noise. One part is the so-called Fano noise. It results from a non-constant amount of electron-hole pairs produced for different events with the same energy. The Fano factor F is defined as:

$$F = \frac{\sigma^2}{\mu} \tag{3.1}$$

Here σ^2 is the variance of the number of produced electron-hole pairs and μ is the average of the number of electron-hole pairs. It is not dependent on energy and for

silicon the value is estimated to be $F = 0.12$ [37]. Another source of noise is the leakage current, which is a small fluctuating current flowing through semiconductor junctions in case of an applied voltage. The fluctuation in the current appears as noise in the detector. One source of leakage current are thermally created electron-hole pairs originating from recombination and trapping centers in the depletion region. These centers result from impurities in the crystal. This part of the noise can be suppressed by lowering the temperature. Another source of leakage current are surface currents.

In order to have the possibility of an in-situ energy calibration, a 10 μCi (3.7 $\times$ 10^5 Bq - measured in 2005) Fe-55 source [4] is installed in the VIP2 setup. The photons from the source hit the SDDs directly and also induce Kα transitions in a titanium foil, which is located between the source and the detector. These two photon sources enable continuous calibration of the energy scale and thereby minimize peak drift effects and optimize the energy resolution.

The time resolution of the SDDs is determined by the drift time of the electrons from their origin to the anode. In [35] the maximum drift time at 150 K for the type of detector used in the VIP2 experiment is estimated to be 600 ns. Due to the temperature dependence of the electron mobility (e.g. increased phonon scattering), the time resolution generally deteriorates with rising temperature. The measured performance characteristics of the SDDs used in the VIP2 experiment will be discussed in chapter 5.

3.2. Active Shielding

The active shielding system has the purpose of rejecting SDD events caused by external radiation (e.g. from cosmic radiation). This means that whenever a signal in the SDDs is in coincidence with a signal from the scintillators, it can be rejected. The active shielding consists of 32 scintillators read out by two Silicon Photomultipliers (SiPMs) each, which are assembled around the copper target and the SDDs. A render of the setup including the active shielding system enclosing the target is shown in figure 3.5.

---

[4]An Fe nucleus with 26 protons and 29 neutrons decays via electron capture to Mn-55 with a half-life of 2.737 years. This results in the emission of a photon or an Auger electron.
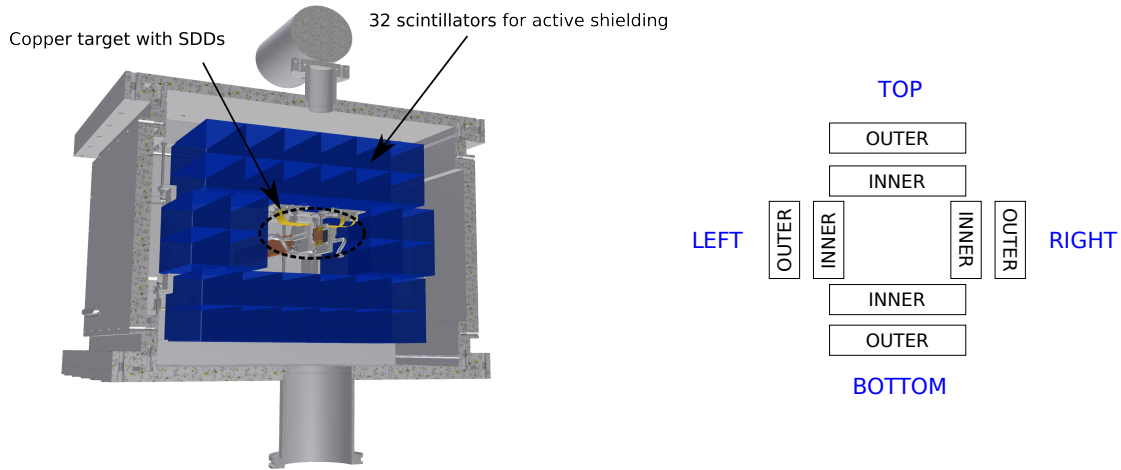
Figure 3.5.: Render of the active shielding system of the VIP2 experiment consisting of 32 scintillators (left). The scintillators can be grouped into an "outer" and an "inner" layer of 16 scintillators each (right).

3.2.1. Scintillators

Scintillators are materials that emit photons after they are hit by ionizing radiation. The scintillators used in the VIP2 experiment are plastic scintillator bars of the type EJ-200 produced by Eljen Technologies. Their dimensions are 38 mm × 40 mm × 250 mm. The base polymer is polyvinyl toluene and the flour is anthracene [38]. When ionizing radiation passes through the scintillator, electrons in the valence band in so-called molecular orbits are excited [37]. Subsequently the excited states loose their energy via the emission of a photon, typically in the UV range. A flour is suspended in the polymer matrix to absorb the UV radiation and re-emit it at visible wavelengths. The wavelength of maximum emission for the scintillators used in VIP2 is 425 nm (blue light) and their pulse width is 2.5 ns (FWHM) [38]. The scintillation material has a refractive index of 1.58, meaning that total internal reflection can occur for photons with a flat impact on the surface. Nevertheless light can also escape the scintillator if the impact angle is too steep. To increase the light collection on the SiPMs, the scintillators were wrapped in reflective aluminum foil to reflect stray photons back into the scintillator, while leaving a small air gap in between the foil and the scintillator. To minimize the influence of photons from the environment (i.e. ambient light) hitting the SiPMs, a layer of black tape was wrapped around the aluminum foil.

3.2.2. Silicon Photomultipliers

A Silicon Photomulitplier consists of an array of semiconductor pn junctions working in reverse bias mode. For the VIP2 experiment, we use the 3×3 mm^2 ASD-SiPM3S-P50 SiPMs manufactured by AdvanSiD. On one end of each scintillator bar, two SiPMs are attached with optical glue and connected in series. As the probability of correlated dark counts in both SiPMs is suppressed compared to reading a single detector, the signal to noise ratio can be improved in this way. One SiPM consists of 3600 sequentially connected Silicon avalanche photodiodes (APD) with an area of 50×50 μm each. All of them are operated in Geiger mode (an analogy to the Geiger counter), meaning that the reverse bias voltage is higher than the breakdown voltage [5]. In this mode, the generation of one charge carrier causes an avalanche of charge carriers due to impact ionization. The first charge carrier can be produced by an incident photon undergoing the photoelectric effect. In the case of the VIP2 experiment, this photon comes from the scintillator. The energy of the optical photons from the scintillator (425 nm $\sim$ 2.9 eV) is enough to generate an electron-hole pair. The spectral response range for the SiPMs used for VIP2 is 350 nm - 900 nm [39], overlapping with the photon spectrum of the scintillator.

The time resolution of a system of a scintillator read out by SiPMs is typically on the order of a few ns. This means that it is small compared to the time resolution of the SDDs, which is in the order of a few 100 ns.

3.3. Cooling System

The Silicon Drift Detectors used for the VIP2 experiment have a working temperature of around 150 K [35] or lower. To reach this temperature, a system of a helium compressor coupled to a pulse-tube refrigerator is used with helium gas as working medium. The cooling power produced by this system liquefies argon, which evaporates and cools the detectors down.

A CNA-21A helium compressor from SHI (Sumitomo Heavy Industries) cryogenics is used. This compressor receives $\sim$ 9.8 bar helium gas at room temperature from the cold head. This gas is then compressed to $\sim$ 22 bar and cooled back down to room temperature after it was heated due to the compression. The compressor

---

[5] The breakdown voltage of a diode is the minimum reverse bias voltage to make the diode conductive.

is air-cooled meaning the helium gas flows through a heat exchanger after compression which is cooled with ambient air. The high pressure helium gas at room temperature is then supplied to a pulse tube refrigerator. The working principle of this type of refrigerator is shown in figure 3.6. The high pressure helium gas is con-
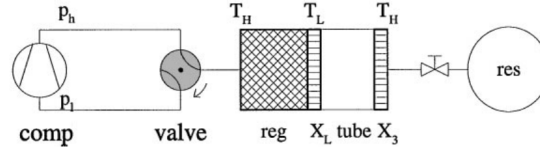

Figure 3.6.: Schematic drawing of a pulse tube refrigerator [40].

nected to the RP-2620A coldhead which is also manufactured by SHI - cryogenics. The cold head has a valve on its side close to the helium compressor. This valve connects the refrigerator to the high and the low pressure side of the compressor in an alternating way. Coming from the high pressure side of the compressor, the gas first hits a regenerator at a high temperature ($\sim$ room temperature) T_H. After the regenerator, there is a heat contact X_L to the medium to be cooled at the lower temperature T_L. Subsequently the pulse tube follows where the gas is thermally isolated (adiabatic) and therefore the temperature of the gas depends on its pressure. After the pulse tube a thermal contact to the surroundings is installed. The pulse tube is coupled to a gas reservoir via a flow resistive valve. The heat exchangers, the regenerator and the pulse tube are suspended in vacuum of $\sim 10^{-5}$ - 10^{-6} mbar.

When the high pressure helium gas flows through the regenerator, it is cooled down to T_L, thereby transferring heat to the regenerator. The gas enters the pulse tube at T_L. Then the pressure is switched to the low pressure side of the helium compressor, which is around 10 bar in our case, and the gas flows out of the tube. But due to the lower pressure, the temperature in the tube is now lower than T_L. The gas now flows through the thermal contact X_L. It cools the contact and thereby effectively cools the argon gas, with which X_L is in thermal contact. The helium gas then flows through the regenerator at T_L, whereby it transfers the heat that was stored in the regenerator back to the gas. The opposite effect occurs at the temperature T_H at X_3, where heat is dissipated to the environment. The coefficient of performance (ratio between cooling power and compressor power) for an ideal pulse tube refrigerator is $\frac{T_L}{T_H}$, which is lower than the one of a Carnot process $\frac{T_L}{T_H - T_L}$ due to losses in the valve [40].

The cooling power of the pulse tube refrigerator at X_L is used to cool down an aluminum target through which the argon gas flows. The argon condensates and

flows down a pipe which runs past the SDDs, cooling them to their working temperature. Thereby the argon evaporates. Afterwards it is cooled again by the pulse tube refrigerator. A picture of the SDDs with the argon cooling line and a readout board is shown in figure 3.7.
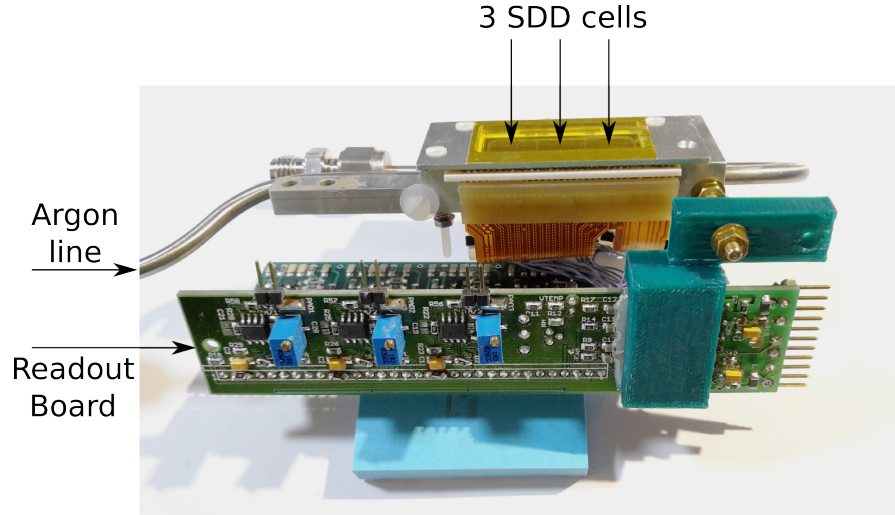

Figure 3.7.: The SDDs with the argon cooling line and the readout board.

The cooling of the pulse tube refrigerator is counteracted by a heating wire controlled by a LakeShore 331 temperature controller. This is done in order to be able to control the temperature of the argon by adapting the heating power. Changes in argon temperature can in this way be compensated with the PID (Proportional Integral Differential) control of the LakeShore 331 on a very short timescale. The vacuum needed to maintain the necessary cryogenic temperatures is maintained by two turbo pumps connected to a common prepump.

3.4. Data Acquisition and Slow Control Systems

3.4.1. Signal Readout and Data Acquisition

After a first stage of amplification in the preamplifier board in the vacuum chamber, the signals of the six SDDs go into a programmable CAEN 568B spectroscopy amplifier. The fast "FOUT" signal of the amplifier goes to a discriminator to make a trigger. An OR of all six discriminated SDD signals is going to a CAEN V1190B

TDC (Time to Digital Converter), which stores the arrival time of this signal. The "OUT" output of the amplifier, which has adjustable gain, is used for spectroscopic signal analysis. The spectroscopic signal is fed into a CAEN V785 peak sensing ADC (Analog to Digital Converter) for digitalizing the signal. This ADC stores a value proportional to the peak height of the incoming signal.

The signal from the two SiPMs from each of the 32 scintillators is amplified in a preamplifier board in the vacuum chamber. The analog signal is split thereafter, with one part going to a programmable Constant Fraction Discriminator (CFD) to make a timing signal in the TDC and to make the the trigger, and the other going to a CAEN V792 QDC (Charge to Digital Converter). The QDC integrates the signal in each channel and stores a value proportional to this integrated charge. Referring to figure 3.5, the 32 scintillators can be grouped into one "outer" and one "inner" layer, and more specifically into eight sub-layers with the indication of their position relative to the target (e.g. "top outer" layer indicates the eight scintillators above the target, which are closer to the setup box). A signal of one of these layers is an OR of all the discriminated SiPM signals in this layer. The discriminated signal of each of these eight sub-layers and an AND of the outer and inner layer is sent to the TDC.

The digital signal from the discriminators is used to make a trigger for the TDC, ADC and QDC modules. The trigger logic is shown in figure 3.8. It consists of the OR of all six SDDs making an OR with the inner AND outer scintillator layer. The AND of the inner and outer scintillator layer is designed to trigger mainly
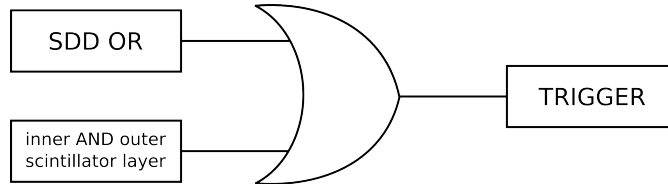

Figure 3.8.: Trigger definition of the VIP2 experiment.

on cosmic radiation, but also on any other radiation which produces a detectable signal in both of these layers. The OR of the SDD signals includes every SDD event above an energy threshold of approximately 1-2 keV, depending on the SDD. From the arrival times of the signals from the SDDs and the scintillators in the TDC, the time correlation of both of these systems can be examined.

The data from ADC, QDC and TDC are read out via a CAEN V2718 VME - PCI bridge to a CAEN A2818 PCI controller. A LabView program is communicating with this controller to record and store the data in binary form.

The stored data therefore includes information about the signal amplitudes of all six SDDs (from the ADC) and all 32 scintillators (from the QDC) as well as the arrival times of the signals of all eight scintillator layers, the AND of inner and outer scintillator layer and the OR of all six SDDs (from the TDC). Further information that is stored is the current trigger rate and the time and date of the event. The complete DAQ layout is shown in the appendix in figure B.1.

3.4.2. Slow Control

The slow control is the system which monitors and controls important parameters of the experiment. A schematic drawing of its layout is shown in figure 3.9. The
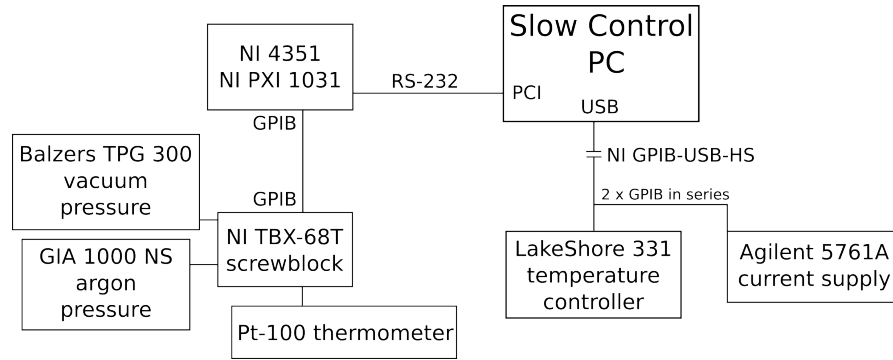

Figure 3.9.: A schematic layout of the slow control system of the VIP2 experiment.

central point of the system is a PC running a Visual C++ program which communicates with the different sensors and devices via a GPIB and a USB interface, storing and manipulating values of different parameters. The PC can be accessed remotely to control parameters and transfer the stored data. The USB interface is on the one hand connected to a LakeShore 331 temperature controller which regulates the heating of a resistor which counteracts the cooling of the cold head and thereby regulates the argon temperature. On the other hand it is connected to an Agilent 5761A current supply which provides the current through the copper target. The GPIB interface is connected to a National Instruments (NI) PXI 1031 chassis with a NI PXI 4351 board. This is then connected via GPIB to a NI TBX-68T screwblock which receives analog signals from several sources, which correspond to pressure and temperature at different points in the setup. Temperature information comes from Pt-100 resistance thermometers and pressure readings come from a cold cathode [6] for vacuum pressure (on the order of 10^{-5} mbar) and

---

[6]A cold cathode generates electrons via the discharge of a high voltage. The electrons ionize the gas and the number of produced ions is proportional to the gas pressure.

piezoresistive sensors [7] for the pressure of the argon gas (on the order of 1 bar). A list of all parameters that can be measured and controlled with the slow control system can be found in table 3.2.

All the values listed in this table are stored periodically. An emergency system is in place which periodically checks the values recorded by the slow control. In case specific values (like the vacuum pressure and the SDD temperature) exceed set thresholds, crucial systems like the turbomolecular pumps and the SDDs are turned off automatically. This is done by the communication with an Energenie EG-PM2-LAN plug which allows the automatic power shutdown of these devices which are attached to it.

3.5. X-ray Tube

During the measurements at the LNGS underground laboratory, an XTF-5011 X-ray tube is mounted on the setup for the possibility of a quick calibration of the SDDs. In our X-ray tube, electrons emitted from the cathode are accelerated by a high voltage of about 22 kV and subsequently impact on a tungsten anode. There they produce bremsstrahlung and possibly characteristic radiation of the tungsten anode. The photons, with a maximum energy of 22 keV, are shining onto the SDDs through a slit in the scintillators. On their way to the detectors, the photons are passing a titanium and a zirconium calibration foil, where they can excite a photon emission from these two elements. The emitted K-lines can then be used for a calibration of the energy scale.

Due to technical difficulties, the tube was only rarely turned on and can not be used for a regular calibration. Instead, the calibration is conducted with the Fe-55 source, which is permanently mounted inside the setup, as described in section 3.1.

---

[7]The piezoresistive effect causes the resistance of a material to change under mechanical strain.

Value to measure / control	Measured / Controlled by	Primary readout device	Adjustable
Room temperature	Pt-100	NI PXI 4351	No
Copper bar external temperature	Pt-100	NI PXI 4351	No
Copper bar internal temperature	Pt-100	NI PXI 4351	No
Water cooling pad temperature	Pt-100	NI PXI 4351	No
PCB board 1 temperature	Pt-100	NI PXI 4351	No
PCB board 2 temperature	Pt-100	NI PXI 4351	No
SDD 1 temperature	Pt-100	NI PXI 4351	No
SDD 2 temperature	Pt-100	NI PXI 4351	No
Argon upper line temperature	Pt-100	NI PXI 4351	No
Argon lower line temperature	Pt-100	NI PXI 4351	No
Argon target temperature	Pt-100	NI PXI 4351	No
Argon gas temperature	Pt-100	NI PXI 4351	No
Vacuum pressure	Balzers IKR 050 cold cathode	Balzers TPR-010	No
Argon gas pressure	Keller PAA-21-10	GIA 1000 NS	No
Heater output power	LakeShore 331	LakeShore 331	No
Heater PID settings	LakeShore 331	LakeShore 331	Yes
Argon gas set temperature	LakeShore 331	LakeShore 331	Yes
Current through copper	Agilent 5761A	Agilent 5761A	Yes

Table 3.2.: Summary of parameters measured and controlled by the slow control system.

38

4. Monte Carlo Simulations

For the purpose of evaluating and verifying several experimental parameters, the complete setup has been modeled in the Geant4 framework [41]. The utilized version of the framework is Geant4.10.2 . All components of the setup were considered in the simulations including the SDDs with metal frames, the copper target and the copper current supply bars, the scintillators and the calibration foils as well as the aluminum vacuum box. The PENELOPE (PENetration and Energy LOss of Positrons and Electrons) model was chosen for electromagnetic processes. As atomic de-excitation processes were important, fluorescence, auger electron emission and PIXE (Particle induced X-ray emission) were turned on. The simulations were conducted by Dr. Hexi Shi, a member of the VIP2 collaboration. A render of the setup is shown in figure 4.1.
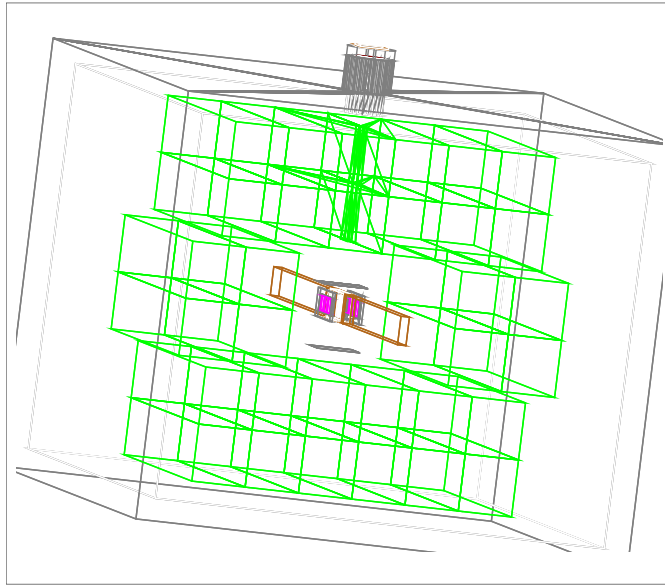

Figure 4.1.: View of the the VIP2 setup modeled in a Geant4 MC simulation.

4.1. Detection Efficiency of PEP-violating Transitions

One objective of the simulations was to determine the detection efficiency of the setup. The efficiency is in our case defined as the probability for an X-ray coming from a PEP violating transition (i.e. a photon with an energy of 7.7 keV) originating in one of the two target strips to be detected in an SDD. Two factors contribute to the efficiency. On the one hand the solid angle coverage of the copper target by the SDDs is limiting the efficiency. Taking into account the fact that the aluminum pad for water cooling between the two copper foils absorbs ~100 % of these photons, the solid angle can be estimated to be ~ 10 % (from the ratio between the area of the target and the area of the SDDs). On the other hand some photons can be absorbed inside the 50 μm Cu target. Here photoabsorption contributes most to this loss. This contribution can be estimated with the attenuation of photons going through half of the target (25 μm) which is approximately 25 %. This gives an estimation for the whole efficiency of approximately 2.5 %.

To determine the efficiency with a simulation, 10^6 photons with 7.7 keV were simulated with their starting positions randomly selected inside the copper target and their starting directions randomized over 4π solid angle. The result of the simulation is shown in figure 4.2. In the figure all original vertices in one copper
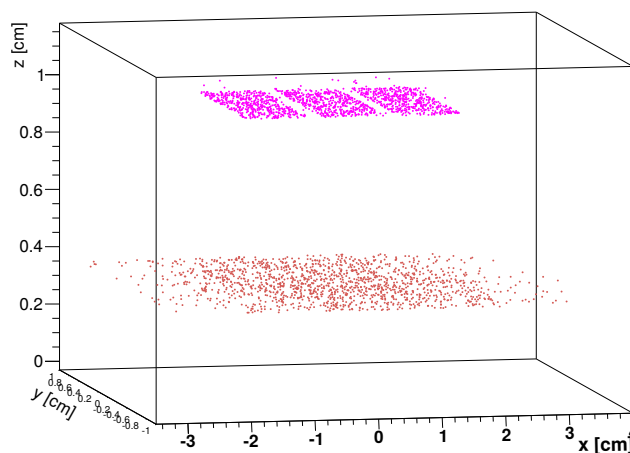

Figure 4.2.: Starting (brown) and end (purple) points of photons originating from the Cu target and hitting the SDDs generated by MC simulations.

target strip (starting points - brown) of photons which deposit all their energy in the SDDs are shown. The last vertices (end point of the track - purple) where the

photons lose their energy in the SDDs are also shown. Only photons which deposit all their energy of 7.7 keV in the SDDs are counted. It is evident from the figure, that most photons which are detected by the SDDs originate in the part of the 7.1 cm long target closer ("beneath" in the figure) to the SDDs. This can be explained by the larger solid angle under which these photons see the detector. Only one side of the simulation result is shown in the figure, as the setup is symmetric and the other side gives the same result.

From the 10^6 photons starting from the target, 18,200 were detected by the SDDs. This results in an efficiency of 1.82 %, which is close to the estimation of 2.5 % and therefore a realistic result.

4.2. Background from Cosmic Radiation

Cosmic radiation seen at the surface of the earth primarily consists of muons [42]. The origin of this radiation is so-called primary cosmic radiation consisting of nuclei which are part of the stellar power generation such as hydrogen and helium nuclei. These particles hit earth's atmosphere mainly generating mesons, which then decay into the cosmic radiation seen at the surface of the earth (e.g. muons). The rate of muons on the surface of the earth integrated over the whole solid angle is ~ 1 cm^{-2} min^{-1} [42]. For the simulation, 10^7 muons were generated in an area of 50 cm × 35 cm, which was located 20 cm above to the target. The primary particle energy was 270 GeV and the particle directions were randomized in the lower half-sphere. This energy was chosen as it was reported as the mean energy of the muon spectrum at LNGS in [43], and can also be used to estimate the contribution of muons to the detected events above ground. With the mentioned rate this corresponds to the background of ~ 4 days. This part of the background is important in measurements above ground, but is reduced at the underground laboratory LNGS by approximately six orders of magnitude. The goal of these simulations was to estimate the probability of the rejection of muons by scintillator veto and to estimate the signal rate from this source in the scintillators and SDDs.

The energy deposit in each scintillator summed up over all scintillators is shown in figure 4.3. A pronounced peak at ~ 8 MeV deposited energy is visible. With a scintillator thickness of 4 cm, this corresponds to an energy loss of 2 $\frac{MeV}{cm}$. Furthermore, the trigger rate of the scintillators can be estimated from the rate of 1 cm^{-2} min^{-1} to be ~ 1.67 Hz per scintillator or 10 Hz for all scintillators combined.
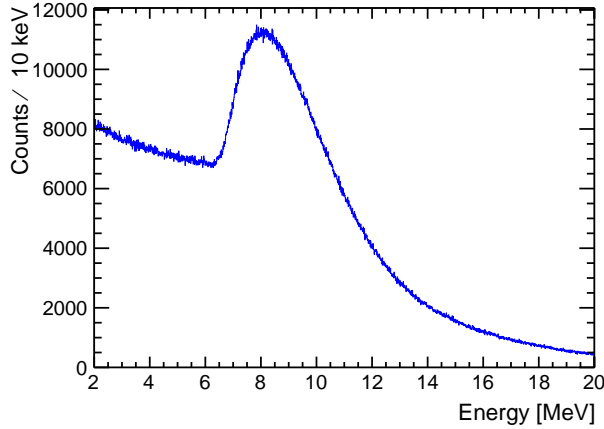
Figure 4.3.: Energy deposit of 270 GeV muons in plastic scintillators in MC simulations.

The energy deposit in the SDDs is shown in figure 4.4. The peak of deposited energy is in this case at around 300 keV. In all six SDDs combined there were 7896 hits in 7744 different events. This equals a rate of 0.0224 Hz or 1 event approximately every 45 seconds. The energy range of the SDDs is divided into a subrange of 1 keV - 30 keV and the energy > 30 keV, as everything above this value is in the overflow bin of the ADC. Therefore, it makes sense to calculate the rates for these two energy ranges. Approximately 4 % of the hits are in the lower subrange, 96 % are in the SDD overflow.

From the 7896 SDD hits, 7859 events have an energy deposit of more than 100 keV in the inner and the outer scintillator layer. A signal in both layers is the condition for a rejection. The threshold of 100 keV will be justified in chapter 5, whereas a threshold of 200 keV is suggested in section 6.5. This means, the background from cosmic rays can be rejected to ∼ 99.5 % for a 100 keV threshold. This value does not change for a threshold of 200 keV. An energy spectrum of the SDDs with and without scintillator veto is shown in figure 4.4.

The underground laboratory LNGS lies at 3800 m water equivalent depth, where the cosmic muon flux is reduced to 3.41×10^{-4} m^{-2} s^{-1} [44]. Compared to 1.67×10^2 m^{-2} s^{-1} given in [42] for the surface of the earth, which corresponds to a reduction to 2×10^{-6} times this value. The expected event rates due to cosmic muons calculated in the previous section scale accordingly. The hit rate for each scintillator is then $\sim 3.4 \times 10^{-6}$ Hz or ~ 1 event every 3 days and ~ 2 events per day for all scintillators. The expected event rate for all six SDDs is ~ 1 event
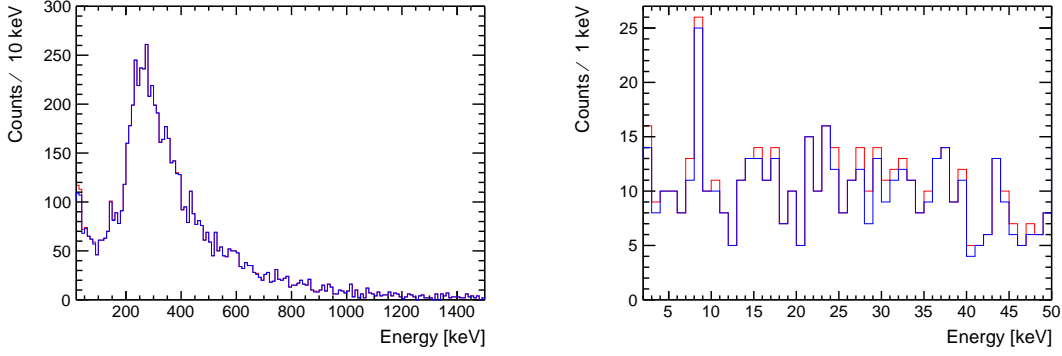
Figure 4.4.: The complete simulated spectrum (red) introduced in the SDDs in 4 days above ground by cosmic muons for two different energy ranges. The part that can be rejected by scintillator veto is also shown (blue). The two spectra are for the most part identical, meaning strong rejection power.

every 260 days, i. e. negligible.

4.3. Background from γ Radiation

The background consisting of γ rays is the dominant background in the underground laboratory LNGS, as cosmic radiation is reduced by almost six orders of magnitude. The origin of the γ radiation at LNGS are long-lived γ emitting primordial isotopes. They are part of the rocks of the Gran Sasso mountains and the concrete used to stabilize the cavity. The dominant isotopes of this kind are ^{238}U, ^{232}Th and ^{40}K [45] and their decay products. For the simulation 2.5×10^9 γ photons were generated on a surface of 0.945 m^2, which completely enclosed the setup. The energy distribution of the particles followed the one reported in [46] in the dominant energy range from 40 - 500 keV, which was modeled by a Landau distribution with a mode at 120 keV. The directions of the particles were randomized in the half sphere towards the setup. In [45] an integral flux of 0.33 γ cm^{-2} s^{-1} = 2.85×10^8 γ m^{-2} day^{-1} was reported, whereas in [46] a flux of 6.3×10^8 γ m^{-2} day^{-1} was given. For now the data from [46] will be used and later the result of this assumption will be compared with the measured data. In this case the simulated 2.5×10^9 particles correspond to a data taking time of 4.2 days.

The interaction of the photons with the scintillators takes place almost exclusively

via inelastic Compton scattering, meaning the photons do not deposit their complete energy. The deposited energy can be as high as 500 keV. A plot of the energy detected by the scintillators from high energy photon radiation is shown in figure 4.5. In the 4.2 days of the simulated data, there were 184,380 events with an
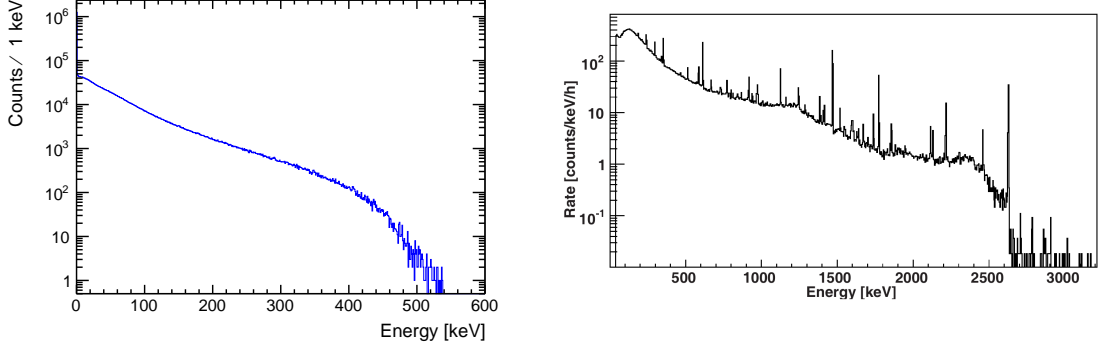

Figure 4.5.: Energy spectrum of γ radiation deposited in the scintillators in MC simulations corresponding to 4.2 days of data at LNGS (left). Measured photon spectrum at LNGS, from which the dominant part from 40-500 keV served as input for these simulations (right) [46].

energy deposit in the inner and outer scintillator layer larger than 100 keV. As this is the trigger condition, the trigger rate from these events is 0.51 Hz or ~ 1 event every 2 seconds in all scintillators. The scintillator hit rate for any detector receiving 100 keV or more would be around 8 Hz.

The energy spectrum in the range from 1 keV - 30 keV deposited in the SDDs is shown in figure 4.6. In the figure the Cu Kα and Kβ lines are visible at 8 - 9 keV as well as the Zr Kα and Kβ lines at 16 - 18 keV. The Cu lines are caused by photons from the Cu target and the Zr lines come from photons from the Zr calibration foil. This foil is mounted in the setup for the possibility to conduct an energy calibration of the detectors with an X-ray tube. In the 4.2 days of simulated data, there were 57,617 events in all SDDs with an energy deposit > 1 keV, corresponding to a rate of 0.16 Hz or ~ 1 event every 6 seconds in all SDDs. From these events, around 50 % are in the range between 1 keV - 30 keV. Comparing these rates to the ones induced by cosmic muons at LNGS, it is obvious that γ radiation is the dominant source of background.

From the 57,617 events in all SDDs with an energy deposit > 1 keV, 604 events have an energy deposit in the inner and outer scintillator layer and can therefore be rejected. The rejection ratio is therefore ~ 1 %. For an energy deposition threshold of 200 keV at the scintillators, the rejection rate is around 0.02 %. A plot of the
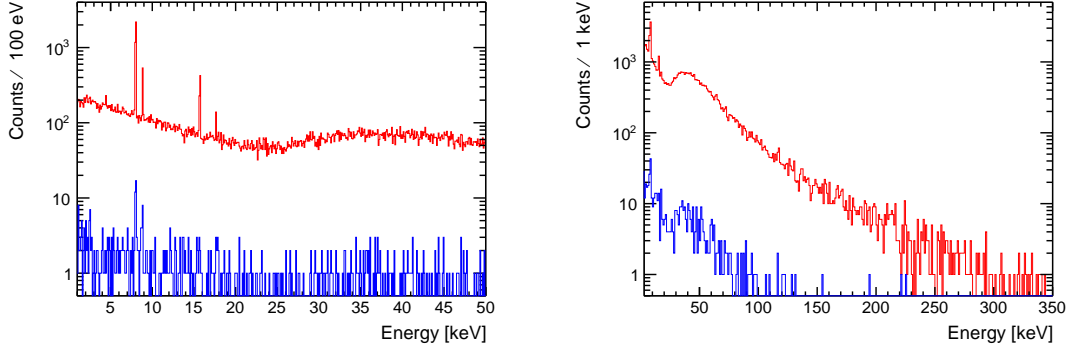
Figure 4.6.: The complete simulated spectrum (red) introduced in the SDDs in 4.2
days at LNGS by γ radiation for two different energy ranges. The part
that can be rejected by scintillator veto is also shown (blue). The Cu
and Zr lines are visible at 8 keV and 16 keV respectively.

full energy spectrum seen by the SDDs with the part that can be rejected with a
100 keV threshold is shown in figure 4.6.

This rejection rate might not be as high as expected, nevertheless the scintillators
also represent a passive shielding for low energy γ radiation and X-rays with at
least 8 cm of plastic scintillators in between the source of the radiation, which is
outside of the setup, and the SDDs. Furthermore, a passive shielding consisting
of lead and copper bricks will be installed around the measurement setup in the
future. This will reduce the background from γ radiation possibly to a level, where
it becomes comparable to the background from cosmic radiation. In this case the
active shielding would reduce the background by a larger fraction and improve the
result of the experiment.

5. Test Measurements

5.1. Test Measurements at LNF

First measurements with the scintillators read out by SiPMs were done at the Beam Test Facility (BTF) at Laboratori Nazionali di Frascati (LNF). This facility is connected to the linear accelerator of the DAΦNE collider and provides a 500 MeV electron or positron beam. The test setup is shown in figure 5.1, The scintillators
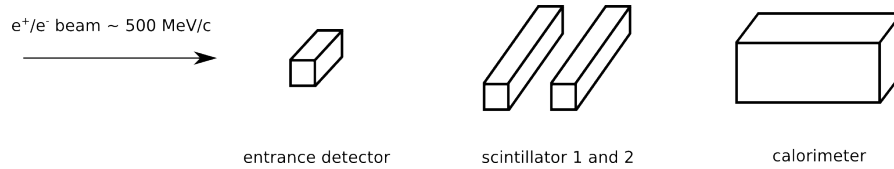

Figure 5.1.: The setup for testing the plastic scintillators with SiPM readout at the Beam Test Facility.

were the ones later on used in the VIP2 experiment, namely plastic scintillator bars of 25 cm × 4 cm × 3.8 cm. The trigger is defined as signal in the calorimeter AND a signal in the entrance detector, for which another scintillator was used. In case both of these detectors show a signal, both scintillators also need to show a signal because the triggering particle necessarily passes through them. The detection efficiency for any of the two scintillators is defined as the fraction of total triggers, for which each scintillator produces a signal over threshold. Furthermore, three different beam positions relative to the SiPM readout have been set, as shown in figure 5.2. The detection efficiency was larger than 98 % for all the beam hit position. No dependence of the detection efficiency on the hit position could be found. For each measurement the analog data from the SiPMs was converted to a digital signal in a QDC. The distribution of this signal in each case followed a Landau distribution. The most probable value of this distribution was dependent on the beam hit position and it was decreasing with increasing distance between the hit position in the readout. This means the scintillation light losses over the length of the scintillator have a measurable effect. Due to the 16 cm difference in
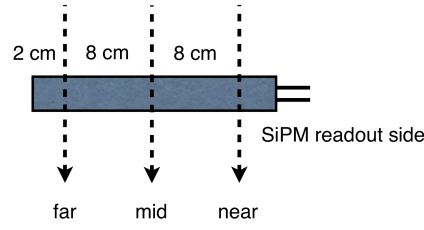
46

Figure 5.2.: 3 different beam positions for the tests of the scintillators at the Beam Test Facility.

beam hit position, the signal was decreased further away from the SiPM readout to 93 % and 87 % for the two scintillators. The signals from the SiPMs were converted into time stamps by a TDC. By comparing these time stamps to a reference time stamp from the trigger, a time resolution of 2.6 ns (FWHM) could be estimated.

5.2. Test Measurements at SMI

After first tests at LNF, the setup box as well as the scintillators and the two SDD arrays which originally belonged to the SIDDHARTA experiment were transported to the Stefan Meyer Institute in Vienna in summer 2014. Tests were done with the SDDs in a smaller setup, but due to problems induced by Wi-Fi signals, which were most likely picked up due to the similarity of Wi-Fi wavelength ($\sim$ 12 cm) and setup geometry, these tests were abandoned.

Subsequently, SDD tests were conducted with an adapted readout board in the final setup box, which was larger and therefore less likely to pick up Wi-Fi signals. The final argon cooling system for the SDDs was assembled and taken into operation. The Cu target was mounted together with its water cooling system. The scintillators were wrapped in aluminum foil and black tape and two SiPMs were attached to a surface with optical glue and read out in series. The slow control was set up including the current supply, the temperature controller, the Pt-100 temperature sensors and pressure sensors, as described in 3.4.2. The PID values of the LakeShore331 temperature controller were adjusted to ensure stable operation. The data acquisition system was set up and connected to the signals from the SDDs and the SiPMs. The gain and shaping time of each SDD channel was was adjusted in the CEAN 568B spectroscopy amplifier.

After all these parts were tested individually, they were assembled and long term

tests were conducted which will be described subsequently. These test in the final experiment configuration were crucial in order to test and determine performance characteristics of the subsystems and to ensure long term stability of the operation of the experiment.

5.2.1. Water Cooling of Cu Target

The water cooling was tested to ensure adequate temperature of the Cu target also in the case of a high current. The cooling of the target is done by water flowing through the cooling pad between the two copper target foils. The temperature was measured on each foil with a Pt-100 temperature sensor. Two different measurements with a high current were done, one time with water cooling and once without water cooling. The outcome is shown in figure 5.3.
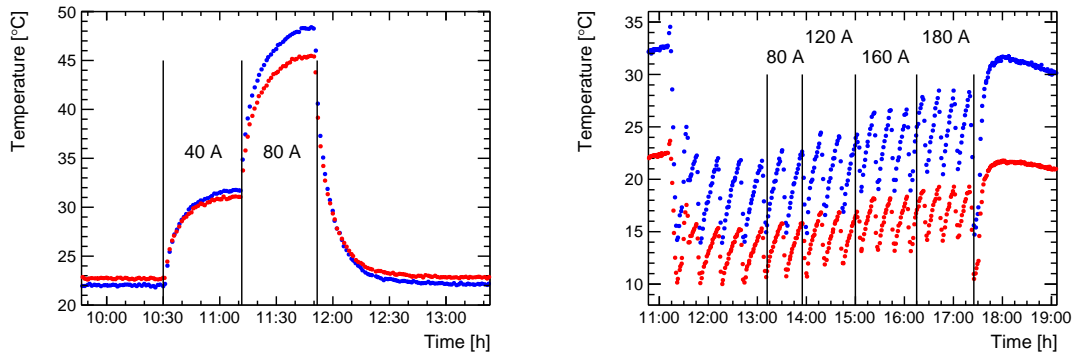

Figure 5.3.: The temperature of the two Cu target foils (red and blue) with a high current without water cooling (left) and with water cooling (right).

The left figure shows the temperatures without the water cooling with a current of 40 A (starting at ∼ 10:30) and a current of 80 A (starting at ∼ 11:15). The temperature rises to ∼ 45 °C, well above room temperature. As an even higher current of 100 A is projected, it is not an option not to use water cooling. On the right picture the temperature of the Cu target with water cooling is shown. In this case the current was varied gradually from 80 A (starting at ∼ 13:00) to 180 A (starting at ∼ 16:00). In this case the temperature can be stabilized below room temperature even for a current as high as 180 A. Consequently, similar temperatures of the target can be achieved for data taking with and without current.

5.2.2. Argon Cooling of Silicon Drift Detectors

The argon cooling of the SDDs was tested in many test runs at the Stefan Meyer Institute. The Pt-100 temperature sensors were mounted on the aluminum support structure of the SDDs, which is in thermal contact with the detectors. During these data taking periods, the temperature of the detectors could be kept constant at around -170 °C, except for short periods of higher temperature, with a duration of a few minutes typically. The reason for these sudden temperature changes is still unclear. The temperature for both SDD arrays during 1 day of data taking is shown in figure 5.4. As the scheduled operation temperature is 150 K [35] ($\sim$ -120
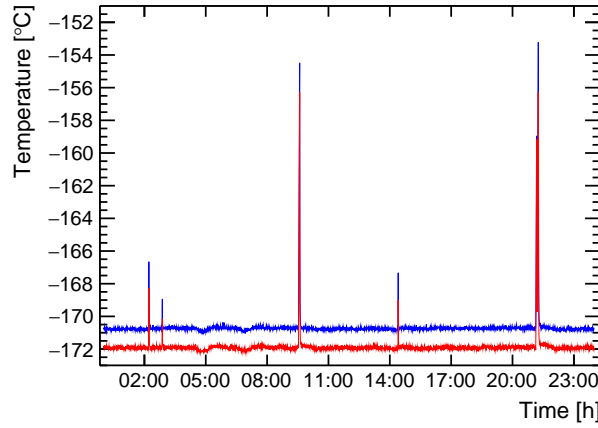

Figure 5.4.: Temperature of the two SDD arrays during one day of data taking at the Stefan Meyer Institute.

°C), which is still higher than during the periods with higher temperature, the performance characteristics of the detectors are not not affected by these changes. But nevertheless this problem was solved in the measurement at the Gran Sasso National Laboratory by adding a bit more argon to the cooling system, which ensured stable data taking conditions at an SDD temperature of around 100 K.

5.2.3. Scintillator Energy Deposition Trigger Threshold

To estimate the minimum energy that needs to be deposited in the scintillators by ionizing radiation in order for the event to be detectable, we used a Caesium-

137 [1] source shining directly into plastic scintillators used in the VIP2 experiment parallel to their length axis. A 2 mm aluminum plate was mounted between the source and the scintillator in order to shield the β radiation from the source. The scintillators were read out by two serially connected SiPMs on the opposite side of the source. The pulse-height spectrum of the SiPMs was recorded with an oscilloscope. The setup was modeled in the Geant4 framework and the energy deposited in the scintillator was recorded. The deposited energy was smeared in the simulation by 10 % to account for the finite resolution of the detection system. The pulse-height spectrum from the oscilloscope and the MC-spectrum are shown in figure 5.5. The pulse-height spectrum was recorded once with and once without
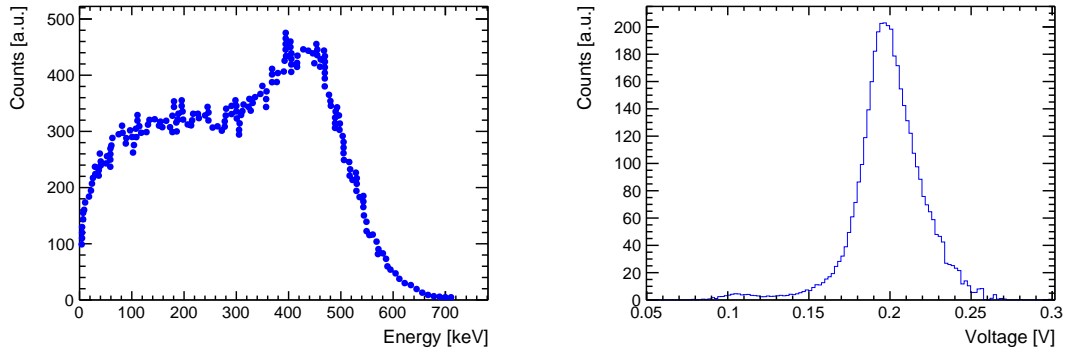

Figure 5.5.: The energy spectrum from a Cs-137 source deposited in the scintillator from MC simulations (left) and the pulse-height spectrum recorded with an oscilloscope (right). The part of the pulse-height spectrum below approximately 180 mV is cut off due to the trigger settings of the oscilloscope.

the source. The subtracted spectrum was calculated in order to get the isolated spectrum from the source without events from external radiation. This subtracted spectrum is shown in the plot.

In the energy region of $\sim$ 80 keV - $\sim$ 4 MeV (which includes the photons from the Cs-137 source) the dominant energy-loss mechanism for photons in a plastic scintillator is the Compton effect [37]. Therefore, not the whole energy of the photons is deposited in the detector. The falloff in the MC-spectrum corresponds

---

[1]Cs-137 decays to a metastable Barium-137 state via β^- decay with a half-life of approximately 30 years. This state then decays into a stable state via emission of a 662 keV photon.

to the Compton edge [2]. The single Compton edge of 662 keV photons is at 478 keV, higher energies in the MC-spectrum come from Multi-Compton processes and from the smeared energy resolution.

The falloff in the pulse height spectrum at ~ 200 mV corresponds to this Compton edge. The part below ~ 180 mV is partly cut from the spectrum due to the trigger settings of the oscilloscope and does not have any physical meaning. From this measurement a relation between deposited energy and output pulse height of:

$$\frac{\text{Energy}}{\text{Pulse Height}} \approx \frac{500 \text{ keV}}{200 \text{ mV}} = 2.5 \frac{\text{keV}}{\text{mV}}. \tag{5.1}$$

Furthermore, the threshold settings in the experiment at LNGS were set to approximately 40 mV. They could not be set lower than this, as at lower thresholds the rate of dark counts rises and this needs to be avoided. With $2.5 \frac{\text{keV}}{\text{mV}}$ a threshold of 40 mV corresponds to a deposited energy of 100 keV. This energy is used as a threshold for MC simulations, which were discussed in chapter 4. For the measurements at SMI the SiPM thresholds were set higher, as at this point the goal was to detect events induced by cosmic radiation, which have a typical energy deposit of a few MeV.

There are a few assumptions going into this calculation, as for example the linearity of the relation between deposited energy and output pulse height. Therefore, the value of 100 keV energy deposition threshold at LNGS should be viewed as an estimation rather than a fixed value.

5.2.4. SDD Energy Resolution

The following tests of the functionality of all parts are extracted from a data taking period from 23. October 2015 - 27. October 2015 at SMI, corresponding to 4 days of data taking time. There was no current flowing through the copper target during this data taking period.

To achieve the optimal energy resolution, the voltage values for the photon entrance window (Bc) and the separation mesh (Bf) (see chapter 3.1) were adjusted before this data taking period, starting from the values used in the SIDDHARTA setup

---

[2]When a photon scatters on a charged particle, the energy it transfers to the charged particle depends on the angle between incoming and outgoing photon. The maximum energy is transfered when the photon changes direction by $180°$. As a photon can not deposit more energy in a single process, this energy marks an "edge" in the detected spectrum.

for these SDD cells. The values used are summed up in tables 5.1 and 5.2.

Rx	R1	Bf (SDDs: 1,2,3)	Bf (SDDs: 4,5,6)
-250 V	-16 V	-137 V	-144 V

Table 5.1.: Voltages for outer and inner SDD rings as well as for the separation meshs of the two SDD arrays.

Bc1	Bc2	Bc3	Bc4	Bc5	Bc6
-134 V	-121 V	-143 V	-133 V	-137 V	-144 V

Table 5.2.: Voltages for the photon entrance windows for SDDs 1-6.

After optimizing the voltage settings, the energy resolution was determined from the the data taking period in October 2015. The results are shown in table 5.3. The analysis technique used to find the energy scale and the energy resolution will be described in detail in section 6.2. The typical statistical error of the Full Width

	SDD 1	SDD 2	SDD 3	SDD 4	SDD 5	SDD 6
FWHM @ 6 keV	148 eV	150 eV	147 eV	147 eV	156 eV	158 eV

Table 5.3.: Energy resolution (FWHM) of the SDDs at 6 keV.

Half Maximum (FWHM) energy resolution is 1-2 eV for this amount of data for one SDD. These energy resolutions are close to the design resolution of 150 eV (FWHM) at 6 keV given in [35]. The summed up energy spectrum is shown in figure 5.6.

For in-situ calibration, an Fe-55 source creates two sources of calibration (see also section 3.1). On the one hand, the photons from the source directly hit the SDDs and on the other hand, they excite photons from a 25 μm thick titanium calibration foil, which is placed in between the source and the detector. The Mn Kα and Kβ lines (5.9 keV and 6.5 keV) from the Fe-55 source and the Ti Kα and Kβ lines (4.5 keV and 4.9 keV) from the Ti calibration foil are visible in the figure. The Mn Kα and Ti Kα lines are used to find the energy scale. Details to the calibration procedure will be given in chapter 6. Furthermore, the silicon Kα escape peak [3] of the Ti Kα line is visible 1.7 keV below its main peak at around 2.8 keV. The Cu Kα line at 8 keV is caused by external radiation hitting the Cu parts and

---

[3]A Si Kα photon escapes the detector. Its energy is therefore not converted into electron/hole pairs and is missing in the spectrum.
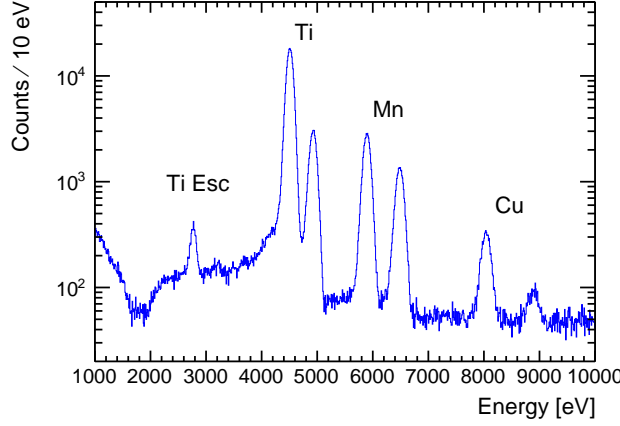
Figure 5.6.: Energy spectrum corresponding to 4 days of data taken at SMI.

creating vacancies in the 1s shell which are subsequently filled by electrons from the 2p shell. As the thermal energy at room temperature (~ 25 meV) is orders of magnitude smaller than the gap between the 1s and the 2p shell (~ 8 keV), the creation of a vacancy in the 1s shell is reliant on an external energy source. All the expected peaks are therefore visible in the spectrum and the functionality of all six SDDs could be established.

5.2.5. SDD Time Resolution

For the measurement of the time resolution of the Silicon Drift Detectors, the arrival times of the digitized signals from the SDD "OR" and the "AND" of inner and outer scintillator layer at the TDC were compared. For details about the DAQ system see figure B.1 or section 3.4. As mentioned in 3.2, the time resolution of the scintillators read out by SiPMs is smaller than the one of the SDDs by around two orders of magnitude and is neglected here. The events in which both SDDs and and scintillators produce a signal are mainly caused by charged particles which first hit the scintillators and then either directly hit the SDDs or cause secondary radiation (e.g. bremsstrahlung in the scintillators), which in turn hits the SDDs. In either case the time difference of the actual hits of the radiation in scintillators and SDDs is also negligible compared to the time resolution of the SDDs. The difference in arrival times at the TDC between the two signals are shown in figure 5.7. The plot corresponds to all events with scintillator and SDD coincidence for the data taking period of 4 days at SMI. The time resolution was found to be

around 380 ns (FWHM). This is in agreement with the specification of a time resolution $\leq 1~\mu$s given in [35]. Furthermore, the mean delay of the arrival of the SDD signal is 290 ns and the maximum drift time is approximately 1 μs.
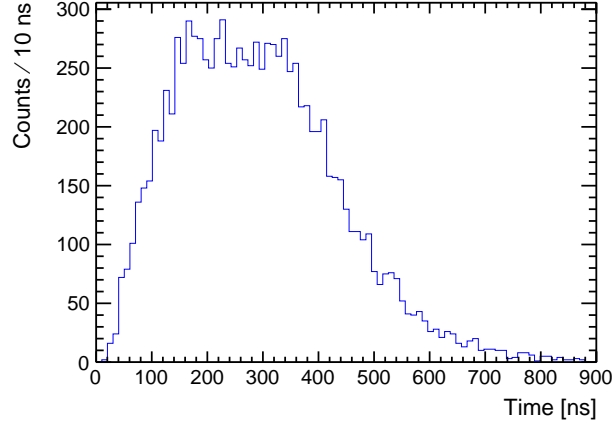

Figure 5.7.: Arrival time of the signal of Silicon Drift Detectors relative to the signal from the SiPMs corresponding to a time resolution of $\sim$ 380 ns (FWHM).

5.2.6. Scintillator plus SiPM Time Resolution

For the mentioned 4 day data taking period, the difference in arrival times of signals from the adjoining "bottom inner" and "bottom outer" layer are shown in figure 5.8. The distribution of the difference of the arrival times can approximately be modeled by a Gaussian distribution with a $\sigma = 1.33$ ns (3.13 ns FWHM). Assuming the time resolution is the same for both of these layers, this results in a $\sigma = 0.94$ ns (2.2 ns FWHM) for each layer and therefore also for each scintillator plus SiPM readout system.

5.2.7. Detection Efficiency of Cosmic Radiation and Active Shielding Test

The data used for this test is again from the 4 day data taking period in October 2015 at SMI. The test was done in order to determine the detection efficiency
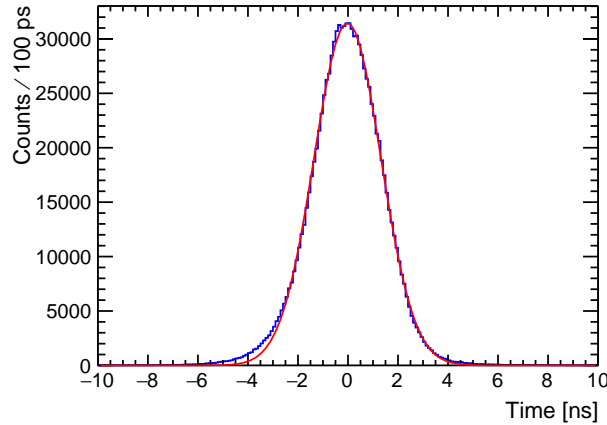
Figure 5.8.: Difference of arrival times of two different scintillator layers with Gaussian fit function ($\sigma = 1.33$ ns).

of the active shielding system for particles from cosmic radiation going through the scintillators. The energy calibration procedure, which is needed to determine the energy of each SDD event, will be discussed in section 6.2. The first step was to determine if any scintillator detected less events than other scintillators. For this purpose the QDC spectra, which correspond to the charge deposited in the scintillator in each event, of each scintillator were investigated. One of these spectra with two different scales is shown in figure 5.9.
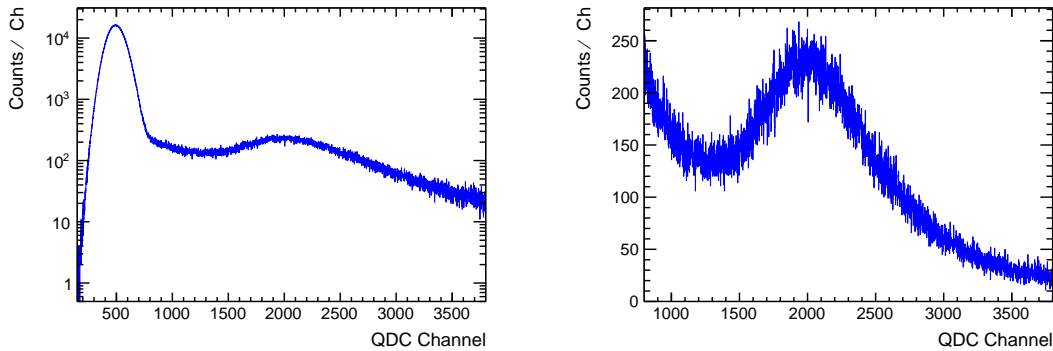

Figure 5.9.: Spectrum of charge collected by the QDC for one scintillator once in logarithmic scale (left) and once in linear scale (right).

The left figure shows a large peak on the left side. In these events the collected charge was low so it can be deduced that no ionizing radiation hit the scintillator. Starting from approximately channel 800 there is a bump in the spectrum. For

55

these events the collected charge was high and it can be said that there was most likely ionizing radiation hitting this scintillator. To approximately determine the number of events in each scintillator, a threshold channel is introduced, above which all events where counted as signal events. This channel was determined as the 3σ deviation from the mean value of the "No-Signal" gaussian distribution. In this case the threshold channel is 800. It is interesting to compare the collected charge distribution to the distribution of energy deposited in the scintillators by cosmic radiation, which is shown in figure 4.3. The peak in the QDC spectrum at channel 2000 corresponds to a deposited energy of around 8 MeV.

The distribution of the counts determined in this way is shown in figure 5.10. The histogram is filled at positions corresponding to the positions of the scintillators in the setup, as they are shown in figure 3.5. One thing to note is that scintillators on the edge of the setup have less counts on average. This is due to the fact that for an event to be triggered, the inner and outer scintillator layer need to have a signal. Taking into account the angular distribution of cosmic radiation which is $\propto \cos^2(\theta)$ [42], there is a chance of particles hitting for example the scintillator in column 1 and layer 5, but not hitting any other scintillator, thus not generating an event. This effect is not important for more central scintillators, like for example the one in column 3 and layer 4. For all these scintillators the number of hits is approximately 380.000 on average, which corresponds to a rate of 1.1 Hz in each scintillator. Comparing this rate to the 1.67 Hz extracted from [42], it is obvious that the system of scintillators detects less events than expected. This might be due to the shielding of the aluminum enclosure and the multistory building above the setup. But from this plot one can say that all scintillators are working and giving signals.

To evaluate the detection efficiency for ionizing radiation, events were investigated in which at least 3 of the 4 scintillator layers with six scintillators (e.g. "top outer") had a signal. For these events the probability was measured that also the 4th layer had a signal. It turned out to be ~ 90 %. A reason for this number not being higher might be that a part of the events are introduced by γ radiation, for which the detection efficiency is very low as was mentioned in 4.3. This radiation could introduce events in some scintillators, while in others it does not. Another factor might be differences in gain settings of the SiPMs and trigger threshold settings for the SiPM signals. These differences can again lead to radiation triggering signals only in a part of the scintillators.

To ensure that the active shielding system is working as expected, it is interesting to look at hit patterns. For this purpose all events for which one specific scintillator has a signal are selected and then all events (from the previously selected events)
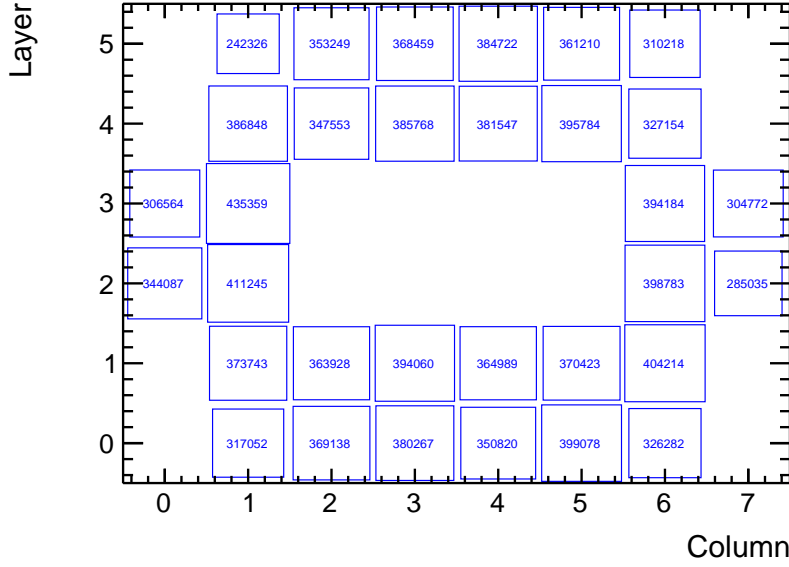
Figure 5.10.: The number of signals in each scintillator for a data taking period of 4 days.

every other scintillator produces are counted. In figure 5.11 a hit pattern for the scintillator in column 2 and layer 5 is shown. It can be seen that for most events in this scintillator, the scintillator below also has an event, meaning most particles go through the setup almost vertically. Other scintillators not being directly below the specific scintillator get hit less often. The distribution resembles the $\cos^2(\theta)$ distribution of cosmic radiation mentioned in [42]. As the hit patterns for all scintillators look as expected, it can be assumed that all scintillators are connected properly and working fine.

Another test was done comparing the SDD spectrum of the events rejected by scintillator veto to the simulated spectrum introduced in the SDDs by cosmic muons and rejected by scintillator veto, which was already shown in figure 4.4. The expectation was, that these spectra should be similar as a big part of the rejected events in the measurement are the ones introduced by muons. The two spectra are shown in figure 5.12. One thing to note is that in the energy region from about 15 - 25 keV the two spectra are quite similar with approximately 1-2 counts per 100 eV. In the energy range where the scintillator veto is crucial, the region of the forbidden Cu Kα transition below 15 keV, there are more SDD hits rejected than there are predicted hits from cosmic radiation (consider the logarithmic scale on the right figure). This most likely means that the scintillator
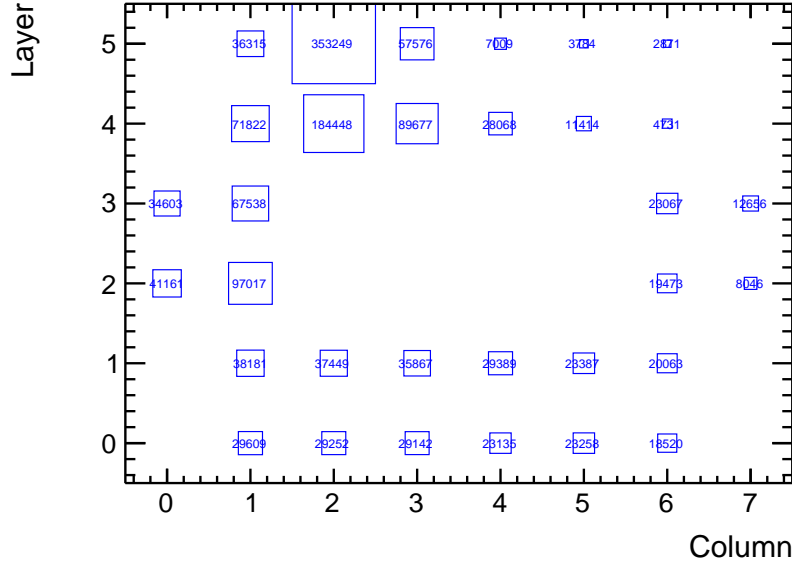
Figure 5.11.: Hit pattern for scintillator in column 2 and layer 5.

veto can also reject at least a small part of the γ radiation which is present in the laboratory. Consequently, the system is not only capable of what it was designed for, namely detecting high energy ionizing radiation, but also detecting a part of the γ radiation.

Finally it is interesting to look at the amount of hits in the SDDs which are in coincidence with a scintillator signal. The spectrum together with the rejected events is shown in figure 5.13. It is obvious that only a small fraction of the SDD events can be rejected by scintillator veto. For example in the region of the the Cu lines from 7 - 10 keV a fraction of ~ 1 % of events is seen in the scintillators. This rejection ratio means that the vast majority of counts in this energy region is caused by external photons, which can only be rejected to a small part. For the part below 7 keV the Fe-55 source inside the setup contributes most of the counts, which can not be rejected. Therefore, it does not make sense to calculate a rejection ratio for this energy region. The higher the energy the higher the contribution of charged particles, with a high detection efficiency in the scintillators, to the SDD events. In the overflow bins of the SDDs, corresponding to an energy higher than around 30 keV, the rejection ratio is 6.5 %. The fact that the contribution of charged particles to the background is proportional to the energy can be seen comparing figures 4.4 and 4.6. While the peak contribution of charged particles is at around 300 keV, the contribution from external γ radiation is high from ~ 0 - 70 keV,
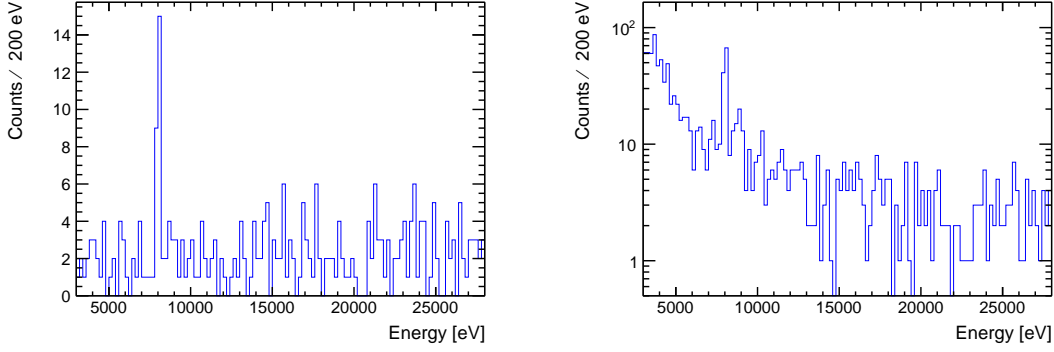
Figure 5.12.: The energy spectrum corresponding to 4 days of data introduced by cosmic radiation above ground from simulation (left) and measured (right).

with a maximum on the low energy side.

Despite the rejection ratio, which might be smaller than expected, the scintillators were kept inside the setup. On the one hand, they offer a passive shielding effect, as they represent at least 8 cm of plastic scintillator between the source of a possible background radiation outside of the setup and the SDDs. On the other hand, for future measurements of the VIP2 experiment in the underground laboratory in Gran Sasso, a passive shielding consisting of Cu and Pb blocks will be mounted around the setup. This will possibly bring the background from γ radiation to a level comparable to the background from cosmic radiation, which can be rejected. In this case the active shielding will improve the result of the measurement.

The test of the active shielding system has shown that the detection of charged particles works with $> 90\,\%$ efficiency. All scintillators were found to work properly and contribute to the rejection of external radiation. But as the main background at SMI apparently comes from γ radiation, for which the scintillator detection efficiency is low, the background rejection ratio is approximately $1\,\%$ in the energy region of the forbidden transition.

As all tests mentioned above gave the expected results it can be concluded that all detectors and parts of the data acquisition are working as expected. A summary of the outcome of some of the tests discussed in this chapter can be found in table 8.1. Crucial parameters of the experimental setup like SDD scale linearity and peak position stability will be discussed in the the following chapter.
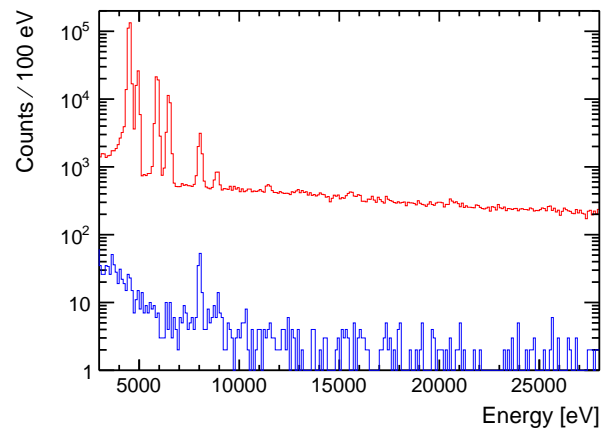
Figure 5.13.: The energy spectrum corresponding to 4 days of data at SMI (red) and the part of the spectrum rejected by scintillator veto (blue).

6. Data Taking at LNGS and Data Preparation

After exhaustive tests at the Stefan Meyer Institute, the VIP2 experiment was transported to the Laboratori Nazionali del Gran Sasso of INFN in November 2015. The laboratory is located beneath the Gran Sasso mountains in the Italian Abruzzo region. The Apennine mountains above the laboratory provide a natural shielding from cosmic radiation corresponding to 3800 m water equivalent depth [44]. The flux of cosmic muons in the underground laboratory is reduced compared to the flux above ground by approximately 6 orders of magnitude (see also chapter 4). The dominant background radiation for the experiment therefore does not come from cosmic radiation, but from γ radiation originating from radioactive isotopes like ^{238}U, ^{232}Th or ^{40}K and their decay products. These isotopes are part of the rocks and the concrete used to stabilize the cavity. The background reduction due to the shielding of the mountains is crucial for improving the final limit on the probability for the violation of the Pauli Exclusion Principle the experiment is able to set, as this limit is proportional to the square root of the background. A comparison of the spectra taken at Stefan Meyer Institute and at LNGS is shown in figure 6.1. The counts in the energy region of the forbidden transition at approximately 7.7 keV, just below the Cu Kα peak, are reduced by a factor of 5. In the region below 7 keV, the counts do not change drastically, as in this energy region most of the events are caused by X-rays from the Fe-55 source and the titanium calibration foil. These counts are similar, as the source rate is the same at SMI and LNGS (apart from a slight decrease in the rate of the source due to its half-life of 2.7 years).

After some tests in November 2015 and a break over the Christmas holidays, the first data without current was taken in February 2016 at LNGS. After a period of further tests and maintenance and a data taking break in summer 2016, the first data with current was taken in October 2016. Data taking continued with various breaks for maintenance until November 2017. Until the end of July 2017, a total of 116 days and 20 hours of data without current and 81 days and 10 hours of data with a current of 100 A have been taken at LNGS, which are analysed in this work.
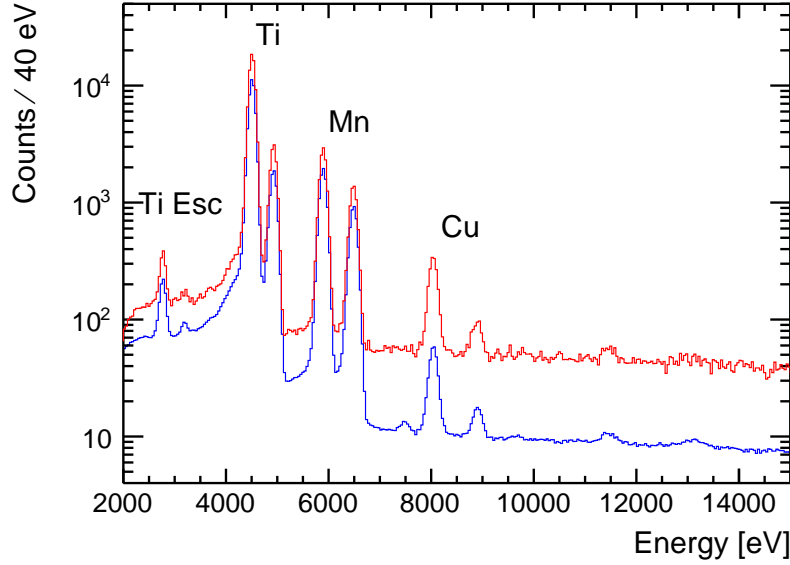
Figure 6.1.: The complete spectra from SMI (red) and LNGS (blue) both scaled to 1 day of data taking time. The data corresponds to 4 days for the SMI data and to 198 days in the case of LNGS (hence the difference in statistical errors in the single bins).

During this data taking campaign, periods with 100 A of current flowing through the target were alternated with periods without current. The typical length of one of these periods was one week. The current could be turned off and on remotely as was described in section 3.4.2. It is also important to note that in upcoming figures like 6.2, in which the x-axis corresponds to the time of the data taking starting from February 2016 until July 2017, each data point corresponds to a certain quantity (event rate, peak position, temperature and energy resolution) averaged over one day of data.

6.1. Data Selection

The selection of events is important in the VIP2 experiment. First SDD events were discarded which occurred in coincidence with an active veto signal. This will be discussed in more detail in chapter 6.5.

Furthermore, events were neglected which occurred in a time of a higher than

normal background rate. Excluding any possible source of background, which causes events in the energy region of the forbidden Cu Kα transition, is important as it complicates finding candidate events from this transition. Figure 6.2 shows
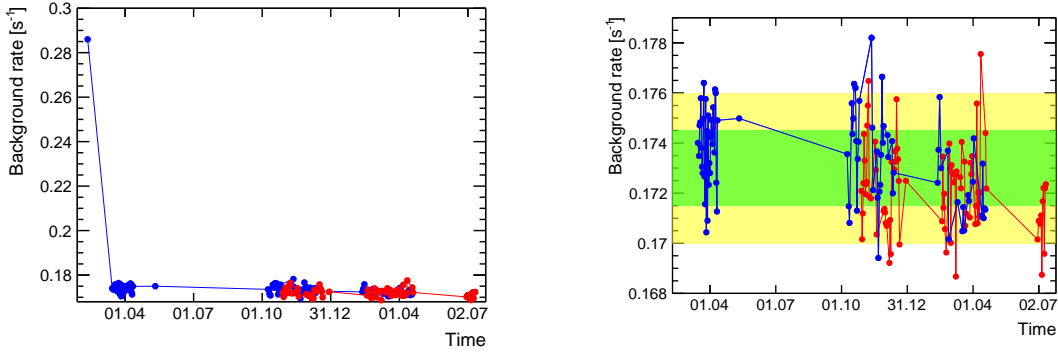

Figure 6.2.: The rate of events with an energy deposit larger than 7 keV in any SDD for the complete dataset (left) and for the cleaned dataset (right). Data with current is shown in red, data without current is shown in blue. 1σ and 2σ statistical uncertainties from the mean are shown in green and yellow. Each data point corresponds to one day of data. The x-axis spans a time from February 2016 until July 2017.

the rate of events with an energy deposit above 7 keV in any SDD. Each data point in the figure corresponds to the rate of these events, averaged over a whole day. The rate of events with an energy lower than 7 keV is dominated by events caused by the Fe-55 source. The left picture corresponds to a dataset starting around the 11th of February 2016. A period of higher event rate by a factor of about two in the time around the 11. February 2016 is visible. The reason for this increase is not clear. These data were left out in the data analysis. The same event rate (any SDD has a signal larger than 7 keV) without these data is shown in the right picture of figure 6.2. The rate is stable throughout the whole period, within statistical uncertainty. The 1σ and 2σ error bands are shown in the plot. As approximately 95 % of the data points lie within the 2σ statistical uncertainty, systematic effects changing the background rate in subsets of data can be excluded (see for example [47]). The statistical uncertainty was calculated from the assumption, that the number of background events per day follows a Poissonian distribution, meaning its error is the square root of its mean value. Systematic uncertainties are briefly discussed in A.

It is interesting to look at the rate of events with an energy smaller than 7 keV, which are caused mainly by the Fe-55 source. Due to its half-life, events from the
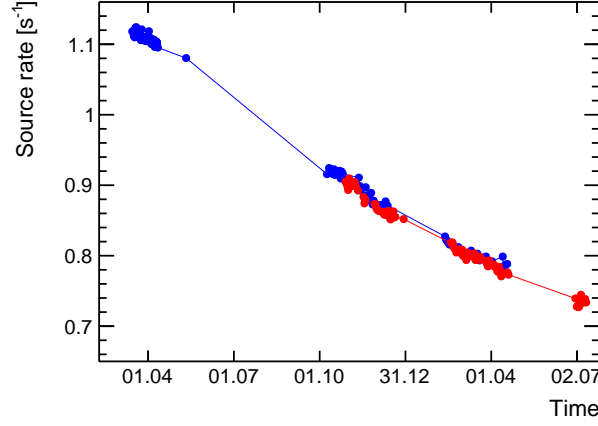
Figure 6.3.: The rate of counts caused by the Fe-55 source for the data with current (red) and without current (blue). Data points from these two datasets are overlapping due to similar rate. The rate is decreasing due to the half-life of Fe-55 of 2.7 years. Each data point corresponds to an average over one day of data.

source decrease by a factor of approximately 0.65 in the course of the data taking of 1 year and 5 months.

Events in the SDDs originating from a Pauli-forbidden transition are expected to hit only one SDD as only one photon is produced in the course of this process. Therefore, all events with a SDD hit multiplicity larger than one can be excluded when looking for those photons. The vast majority of events has an ADC multiplicity of one, from which in turn the vast majority comes from the Fe-55 source. Additionally there are events caused by the environmental γ radiation and possibly events from non-Paulian transitions in the spectrum with 100 A current, which also have a SDD hit multiplicity of one. All these are used for the analysis.

A possibility of signals in two SDDs is a hit on the border of one SDD, where a part of the generated charge is transfered to the neighboring SDD. Events of this kind can be illustrated with the energy correlation between SDDs, as shown in figure 6.4. Here the charge generated by a photon either directly from the Fe-55 source or the Ti foil is split and drifts to the anodes of two neighboring SDDs. The energy equivalent to the total deposited charge equals the energy of one of the calibration lines. Consequently, these lines run diagonally through the figure. The probability of finding events with an energy deposit in two SDDs is approximately 0.5 %, compared to events with a multiplicity of one. Events with
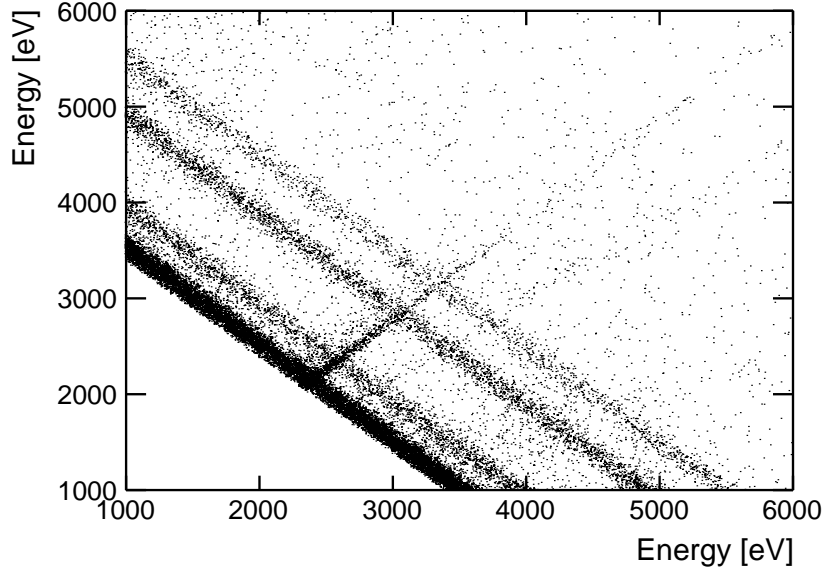
Figure 6.4.: Energy correlation between two neighboring SDDs. The Ti and Mn lines are visible on lines with a constant sum of energy due to charge sharing between adjoining detectors. Low energy parts are cut from the figure to enhance visibility.

SDD multiplicity 3, 4 and 5 do practically not occur. Nevertheless, there are events with SDD multiplicity six, which are probably caused by noise. This noise might be picked up from the environment (e.g. Wi-Fi, power grid).

The events that were not included in the analysis were the ones which:

- were in coincidence with scintillator veto

- had an SDD multiplicity higher than one

- were recorded in a time in which the background was higher than normal

6.2. Energy Calibration

As the goal of the VIP2 experiment is to count events in the energy region of the Pauli-forbidden Cu Kα transition, the determination of the energy of each SDD

hit is of utmost importance. Assigning for example an energy of 7.7 keV to an event coming from a photon from a normal Cu Kα transition at 8.05 keV changes the outcome of the experiment and has to be avoided. Furthermore, the energy resolution should be kept as close as possible to the intrinsic energy resolution of the detectors. A drift of the peak position is one of the effects that leads to a deterioration of the energy resolution.

An energy calibration of the detector is the conversion from the primary spectrum in ADC channels into energy in electron volt. For this purpose the position of the Mn Kα and Ti Kα peak are determined in the primary ADC channel spectrum. As the energies of these peaks are known, a linear relation between ADC channel and energy can be inferred. This relation can for example be written as

$$E(i) = 4510.8 + \frac{5898.8 - 4510.8}{i(MnK\alpha_1) - i(TiK\alpha_1)} \times (i - i(TiK\alpha_1)), \qquad (6.1)$$

where E is the energy in electronvolt to be calculated, i is the measured ADC channel of a specific event, 4510.8 eV and 5898.8 eV are the known energies of the Ti Kα_1 and Mn Kα_1 lines and $i(TiK\alpha_1)$ is the ADC channel of the Ti Kα_1 line. The ADC channel of every event is then scaled according to this linear relation into an energy. To determine the position of the peaks as precisely as possible, the complete spectrum is fit, taking into account all features of a real detector. This fit function will now be discussed.

In the fitting procedure, the relation for the energy resolution, which is only dependent on Fano noise and constant noise is assumed (see also chapter 3.1):

$$\sigma(E) = \omega \sqrt{W^2 + \frac{FE}{\omega}}, \qquad (6.2)$$

where ω is the energy needed to create an electron hole pair in silicon, which is 3.81 eV at 77 K [37]. W denotes the contribution to noise independent from energy and F is the Fano factor.

Photons from a monoenergetic source cause a complex spectrum in a real detector. For silicon detectors they were described for example in [48] and [49]. The main feature is the *Gaussian peak*, corresponding to the case in which all electrons that are produced by the incident photon are collected at the anode. The width of this Gaussian is determined by the intrinsic detector resolution and the natural linewidth. The natural line shape is a Lorentzian with a width of typically a few eV FWHM [50]. The intrinsic detector resolution gives rise to a Gaussian line shape with a width of approximately 100 - 200 eV FWHM, depending on the energy.

The real line shape is then a convolution of these two shapes, which would be a Voigt function. As the intrinsic detector resolution is by far larger than the natural linewidth, the latter contribution is small and the shape can be approximated by a Gaussian function. On the low energy side of the main Gaussian peak, there is a structure in the spectrum which is caused by incomplete collection of the charge generated by the detected radiation. The effects contributing to these structures are summed up in [48]. Qualitatively they can be described by an exponential *tail* energetically right below the main peak and a *shelf* extending from the main peak to zero energy. A *truncated shelf* extending from the energy of the main peak to smaller energy has also been described, but it was not used here. Furthermore, when the primary photon excites one Si K-shell electron via the photoelectric effect, the subsequent Si Kα photon may escape from the detector volume without contributing to the electron-hole generation. Such events contribute to the so-called *escape peak* 1.74 keV (Si Kα energy) below the main peak. *Pile-Up* effects do not play a role as the SDD event rate is as low as approximately 1 Hz (for six single channels) at LNGS. The mathematical structure of all the mentioned components is shown in equations 6.3 - 6.6 and is similar to the one used in [49]. The number i denotes the number of the ADC channel.

$$Gaussian\ Peak\ (i) = \frac{Gain}{\sigma} \times \exp(-\frac{(i - i_0)^2}{2 \times \sigma^2}) \tag{6.3}$$

$$Tail\ (i) = Gain \times tR \times tN \times \exp(\frac{i - (i_0 - tSh)}{\sigma_{tail} * tSl}) \times \mathrm{erf}(\frac{1}{\sqrt{2} * tSl} + \frac{i - (i_0 - tSh)}{\sqrt{2} * \sigma_{tail}}) \tag{6.4}$$

$$Escape\ Peak\ (i) = Gain \times eR \times \frac{1}{\sigma_E} \times \exp(-\frac{(i - (i_0 - SiK\alpha))^2}{2 \times \sigma_{escape}}) \tag{6.5}$$

$$Shelf\ (i) = Gain \times sR \times \frac{1}{2} \times \mathrm{erf}(\frac{i - i_0}{\sqrt{2} \times \sigma}) \tag{6.6}$$

Here *erf()* denotes the error function. A schematic drawing of the structure of a monoenergetic peak in the detected spectrum is shown in figure 6.5. The parameters used in equations 6.3 - 6.6 are described in detail in table 6.1.

The fits are performed using the CERN ROOT data analysis framework [51]. The code of the fit function is listed in appendix C. To find the optimal parameters, ROOT conducts a χ^2 minimization using MINUIT. The MINOS technique is used for better error estimation. The parameters are fit for the Mn Kα_1, Kα_2, Kβ and for the Ti Kα_1, Kα_2, Kβ lines. The gain ratio of the Kα_2 to Kα_1 lines is fixed to 0.51 for Mn and to 0.5 for Ti. The distance between the Kα_1 and Kα_2 lines are fixed to their physical values (converted into ADC channels). The gain and the mean value for the Kβ lines are free. The sum of all the functions is fit to the data
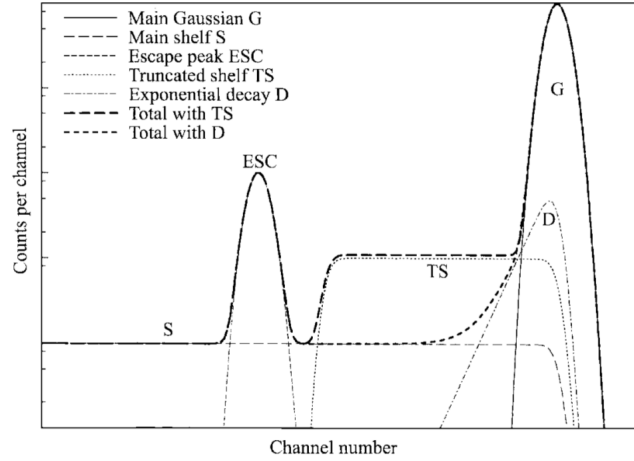
Figure 6.5.: Detected spectrum from monoenergetic incident radiation with a structure described in the text [48].

in ADC channels together with a linear part representing the background. The positions of the Mn Kα_1 and Ti Kα_1 are used to find the linear relation between ADC channels and energy. When the amount of data is high enough, the Cu Kα_1, Kα_2 and Kβ lines are fit in a similar way. Other lines shown in figures 6.16 and 6.17 are not taken into account in the fitting procedure. A typical fit with residuals is shown in figure 6.6. The reduced χ^2 of the shown fit is 1.3. From the fit the linear relation between energy and ADC channel can be derived. It is shown in figure 6.7.

6.3. Peak Stability and Data Splitting

The fitting procedure described in the section 6.2 can be used to find the peak positions in ADC channels for the Mn and Ti peaks and determine their stability. The data taken at LNGS was analyzed in this way. The result for one SDD is shown in figure 6.8, where each data point represents approximately one day of data. The peak position changes by approximately 20 ADC channels in the course of the data taking. This is a typical value similar for all six SDDs. The drift in peak position might be caused by small fluctuations of the high voltages applied to the SDDs or fluctuations of the gain of the spectroscopy amplifier, which could be dependent on the room temperature. As one ADC channel corresponds to approximately 9 eV in the final energy spectrum, the peak position changes by approximately 180 eV. In the case of the SDD for which the peak position is shown in the figure

Parameter Name	Parameter Description	Fit Parameter
Gain	Gain of the main Gaussian peak	Yes
σ	Detector energy resolution at the energy of the Gaussian peak	calculated from Fano and constant noise
σ_{tail}	Detector energy resolution at the energy of the peak of the exponential tail	calculated from Fano and constant noise
σ_{escape}	Detector energy resolution at the energy of the escape peak	calculated from Fano and constant noise
i_0	ADC channel of the main peak	Yes
tR	Ratio of the exponential tail to the main peak	Yes
tN	Norm of the exponential tail	No
tSh	Shift of the exponential tail to the low energy side	Yes
tSl	Slope of the exponential tail	Yes
eR	Ratio of escape peak to the main peak	Yes
SiKα	Energy of the Si Kα transition (1.74 keV)	No
sR	Ratio of the shelf to the main peak	Yes

Table 6.1.: Parameters going into the fit of a signal produced by monoenergetic radiation.

(SDD 3), the energy resolution at 6 keV (FWHM) would change from 151 eV for a small data set to 179 eV. This would be the resolution, in case the whole data taking time shown in figure 6.8 would be summed up in ADC channels and scaled to energy. As the energy resolution needs to be kept as good as possible in order to determine possible events in the energy region of the Pauli-forbidden transition as accurately as possible, the data needs to be divided into subsets for calibration. As small enough subsets of data are not affected by this drift, doing so avoids the problem of peak broadening in the final energy histogram due to scale drift. The strategy for determining the energy of each event as well as possible is as follows:

Finding the optimal time for the subsets of data means to optimize the energy determination uncertainty for a single event of approximately 8 keV, where the non-Paulian transition is expected. It is important to keep in mind that this calculation does not optimize how well the Cu Kα peak in the energy spectrum can be determined for calibration, as for this to be done the number of events in the Cu Kα line is not high enough. This calculation rather has the goal of optimizing the energy determination of a single event with an energy around 8 keV.
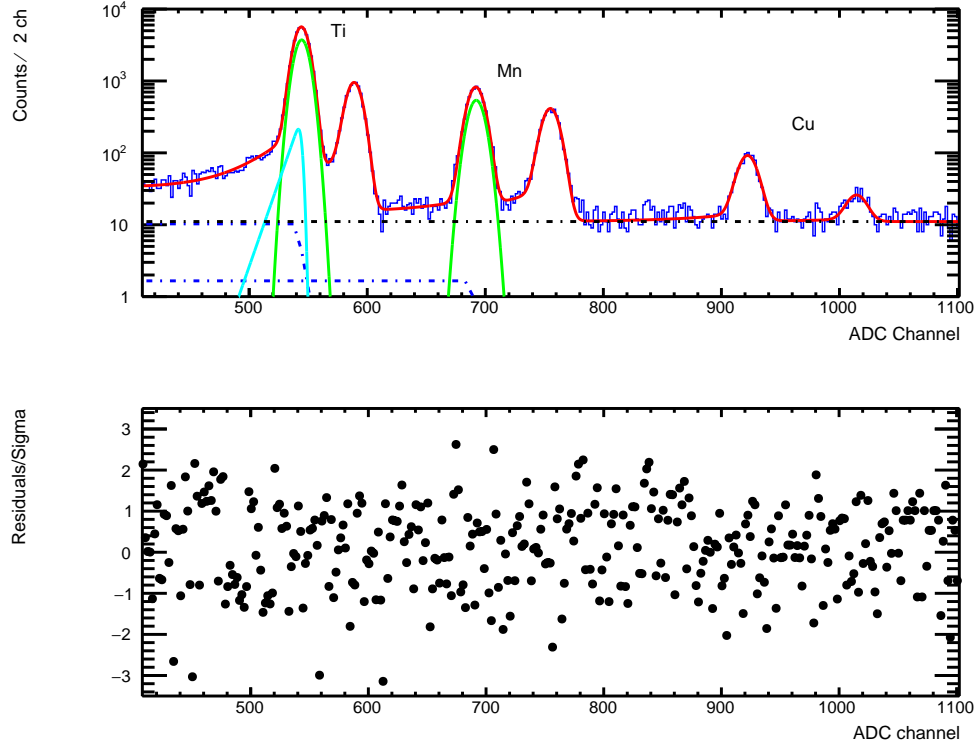
Figure 6.6.: Fit of data taken at SMI (blue) with the complete fit function (red). Some of the constituents of the fit function are shown like Ti and Mn Kα_1 peaks (green), constant background (black, dashed), Ti Kα_1 exponential tail (cyan) and the shelf functions of Ti and Mn Kα_1 (blue, dashed). Residuals divided by σ are shown below for each bin. The reduced χ^2 of this fit is 1.3.

There are two effects that need to be considered: Firstly, the intrinsic energy resolution of the detector together with the drift of the energy scale with time gives a large contribution to the energy determination uncertainty. This contribution can be estimated with formula 6.2 and the measured resolutions from the Ti and Mn lines. This effect will contribute less when the time of the data subset is low, as the effect of the peak drift is then minimized, and the energy determination uncertainty will be close to the intrinsic energy resolution. This can be seen from the right image in figure 6.9, where the contribution is called σ_{det}. The second contribution to the uncertainty in the determination of energy of an event around 8 keV comes from the statistical uncertainty of the peak position in ADC channels of the Ti Kα_1 and Mn Kα_1 calibration lines given by the fit. Taking into account the relation between ADC channels and energy (see equation 6.1) as well
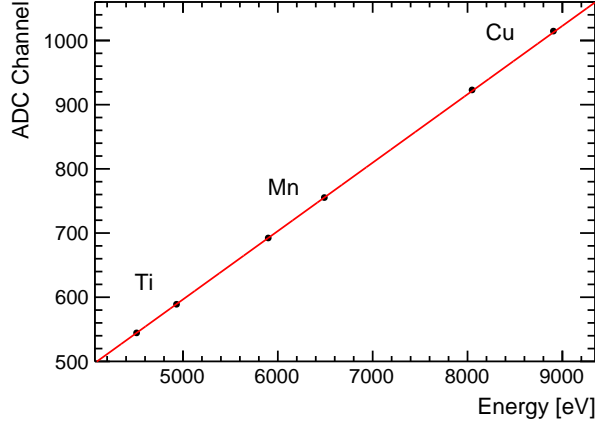
Figure 6.7.: The relation between ADC channel and energy for one SDD derived from Ti Kα_1 and Mn Kα_1 ADC channel positions and their known energies. The fitted positions of Ti Kβ, Mn Kβ as well as Cu Kα_1 and Kβ lines are also shown. Error bars are smaller than the data points.
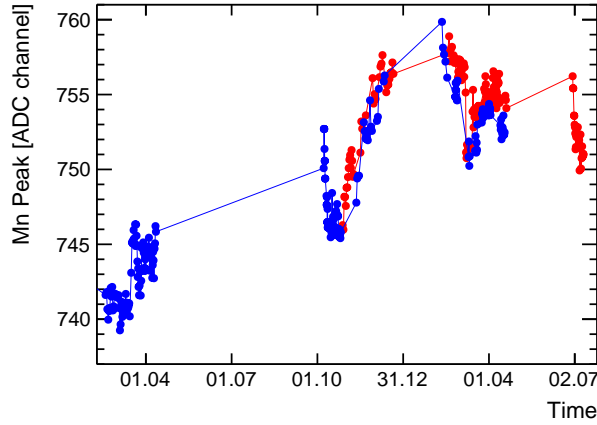

Figure 6.8.: The position of the Mn Kα_1 peak for SDD 3 during the data taking at LNGS without current (blue) and with current (red). Typical statistical error is 1 ADC channel. Each data point corresponds to one day of data.

as these statistical errors, the energy uncertainty at 8 keV can be calculated with error propagation. This contribution to the uncertainty increases with decreasing data taking time, as the statistical error of the calibration lines increases in this case. It is shown in the left image of figure 6.9, where this contribution is called

σ_{stat}. The numbers in the figure correspond to an average over all six SDDs and were calculated from a dataset of 30 days from LNGS without current, which was divided into subsets of 0.1, 0.25, 0.5, 1, 2 and 4 days. The above mentioned uncertainties were calculated for every subset and averaged. The Cu Kα line itself can not be used for calibration due to its low event rate.
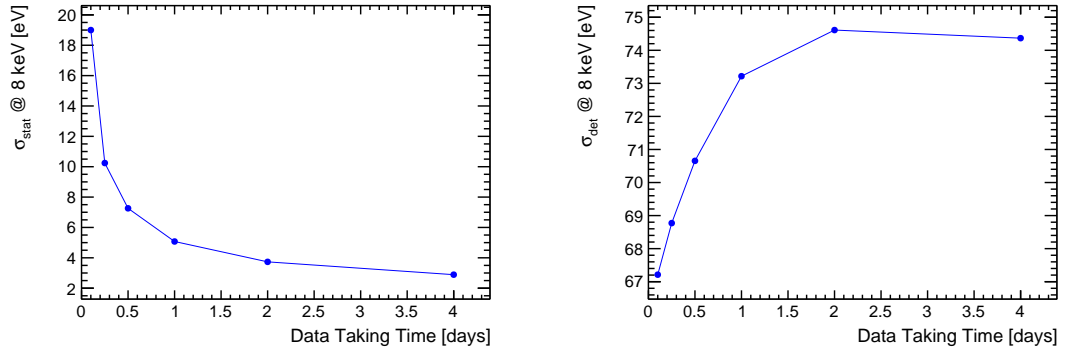

Figure 6.9.: Energy determination uncertainty at 8 keV due to statistical error of the position of the calibration lines as a function of data taking time σ_{stat} (left). Energy determination uncertainty at 8 keV due to intrinsic detector resolution, also taking peak drift effects into account σ_{det} (right).

As the two contributions (σ_{det}, σ_{stat}) are statistically independent, their variances can be added to a total energy determination uncertainty at 8 keV σ_{tot}:

$$\sigma_{tot} = \sqrt{\sigma_{det}^2 + \sigma_{stat}^2} \quad , \tag{6.7}$$

and the result is shown in figure 6.10. As the energy resolution at Cu Kα can not be measured directly due to low statistics, but needs to be calculated from the resolutions at the Mn and Ti lines, this is an estimation. The minimum energy resolution was found for a data taking time of 0.25 days or 6 hours. Therefore, the data taken at LNGS was divided into parts with 6 hours each. The 198 days and 7 hours of data were divided into 618 parts. For every one of them each of the six SDDs was calibrated separately and added up to two energy spectra, one with and one without current.
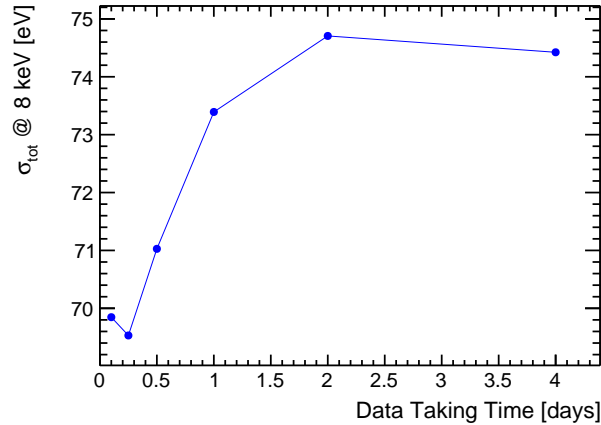
Figure 6.10.: The total uncertainty in the energy determination at 8 keV as a function of the data taking time.

6.4. Scale Linearity and 2nd Order Correction

With the Ti and Mn Kα lines as two sources of calibration it is not possible to determine if the relation between ADC channel and energy is linear over the whole spectral range. But for cases in which the Cu Kα line has enough events to determine the position of its peak, it is possible to investigate it. This is possible for example for the 4 days of data taken at SMI, for which the spectrum of one SDD is shown in figure 6.6. The relation between ADC channel and energy for this fit is shown in figure 6.7. To determine the scale linearity, it is interesting to look at the difference of the positions of the peaks determined by the fit to their positions calculated from the position of the two calibration lines. This is the equivalent of the distance between the red line (which runs through the Ti Kα_1 and the Mn Kα_1 peaks) and the data points corresponding to the fit positions of the peaks in figure 6.7. This plot is shown in figure 6.11. For a perfectly linear scale, the points should all be at zero deviation. As the Ti and Mn Kα_1 peaks are used for calibration, their deviation from the expected position is zero by definition. It is important to note that the fitted position of the Cu Kα_1 peak deviates by approximately 1.5 channels from the position it should be according to the position of the calibration lines and the known energies of the involved transitions. The same effect was observed in the data taken at LNGS. This hints to a not perfectly linear scale and the necessity to introduce 2nd order corrections into the linear relation of ADC channel to energy calculated from the position of the two calibration peaks. The
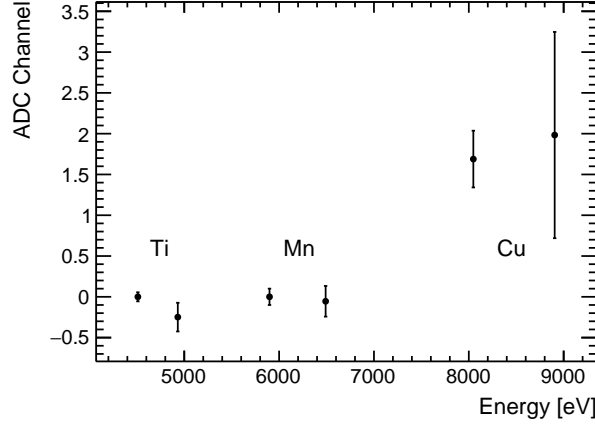
Figure 6.11.: The difference in ADC channels of the fitted position of the peaks to the position calculated with the two calibration lines and the physical position of the respective lines. The plot corresponds to 4 days of data taken at SMI with one SDD. Other SDDs show a similar result.

formula for the 2nd order correction is shown in equation 6.8.

$$i(E) = C_1 + C_2 \times E + C_3 \times E^2, \tag{6.8}$$

where C_1 and C_2 are the coefficients in the relation between ADC channel i and energy E calculated from the two calibration lines. They can be found for example by inverting equation 6.1. To calculate the coefficient C_3 for the data from LNGS, the whole data taken there was first scaled to energy with linear scaling like it was described in chapters 6.2 and 6.3 for each SDD and all subsets of data were summed up in energy. The peak position of the Cu Kα_1 position was determined in these spectra. C_3 was then determined for each SDD so that the energy scale was changed in such a way that this peak was at the correct energy. This had to be done for the complete dataset at once, as the subsets of data mentioned in chapter 6.3 do not have enough data to determine the position of the Cu Kα_1 peak. The position of this peak with a linear scale and a 2nd order scale is shown in tables 6.2 and 6.3. From the tables it can be seen that the peak position of the Cu Kα_1 peak is at its correct position of 8047.8 eV within statistical error. Nevertheless, the possible systematic error of the energy determination due to the discussed calibration procedure is mentioned in chapter A. The spectra acquired by the steps described in the chapters 6.1 - 6.4 were used for calculating the upper limit for the probability for a violation for the Pauli Exclusion Principle.

Cu Kα_1 position	SDD 1	SDD 2	SDD 3	SDD 4	SDD 5	SDD 6	Sum
Linear Scaling	8062.7 eV	8047.5 eV	8066.5 eV	8061.4 eV	8065.5 eV	8063.3 eV	8062.8 eV
2nd order correction	8046.4 eV	8047.1 eV	8047.4 eV	8049.3 eV	8049.7 eV	8047.1 eV	8048.0 eV

Table 6.2.: Cu Kα_1 peak position with linear scaling and with 2nd order scale correction for the data without current. Statistical errors are around 2 eV for single SDDs and 1 eV for the sum of all six SDDs. The true energy is at 8047.8 eV.

Cu Kα_1 position	SDD 1	SDD 2	SDD 3	SDD 4	SDD 5	SDD 6	Sum
Linear Scaling	8068.6 eV	8052.7 eV	8058.9 eV	8063.4 eV	8068.5 eV	8063.9 eV	8064.6 eV
2nd order correction	8046.9 eV	8047.2 eV	8048.0 eV	8049.7 eV	8048.9 eV	8047.2 eV	8048.0 eV

Table 6.3.: Cu Kα_1 peak position with linear scaling and with 2nd order scale correction for the data with current. Statistical errors are around 2 eV for single SDDs and 1 eV for the sum of all six SDDs. The true energy is at 8047.8 eV.

6.5. Comparison of Data and Simulations

To check if the data corresponds to the expectations, it is interesting to compare it to the simulations discussed in chapter 4. The measured counts above 7 keV together with the counts expected from simulations are shown in figure 6.12. The basis for these simulations was the γ spectrum reported in [46] with 6.3×10^8 γ m^{-2} day^{-1}. From the plot a good agreement between measurement and simulations can be observed in the constant part of the background. The constant part is interesting for the analysis described in chapter 7. The good agreement between the measured data and the simulation based on this result favors it over the result reported in [45], where approximately half the γ flux was reported. This also shows that by far the largest contribution to the counts in the region of the Pauli-forbidden transition at 7.7 keV comes from the γ radiation originating in the surrounding rocks of the underground laboratory. The agreement between data and simulation furthermore shows, that systematic effects in determining the number of events in the ROI play a minor role. Systematic uncertainties are briefly
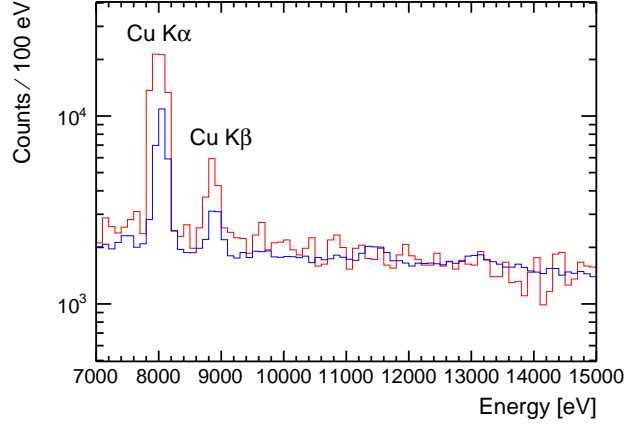
Figure 6.12.: The simulated spectrum introduced by γ radiation (red) scaled to the same data taking time (81 days 10 hours) as the data with current (blue).

discussed in A.

The scintillator rejection rate of 1 % predicted by simulations can also be compared to the measured data. The spectra taken with and without current are shown in figure 6.13 together with the counts that can be rejected by scintillator veto. The
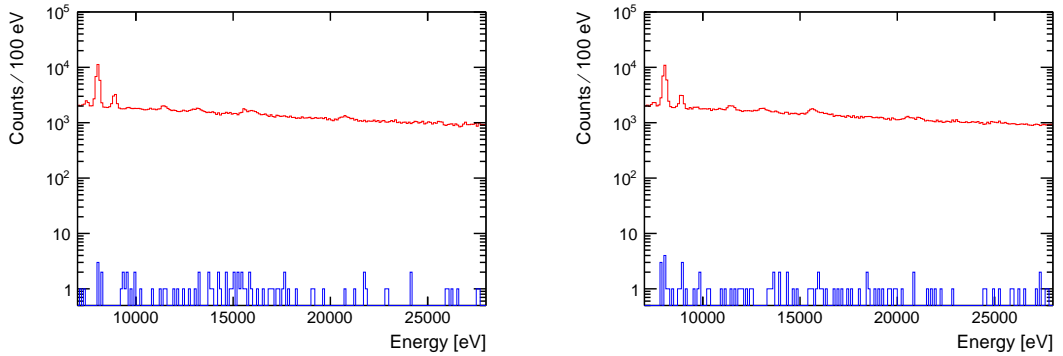

Figure 6.13.: The spectrum without current (left) and with current (right) in red taken at LNGS with the respective counts rejected by scintillator veto in blue.

rejection ratio for the counts above 7 keV is 0.02 % for the data with and without current. The two datasets were separated for this analysis in order to check for noise effects that might be introduced by the 100 A current. These effects were

not observed. Comparing this outcome to simulations, a rejection rate of 0.02 % points to a minimum energy deposition of 200 keV in inner and outer scintillator layer to produce a veto signal. This value of 200 keV is double the value of 100 keV estimated for this threshold in chapter 5. This value is an estimation rather than a calculation, so 200 keV can be accepted as the threshold value, despite this discrepancy. The trigger logic of inner AND outer scintillator layer instead of triggering on any scintillator signal was kept in order to avoid triggers from SiPM dark counts. As the trigger condition was an AND of the two layers, both layers would need to have a dark count in order to produce a dark count trigger. As these correlated dark counts are much more unlikely than single dark counts, they can be suppressed in this way. Despite the low rejection rate of the active veto, it was kept in the setup for two reasons, which were already discussed in section 4.3. Firstly, the scintillators provide a passive shielding of the SDDs from γ radiation. Secondly, once the passive shielding will be installed around the setup (see chapter 8), the γ background will possibly be reduced to a level were the background from cosmic radiation, which can be rejected by the active veto, becomes relevant.

The rate of high energy charged particles impinging on the setup can be estimated from the spectra of scintillator signals recorded by the QDC. Events with high energy deposited in one scintillator can be attributed to these particles, as their energy deposition is typically higher than the one from γ radiation. This is difficult for two reasons: Firstly, the count rate of high energy charged particles is very low, in the order of a few counts per week per scintillator. Secondly, the separation between events caused by γ radiation and charged particles is not unambiguous. Nevertheless a rate of 1 event per scintillator every 3 days can be estimated from the data. This is in good agreement with the rate given in [44] of 3.41×10^{-4} m^{-2} s^{-1}.

6.6. Effects of 100 A Current

The 100 A current flowing through the Cu conductor affects the measurements in several ways. One effect is that the heat produced by the current in turn heats the SDDs, which are mounted approximately 0.5 cm away from the Cu strips. The temperature of the Cu strips is stabilized by a water cooling system and the temperature of the SDDs is kept constant by argon cooling (see also chapter 3). These cooling systems counteract any temperature change of the detectors. The measured SDD temperatures are shown in figure 6.14. The x-axis of this and similar plots spans a time from February 2016 until July 2017, as was already mentioned. Each data point corresponds to the average over one day of data
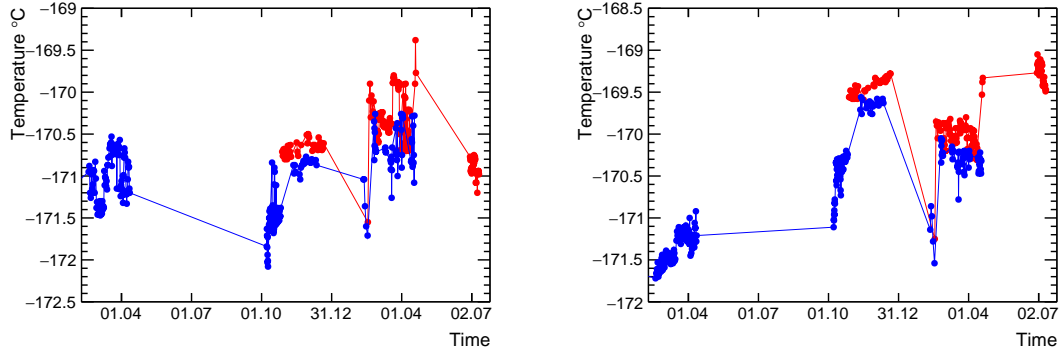
Figure 6.14.: Temperature measured on the aluminum frame of SDDs 1-3 (left) and on the aluminum frame of SDDs 4-6 (right). Data points with 100 A current are shown in red and data points without current are shown in blue. Each data point corresponds to the average over one day of data.

taking time. From the figures it can be seen that the 100 A current only raises the temperature of the metal frame of the SDDs by approximately 0.2 - 0.4 °C compared to the measurements without current. The temperature of the detectors themselves (and not their frames) might be affected more than shown in the plots, but as there is no possibility to measure it directly it is impossible to be certain. Nevertheless it shows that the SDD environment can be stabilized at cryogenic temperature even with high currents. It is worth mentioning that the problems with suddenly rising temperature of the SDDs (see also chapter 5) were overcome during the measurements at LNGS by filling more argon gas into the system.

Another interesting effect of the 100 A current is that it influences the energy resolution of the silicon detectors. A plot of the energy resolution of one SDD at 6 keV for different times of measurement with and without current is shown in figure 6.15. The resolution gets worse in times when the current is turned on by approximately 20 eV (FWHM). This effect might be caused by the temperature rise in the SDDs mentioned above. The dependence of energy resolution on temperature was for example reported in [36]. The change in temperature of the detectors would have to be higher than the 0.4 °C measured on their metal holder. The same effect of peak broadening due to a current was also reported in [21], where it was attributed to electronic noise introduced by the current. The energy resolution at 6 keV measured at LNGS with and without current for the complete data taking time are shown in table 6.4 for each single SDD and for the spectrum resulting from the summation of all single SDDs. The energy resolution
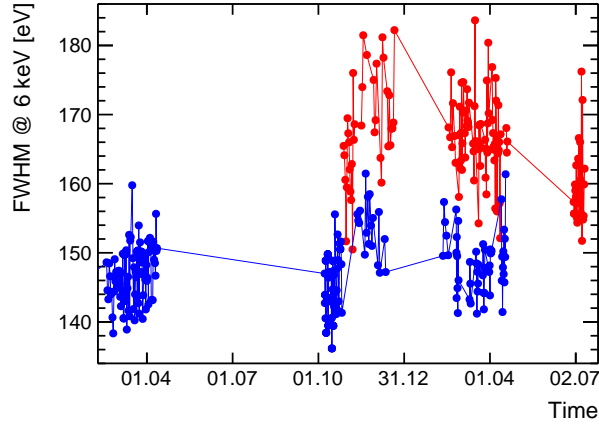
Figure 6.15.: Energy resolution (FWHM) at 6 keV for SDD 1 without current (blue) and with current (red). The statistical uncertainty for the amount of data in each measurement is approximately 0.5 eV. Each data point corresponds to one day of data.

current	SDD 1	SDD 2	SDD 3	SDD 4	SDD 5	SDD 6	Sum
0 A	159 eV	151 eV	151 eV	149 eV	157 eV	163 eV	155 eV
100 A	177 eV	165 eV	166 eV	155 eV	160 eV	169 eV	165 eV

Table 6.4.: Energy resolution (FWHM) of the single SDDs and their sum at 6 keV. Typical statistical uncertainty for the amount of data going into this calculation is 0.5 eV.

changes by approximately 10 eV at 6 keV when turning on the current for the summed up spectrum. The same effect also occurs at an energy of 8 keV where the Pauli-forbidden transition is expected.

6.7. Spectral Lines in the Energy Spectrum

The low background at LNGS gives the opportunity to study possible spectral lines from elements occurring in the equipment surrounding the detectors. Conclusions from this analysis might be used to improve future MC simulations of the setup. The complete energy spectrum taken at LNGS corresponding to approximately 198 days of data is shown in figures 6.16 and 6.17.
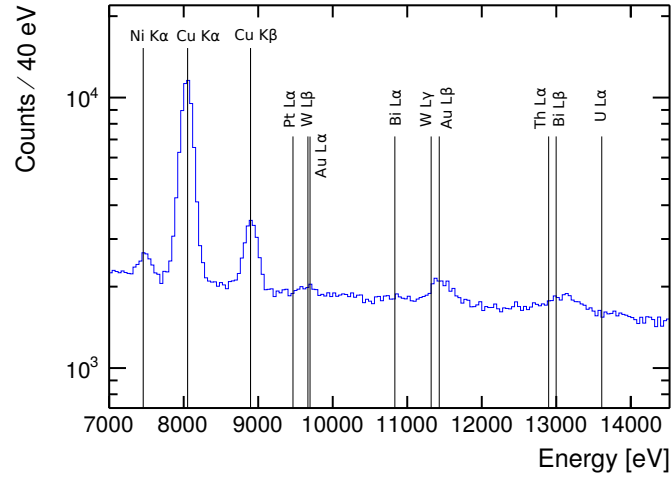
Figure 6.16.: Energy spectrum corresponding to 198 days of data taken at LNGS with candidates for spectral lines.

The most prominent peaks are the Cu Kα and Cu Kβ peaks. The corresponding photons originate from the Cu conductor next to the SDDs. Another peak of certain origin is the Ni Kα peak at 7.5 keV. Nickel is for example used in stainless steel, from which the tubes of the water and argon cooling systems are made of. The Zirconium spectral lines come from a 15 μm thick Zirconium foil mounted above the SDDs, which was initially mounted for calibration with an X-ray tube, which was not performed. The anode of this tube is made out of tungsten (W), from which the tungsten L-lines might be coming from. Several other lines are drawn in the figure, which were suggested in [6]. As the two sources of calibration are Ti Kα and Mn Kα at 4.5 keV and 5.9 keV respectively, the energy calibration has a higher uncertainty for higher energies further away from these lines. This effect limits the possibility to accurately determine the spectral lines with higher energy.
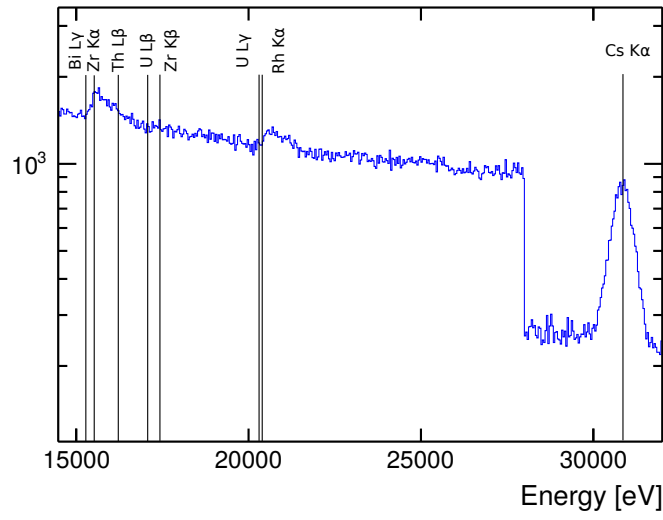
Figure 6.17.: Energy spectrum corresponding to 198 days of data taken at LNGS with candidates for spectral lines. The drop at 28 keV is non-physical as above this energy only the two SDDs, which are not in overflow above this energy, are shown.

7. Data Analysis

The data acquired with the procedures described in chapter 6 were analyzed using several methods. These methods have in common, that they investigate the difference of the spectra taken with and without current in the energy region in which the PEP violating transition is expected. These final spectra in the energy region of the PEP-violating transition with and without current are shown together with fit and residuals in figures 7.1 and 7.2. The Cu and Ni lines were fit like it was described in section 6.2 for the calibration lines, which means taking into account not only the Gaussian main peak, but also various other aspects of a spectrum in a real detector. The energy of the events in the histograms shown in this chapter were determined using techniques discussed in sections 6.1 - 6.4.

To better compare the data with and without current, a dataset of the data without current (total 116 days 20 hours) was selected with the same data taking time as the dataset with 100 A current (81 days 10 hours). In order to have the maximum temporal overlap between the two datasets with and without current, the later part of the data without current was chosen. The data without current analyzed in this chapter spans a time from end of March 2016 (compared to beginning of February for the full dataset) until April 2017. Systematic errors of the analysis methods mentioned in this chapter will be discussed in A.

7.1. Spectral Subtraction Analysis

One approach to calculate the upper limit for the probability of the violation of the PEP from two energy spectra recorded with and without current was described by E. Ramberg and G. A. Snow in [2]. The basic principle is to look for an excess of events in the energy region of the Pauli-forbidden transition in the spectrum taken with current compared to the spectrum without current (see also chapter 2.4). If the PEP can be violated, photons from this transition are expected to occur and introduce this difference between the two spectra. From the difference or the lack thereof, and experimental parameters, the probability for the violation of the PEP
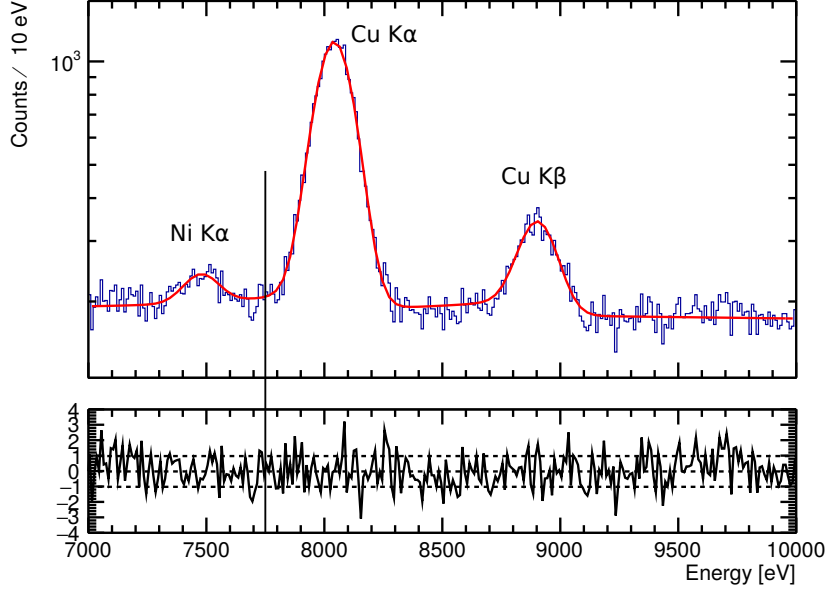
Figure 7.1.: Data taken with 100 A current together with fit. In the lower pad the fit residuals divided by the square root of the fit function are shown. The position of the PEP violating transition is marked in black.

or an upper limit for it can be calculated. This analysis was presented for a subset of the data in [52].

Using the same notation as in the publications about the VIP2 experiment, the number of possible detected events from PEP-violating transitions ΔN_x is related to the probability that the PEP is violated in an atom $\frac{\beta^2}{2}$ (see also chapter 2.2) as shown in equation 7.1.

$$\Delta N_x \geq \frac{\beta^2}{2} N_{new} \frac{N_{int}}{10} (\text{detection efficiency}), \tag{7.1}$$

where N_{new} is the number of new electrons introduced by the current. It can be calculated from the magnitude of the current I, the data taking time Δt and the electronic charge e as

$$N_{new} = \frac{1}{e} \sum (I \Delta t). \tag{7.2}$$

Furthermore, N_{int} is the number of scattering reactions a single electron undergoes during the passage of the Cu target. It is of the order of $\frac{D}{\mu}$, where D is the length of the target and μ is the mean free path length of electrons in Cu. The probability for absorption of the electron into the 2p state in the case of a scattering is assumed
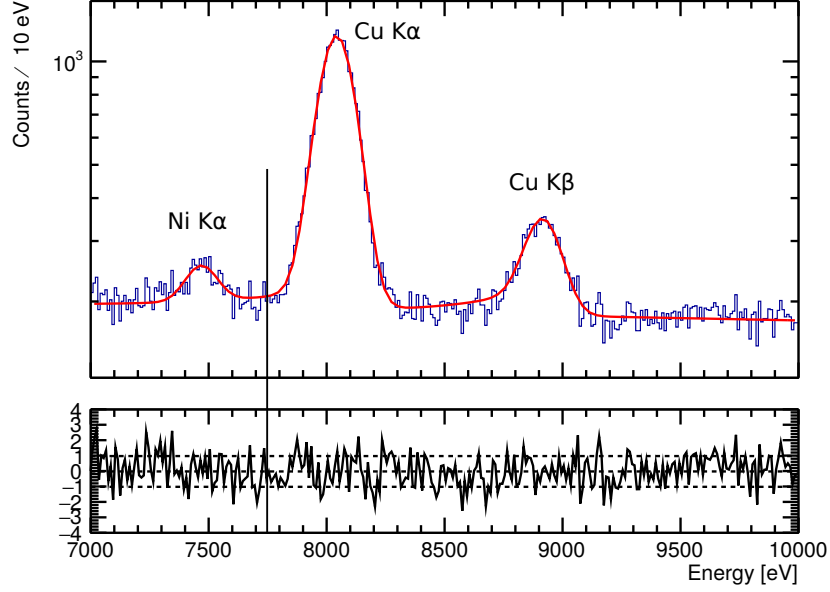
Figure 7.2.: Data taken without current together with fit. In the lower pad the
fit residuals divided by the square root of the fit function are shown.
The position of the PEP violating transition is marked in black.

to be larger than 10 % [2], which introduces the factor $\frac{1}{10}$ and the greater or equal
sign in the equation. The detection efficiency is the probability for a 7.7 keV
photon produced in the target to be detected. This probability includes photon
absorption in the target and the finite solid angle covered by the SDDs (see section
4.1). The equation can then be rewritten as

$$\Delta N_x \geq \frac{\beta^2}{2} \frac{1}{10} \frac{D \sum (I \Delta t)}{\mu e} (\text{detection efficiency}) \tag{7.3}$$

or

$$\frac{\beta^2}{2} \leq \frac{10 \mu e}{D \sum (I \Delta t)} \frac{\Delta N_x}{(\text{detection efficiency})}. \tag{7.4}$$

The values for these parameters used in the analysis are summed up in table 7.1.
Inserting these values into equation 7.4, the relation between amount of counts

μ	D	I	Δt	detection efficiency
3.91×10^{-6} cm[21]	7.1 cm	100 A	81 days 10 hours	1.82 %

Table 7.1.: Values for the experimental parameters for the analysis of the VIP2
data.

from non-Paulian transitions and the probability for the violation of the PEP can be obtained:

$$\frac{\beta^2}{2} \leq \frac{\Delta N_x}{1.46 \times 10^{31}}.$$ (7.5)

The number of detected counts ΔN_x needs to be determined from the energy spectra with and without current. A dataset from the data without current was selected with the same data taking time as the data with current (81 days 10 hours), as was mentioned earlier. ΔN_x was calculated as the difference in counts in the region of interest (ROI) around the non-Paulian Cu Kα transition. As the center of this region the energy of the forbidden Cu Kα_1 transition of 7747 eV (see chapter 2.4) is usually taken. As its width the FWHM of the Cu Kα line of the spectrum with current is assumed. The energy resolutions at 8 keV for the spectra of the sum of all six SDDs with and without current were determined by fitting the Cu lines in the same way as it was done for the calibration lines of Ti and Mn (see chapter 6.2). The fits of the spectra, from which the energy resolutions were determined, are shown in figure 7.1 and 7.2. The results are shown in equations 7.6 and 7.7.

$$\text{FWHM (8 keV)} = 187.7 \pm 1.87 \text{ eV} \qquad \text{with current} \qquad (7.6)$$

$$\text{FWHM (8 keV)} = 176.9 \pm 1.79 \text{ eV} \qquad \text{without current} \qquad (7.7)$$

To account for a theoretical uncertainty of 10 eV of the energy of the PEP-violating transition given in [53], the width of the ROI was chosen as 200 eV instead of 187.7 eV. It spans the energy range from 7647 eV - 7847 eV. The energy region around the Pauli-forbidden transition of the two spectra consisting of the sum of all six SDDs for the spectra with and without current are shown in figure 7.3. On the right side of the figure the spectrum without current was subtracted from the spectrum with current. No significant peak structure can be made out in this figure around the 7747 eV of the forbidden transition. From these spectra ΔN_x can be calculated as the difference between the counts in the ROI in the spectrum with current and the spectrum without current:

- with I = 100 A: $N_X = 4202 \pm 65$

- with I = 0 A: $N_X = 4105 \pm 64$

- for the subtracted spectrum: $\Delta N_X = 97 \pm \sqrt{65^2 + 64^2} = 97 \pm 91$

The statistical error on the counts in the ROI in the spectra with and without current are calculated as $\sqrt{N}$ when N are the counts, as the number of events are distributed according to a Poisson distribution with mean N. The statistical error
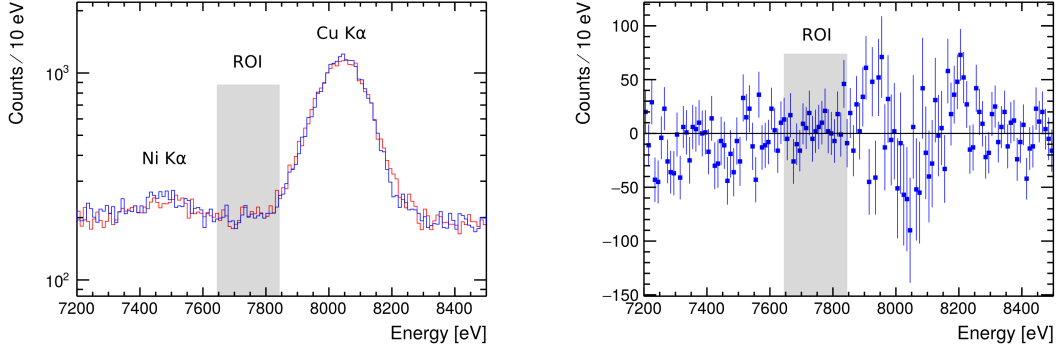
Figure 7.3.: Spectrum with current (red) and without current (blue) around the region of interest (gray) on the left. The subtracted spectrum is shown on the right with error bars.

of ΔN_X is the square root of the sum of variances of N_X. As the deviation of ΔN_X from zero is only about 1σ, it is not enough to claim a discovery. Nevertheless, an upper limit on the probability for a violation of the PEP can be set using 3σ as the upper limit of ΔN_X resulting in a 99.73 % C.L.:

$$\frac{\beta^2}{2} \leq \frac{3 \times 91}{1.46 \times 10^{31}} = 1.87 \times 10^{-29}. \tag{7.8}$$

This value is an improvement by a factor of 2.5 compared to the results of the VIP experiment of 4.7×10^{-29} given in [4].

7.2. Simultaneous Fit Analysis

Another approach for determining the upper limit on the probability for the violation of the PEP is the simultaneous fit of the signal (with current) and the background (without current) spectrum. This method was applied in the analysis of kaonic atom precision spectroscopy data in [54]. A global χ^2 function was defined for the fits of the two histograms of the energy spectra which was minimized for both spectra at the same time. A Gaussian distribution was added to the fit function of the signal histogram at 7747 eV, which represents the contribution from non-Paulian transitions. Its position was fixed, its width was the same as the one of the Cu Kα line of the signal histogram and its gain was a free parameter.

For the background function, a 1st order polynomial was chosen. The two param-

eters for this function were free and common for the fits of both histograms. The position of the Cu Kα, Cu Kβ and Ni Kα lines were kept fixed to their physical values. All other parameters like the widths and the gain of these lines were free parameters and independent for both histograms. With this method, the estimated number of candidate events and its error can directly be obtained from the parameters of the Gaussian function representing signal events in the converged minimum χ^2 fit. In this case the MINUIT package of the CERN ROOT software framework with MINOS error estimation was used. Special care was taken that the crucial error assessment was not perturbed by boundaries of fit parameter ranges. The program code is shown in the appendix D. The results of this fit are shown in figure 7.4. The fit corresponds to a reduced χ^2 of 1.27. As the Gaussian
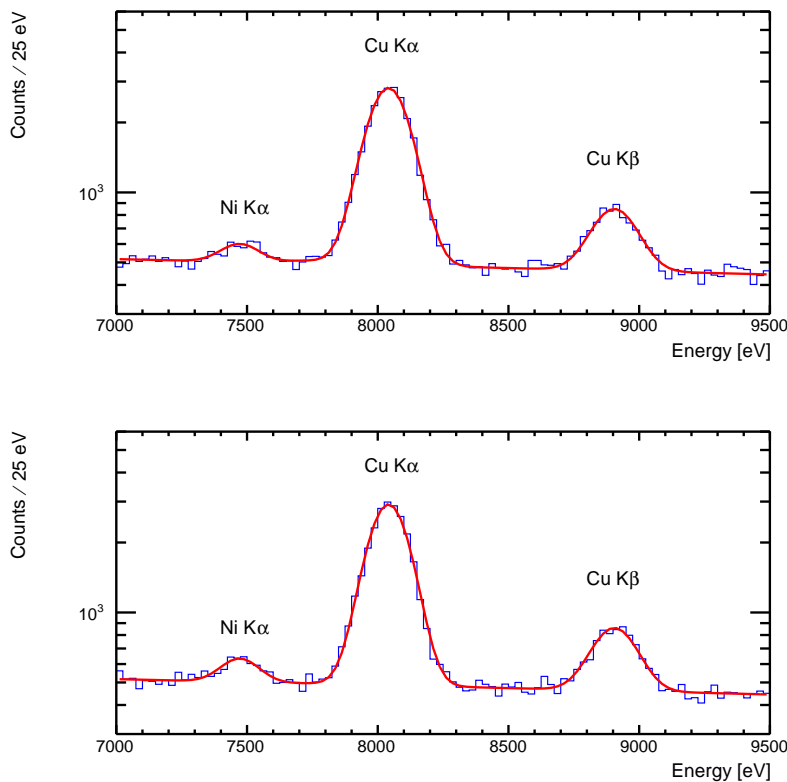

Figure 7.4.: The fits obtained by a simultaneous fit of the signal histogram with current (above) and the background histogram (below) with a few common parameters.

function corresponding to photons from possible non-Paulian transitions is small and impossible to see in this figure, it is drawn again in figure 7.5 together with a 1σ confidence interval.
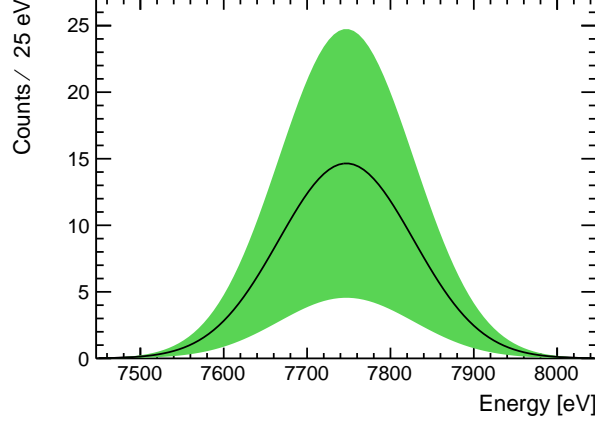
Figure 7.5.: Gaussian function corresponding to possible non-Paulian transitions (black) with 1σ confidence interval (green), obtained from a simultaneous fit of the two spectra.

This method has a few advantages compared to the subtraction method described in section 7.1. On the one hand the definition of a region of interest is not necessary. In the simultaneous fit function this is not needed, as the fit makes use of a wide energy range for the determination of the parameters of the global fit function, from which the number of candidate PEP-violating events is calculated. On the other hand the error of the gain of the Gaussian representing the forbidden transition takes into account uncertainties of the other fit parameters. These uncertainties are usually not evaluated using the subtraction method.

The fit result for the number of detected photons from PEP-violating transitions was 119 ± 82. This is more than 1σ away from zero but not enough to claim a discovery. This is why more data is needed to prove or disprove this excess. Nevertheless, the error of the gain of the Gaussian can, in analogy to the subtraction method, be used to set a 3σ upper limit at 99.73 % C.L. of detected photons from PEP-violating transitions of 3×82. With formula 7.5 the upper limit for the violation of the PEP can be calculated:

$$\frac{\beta^2}{2} \leq \frac{3 \times 82}{1.46 \times 10^{31}} = 1.69 \times 10^{-29}. \tag{7.9}$$

7.3. Bayesian Count Based Analysis

This section represents the preliminary status of a data analysis using the Bayes theorem. The Bayes theorem links the estimate of a parameter (*a-priori distribution, f_0*) with the probability to find the measured data given a certain value for this parameter (*likelihood function, L*) to calculate the probability distribution for this parameter given the measured data (*a-posteriori distribution, f*). For a measured quantity X and a parameter λ that shall be estimated from these data it can be written as

$$f(\lambda|X) = \frac{L(X|\lambda)f_0(\lambda)}{\int L(X|\lambda)f_0(\lambda)d\lambda}. \tag{7.10}$$

For a detailed discussion of the uses of this theorem in particle physics see for example [47].

The model described in this section was discussed in more detail in [55]. In the case of the VIP2 data the measured data can be interpreted as the number of counts X in a certain energy region. X can be seen as drawn from a Poisson distribution characterized by the unknown parameter λ:

$$L(X|\lambda) = \frac{\lambda^X e^{-\lambda}}{X!}. \tag{7.11}$$

This is the likelihood function of the number of counts X given a parameter λ. The width of the energy region is arbitrary, as any two energy regions can be combined and the sum of their counts will again be distributed according to a Poisson distribution. As prior for λ a flat uniform distribution larger than zero was chosen. This encodes the fact, that there can not be a negative amount of events from PEP-violating transitions. The posterior for λ can be written with the Bayes theorem as

$$f(\lambda|X) = \frac{\frac{\lambda^X e^{-\lambda}}{X!}f_0(\lambda)}{\int_0^\infty \frac{\lambda^X e^{-\lambda}}{X!}f_0(\lambda)d\lambda}. \tag{7.12}$$

The integral over a Poisson distribution is one, so the normalization integral equals one and the posterior for λ is

$$f(\lambda|X) = \frac{\lambda^X e^{-\lambda}}{X!}. \tag{7.13}$$

This is a Γ distribution [1] of the parameter λ characterized by the parameters a

---

[1]The Γ distribution depends on parameters $a \geq 0$ and $b \geq 0$, and has the PDF $f(x) = \frac{x^{a-1} \times \exp\frac{-x}{b}}{b^a \times \Gamma(a)}$ for $x \geq 0$, with $\Gamma(y) = (y-1) \times \Gamma(y-1), y \geq 0$

(*shape parameter*) $= X + 1$ and b (*scale parameter*) $= 1$. The mean of λ is equal to $ab = X + 1$, the variance is $ab^2 = X + 1$ and the mode is $(a - 1)b = X$.

In the case of data without current and therefore with no signal, the only contribution to the number of events in the region of interest are background events, which we now call X_{bg} with a distribution parameter λ_{bg}. For the histogram with current there are two contributions to the number of events in the ROI X_s, namely from background events and from signal events from the PEP-violating transition X_{sg}. The number of counts from background events in the signal histogram is seen as drawn from a Poisson distribution with the same parameter as the one from the histogram without current λ_{bg}, and the amount of signal counts is drawn from a distribution parametrized by λ_{sg}. The likelihood function for the signal histogram is then

$$L(X_s | \lambda_{sg}, \lambda_{bg}) = \frac{(\lambda_{sg} + \lambda_{bg})^{X_s} e^{-(\lambda_{sg} + \lambda_{bg})}}{X_s!}. \tag{7.14}$$

Applying Bayes' theorem with a constant positive prior for λ_{sg}, the distribution of this parameter as a function of X_s and λ_{bg} can be obtained:

$$f(\lambda_{sg} | X_s, \lambda_{bg}) = \frac{(\lambda_{sg} + \lambda_{bg})^{X_s} e^{-\lambda_{sg}}}{\int_0^\infty (\lambda_{sg} + \lambda_{bg})^{X_s} e^{-\lambda_{sg}} d\lambda_{sg}}. \tag{7.15}$$

The normalization integral does not reduce to one, as the integration variable is λ_{sg} and not $(\lambda_{bg} + \lambda_{sg})$. The integral in equation 7.15 equals $e^{\lambda_{bg}} \Gamma(1 + X_s, \lambda_{bg})$. The distribution of λ_{sg} was calculated numerically by sampling λ_{bg} according to its distribution obtained from X_{bg}, which is a Γ distribution with $a = X_{bg} + 1$ and $b = 1$ (see equation 7.13). The Mathematica software framework was used [56]. The code is listed in E. Counts in the ROI with current X_s were equal to 4202 and counts in the ROI without current X_{bg} were equal to 4105 (see also chapter 7.1).

The preliminary confidence interval corresponding to a 99.73 % C.L. spans $0 < \lambda_{sg} < 349$. With equation 7.5, the preliminary upper limit on the probability for a violation of the PEP can be calculated:

$$\frac{\beta^2}{2} \leq \frac{349}{1.46 \times 10^{31}} = 2.4 \times 10^{-29}. \tag{7.16}$$

The posterior probability density (P.P.D.) and the cumulative distribution function (C.D.F.) of the posterior probability of the parameter λ_{sg} are shown in figure 7.6. From the plot of the C.D.F. the upper limit for λ_{sg} at 99.73 % confidence level of about 349 can be verified.
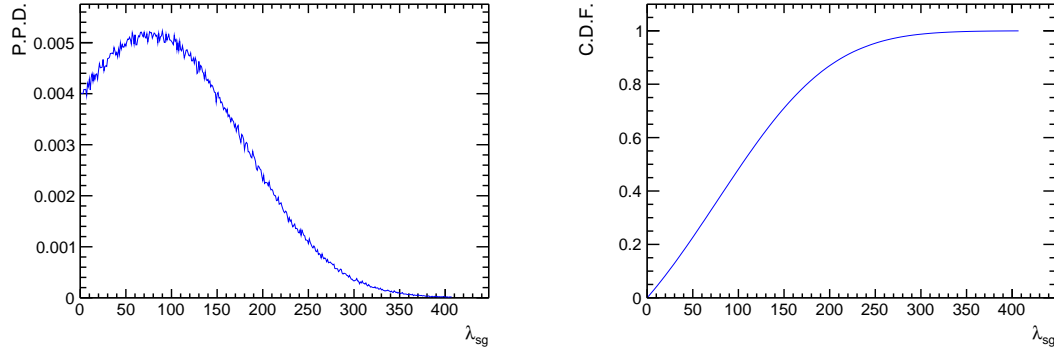
Figure 7.6.: The preliminary probability density (left) and cumulative distribution function (right) of λ_{sg} for a flat positive prior.

7.4. Bayesian Fit Based Analysis

This section represents the preliminary status of a data analysis method using the Bayes theorem. The RooFit [57] and RooStats [58] frameworks were used to calculate an estimation for the number of events from PEP-violating transitions using not only the number of counts in the ROI, but the information from the complete histogram. In a first step the histogram without current was fit. The background level was extracted as a first order polynomial including its errors. Then the histogram with current was fit with the parameters for the background taken from the fit of the histogram without current and kept constant. The fit of the histogram with current included a Gaussian function with a fixed mean of 7747 eV and the same width as the main Cu Kα peak. The outcome of this fit was used as an input for a RooStats::BayesianCalculator. The number of signal events at 7747 eV was the parameter of interest. The RooStats::BayesianCalculator calculates a posterior probability density of the parameter of interest, taking into account an a-priori distribution, which is adjustable by the user. A uniform distribution for values larger than zero was used as this a-priori distribution. The two parameters of the first order polynomial of the background were treated as the nuisance parameters (see for example [47]) and were marginalized using a MC integration method. Parts of the code are shown in E. The posterior density for the amount of signal events is shown in figure 7.7. The preliminary upper limit of the parameter of interest corresponding to a 99.73 % confidence level is at 379 signal events. With formula 7.5, the preliminary upper limit for the probability

for a violation of the PEP can be calculated:

$$\frac{\beta^2}{2} \leq \frac{379}{1.46 \times 10^{31}} = 2.61 \times 10^{-29}. \tag{7.17}$$
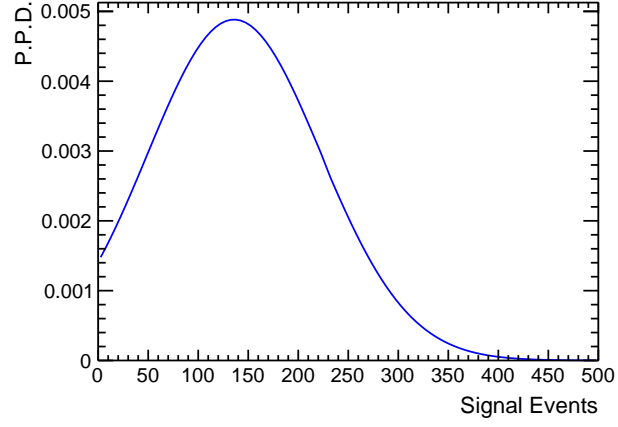

Figure 7.7.: The preliminary posterior probability density for the number of events from PEP-violating transitions for a flat positive prior.

8. Summary and Outlook

The goal of this work was to conduct the most stringent test of Spin-Statistics and specifically of the Pauli Exclusion Principle for electrons in an experiment circumventing the Messiah-Greenberg superselection rule. For this purpose the VIP2 (Violation of the Pauli Principle) experimental setup was built and tested at Stefan Meyer Institute and was later brought to the underground laboratory LNGS in Italy for data taking. The predecessor experiment VIP set an upper limit for the probability for the violation of the PEP of 4.7×10^{-29} [4]. A violation of the PEP can be detected in the VIP2 experiment by searching for photons from a Cu conductor, which are coming from Pauli-forbidden 2p to 1s transitions. As these transitions are only expected when a current runs through it, 100 A are circulated through the conductor. These transitions have a slightly lower transitions energy than normal transitions, because there are two electrons in the ground state already before the transition happens. The second electron increases the shielding of the potential of the nucleus and thereby reduces the Kα transition energy by around 300 eV. The limit on the PEP is calculated from an excess of photons in this energy region in the histogram recorded with a current, compared to the histogram without current.

The core part of the setup are Silicon Drift Detectors recording the photon spectrum from the Cu conductor. An active shielding system consisting of plastic scintillators read out by Silicon Photomultipliers was installed around these detectors to veto events caused by external ionizing radiation. These systems were exhaustively tested first at LNF in Italy and at SMI together with the cooling system of the SDDs and the slow control and data acquisition systems. The results are summed up in table 8.1. The argon cooling kept the temperature of the SDDs at approximately 100 K. The functionality of the slow control and the data acquisition systems was verified. A current through the Cu conductor of up to 180 A was tested and a stable target temperature of about 20 °C was verified under these conditions. The data taken at SMI and LNGS corresponds to the results predicted by Geant4 simulations in several aspects:

- The simulated SDD hit rate of cosmic radiation corresponds to the measured

Active Shielding				SDDs	
Detection Efficiency			Time Resolution	Energy Resolution	Time Resolution
500 MeV e^-	Cosmic Radiation	γ Radiation	FWHM	FWHM @ 6 keV	FWHM
98 %	> 90 %	< 1 %	2.2 ns	150 eV	380 ns

Table 8.1.: Results of the test measurements at LNF and at SMI for the active shielding and the SDDs.

rate of events rejected by scintillator veto at SMI. This indicates that the detection of cosmic radiation with the active shielding works well.

- The scintillator hit rate of cosmic radiation estimated from simulations corresponds to the measured rate of events with high QDC values at LNGS.

- The constant part of the background spectrum measured at LNGS is equivalent to the one obtained by simulations with the high energy photon spectrum of LNGS as input.

The final analyzed data corresponds to 81 days and 10 hours with a 100 A current and the same amount of data without current for all six SDDs. The upper limit for the probability for a violation of the PEP was calculated from the difference in the energy region of the PEP-forbidden transition at 7747 eV of these two spectra. Several techniques were used to calculate the 99.73 % C.L. upper limit, which give slightly different values:

1. Difference of counts in the region of interest of the two histograms. The upper limit is calculated from the statistical error of this difference, assuming a Poisson distribution for the number of counts in each energy bin.

2. Simultaneous fit of the two spectra, with an additional signal Gaussian function in the histogram with current. The upper limit is calculated from the statistical error of the gain of this Gaussian.

3. Difference of counts in the region of interest of the two histograms using Bayesian statistics. The upper limit is calculated from the posterior distribution, which uses a flat positive prior distribution and a Poisson distribution as likelihood function.

4. A fit of the histogram with current including a Gaussian function at the en-

ergy of the PEP-forbidden transition is done, using the background function obtained from the histogram without current. From the result of this fit and the data a posterior distribution for the amount of signal counts is calculated using a flat positive prior.

The results of these different methods are summed up in table 8.2. For comparison

	1. Spectrum Subtraction	2. Simultaneous Fit	3. Bayesian Subtraction	4. Bayesian Fit
Upper Limit $\frac{\beta^2}{2}$	1.87×10^{-29}	1.69×10^{-29}	2.4×10^{-29}	2.61×10^{-29}

Table 8.2.: Results for the upper limit for the violation of the PEP using different analysis techniques. The results coming from Bayesian statistics (methods 3 + 4) are preliminary.

with other publications about this and related experiments, the limit from the spectrum subtraction of

$$\frac{\beta^2}{2} \leq 1.87 \times 10^{-29} \tag{8.1}$$

can be used. This result represents an improvement on the limit set by the VIP experiment by a factor of 2.5.

The VIP2 setup is currently (February 2018) at the Stefan Meyer Institute for testing and mounting new SDDs with a larger active area (20.5 cm^2). After the work at SMI is finished, the setup will be transported to LNGS, where further data will be taken with an additional passive shielding consisting of Pb and Cu blocks of 5 cm thickness. After around three more years of data taking, the anticipated new upper limit for the probability of the violation of the Pauli Exclusion Principle will be on the order of 10^{-30}- 10^{-31}. Or else, a violation of the Pauli Exclusion Principle will be discovered.

Bibliography

[1] M. Goldhaber and G. Scharff-Goldhaber. Identification of Beta-Rays with Atomic Electrons. *Physical Review*, 73(12):1472–1473, jun 1948.

[2] E. Ramberg and G. A. Snow. Experimental limit on a small violation of the Pauli principle. *Physics Letters B*, 238(2):438–441, 1990.

[3] C. Curceanu, S. Bartalucci, A. Bassi, et al. Experimental tests of Quantum Mechanics: from Pauli Exclusion Principle Violation to spontaneous collapse models. *Journal of Physics: Conference Series*, 361:012006, 2012.

[4] C. Curceanu, S. Bartalucci, S. Bertolucci, et al. Experimental tests of quantum mechanics: Pauli Exclusion Principle Violation (the VIP experiment) and future perspectives. *Journal of Physics: Conference Series*, 306(1):012036, 2011.

[5] W. Pauli. Nobel Prize lecture: Exclusion principle and quantum mechanics, 1946.

[6] L. Sperandio. *New experimental limit on the Pauli Exclusion Principle violation by electrons from the VIP experiment*. PhD thesis, 2008.

[7] A. M. L. Messiah and O. W. Greenberg. Symmetrization Postulate and Its Experimental Foundation. *Physical Review*, 136(1B):B248—-B267, 1964.

[8] I. G. Kaplan. The Pauli Exclusion Principle. Can It Be Proved? *Foundations of Physics*, 43(10):1233–1251, 2013.

[9] W. Pauli. The Connection Between Spin and Statistics. *Phys. Rev.*, 58(8):716–722, 1940.

[10] J. Schwinger. Spin, Statistics and the TCP Theorem. *Proceedings of the National Academy of Sciences of the United States of America*, 44(2):223–228, 1958.

[11] G. Luders and B. Zumino. Connection between Spin and Statistics. *Physical Review*, 110(6):1450–1453, 1958.

[12] A. Stern. Anyons and the quantum Hall effect— A pedagogical review. *Annals of Physics*, 323:204–249, 2008.

[13] H. S. Green. A generalized method of field quantization. *Physical Review*, 90(2):270–273, 1953.

[14] O. W. Greenberg. Theories of violation of statistics. *AIP Conference Proceedings*, 545(1):113–127, 2000.

[15] A. Ignatiev and V. Kuzmin. IS SMALL VIOLATION OF THE PAULI PRINCIPLE POSSIBLE? *International Centre for theoretical physics (Preprint)*, 87(13), 1987.

[16] A. Govorkov. Can the Pauli principle be deduced with local quantum field theory? *Physics Letters A*, 137(1-2):7–10, may 1989.

[17] O. W. Greenberg. Particles with small violations of Fermi or Bose statistics. *Physical Review D*, 43(12):4111–4120, 1991.

[18] D. Colladay and A. Kostelecky. Lorentz-Violating Extension of the Standard Model. *Physical Review D*, 58(11), 1998.

[19] M. G. Jackson. Spin-Statistics Violations in Superstring Theory. *Physical Review D*, 78(12):126009, 2008.

[20] N. E. Mavromatos. Models and Searches of CPT Violation: a personal, very partial, list. *EPJ Web of Conferences*, 166, 2018.

[21] S. R. Elliott, B. H. LaRoque, V. M. Gehman, M. F. Kidd, and M. Chen. An Improved Limit on Pauli-Exclusion-Principle Forbidden Atomic Transitions. *Foundations of Physics*, 42(8):1015–1030, 2012.

[22] E. Corinaldesi. MODEL OF A DYNAMICAL THEORY OF THE PAULI PRINCIPLE. *Nuovo Cim.*, 43:937, 1967.

[23] A. Shimony. Proposed Experiment to Test the Possible Time Dependence of the Onset of the Pauli Exclusion Principle. *Quantum Information Processing*, 5(4):277–286, aug 2006.

[24] F. Reines and H. W. Sobel. Test of the Pauli Exclusion Principle for Atomic

Electrons. *Physical Review Letters*, 32(17):954–954, apr 1974.

[25] R. Bernabei, P. Belli, F. Cappella, et al. New search for processes violating the Pauli exclusion principle in sodium and in iodine. *The European Physical Journal C*, 62(2):327–332, jul 2009.

[26] G. Bellini, S. Bonetti, M. Buizza Avanzini, et al. New experimental limits on the Pauli-forbidden transitions in C12 nuclei obtained with 485 days Borexino data. *Physical Review C - Nuclear Physics*, 81(3):034317, 2010.

[27] V. Novikov. Test of the pauli exclusion principle for atomic electrons. *Physics Letters B*, 240, 1990.

[28] D. Javorsek, M. Bourgeois, D. Elmore, et al. New experimental test of the pauli exclusion principle using accelerator mass spectrometry. *Physical review letters*, 85(13):2701–4, 2000.

[29] G. Hilscher. *Festkörperphysik 1*. 2009.

[30] S. D. Matteo and L. Sperandio. VIP Technical Note IR - 4. Technical report, 2005.

[31] J. V. Mallow, J. P. Desclaux, and A. J. Freeman. Dirac-Fock method for muonic atoms: Transition energies, wave functions, and charge densities. *Physical Review A*, 17(6):1804–1809, 1978.

[32] J. Desclaux. http://dirac.spectro.jussieu.fr/mcdf/, 2005.

[33] C. Curceanu. EVALUATION OF THE X-RAY TRANSITION ENERGIES FOR THE PAULI-PRINCIPLE-VIOLATING ATOMIC TRANSITIONS IN SEVERAL ELEMENTS BY USING THE DIRAC-FOCK METHOD. Technical report, 2013.

[34] E. Gatti and P. Rehak. Semiconductor drift chamber - An application of a novel charge transport scheme. *Nuclear Instruments and Methods In Physics Research*, 225(3):608–614, sep 1984.

[35] P. Lechner and H. Soltau. Silicon Drift Detectors for SIDDHARTA - Mounting, Bonding and Testing. Technical report.

[36] M. Cargnelli, M. Bragadireanu, M. Catitti, et al. Silicon drift detectors for hadronic atom research - SIDDHARTA. *Proceedings, International Conference on Exotic Atoms and Related Topics (EXA 2005)*, pages 1–8, 2005.

[37] W. Leo. *Techniques for Nuclear and Particle Physics Experiments.* 2 edition, 1993.

[38] Eljen Technology. http://www.eljentechnology.com/.

[39] AdvanSiD. AdvanSiD ASD-SiPM3S-P. Technical report, 2012.

[40] A. T. De Waele. Pulse-tube refrigerators: principle, recent developments, and prospects. *Physica B: Condensed Matter*, 280(1-4):479–482, 2000.

[41] S. Agostinelli, J. Allison, K. Amako, et al. GEANT4 - A simulation toolkit. *Nuclear Instruments and Methods in Physics Research, Section A: Accelerators, Spectrometers, Detectors and Associated Equipment*, 506(3):250–303, 2003.

[42] T. K. Gaisser and T. Stanev. Cosmic Rays. *The European Physical Journal C*, 15(1-4):150–156, 2000.

[43] M. Ambrosio, R. Antolini, A. Baldini, et al. Measurement of the residual energy of muons in the Gran Sasso underground laboratories. *Astroparticle Physics*, 19(3):313–328, 2003.

[44] G. Bellini, J. Benziger, D. Bick, et al. Cosmic-muon flux and annual modulation in Borexino at 3800 m water-equivalent depth. *Journal of Cosmology and Astroparticle Physics*, 08:049, 2013.

[45] M. Haffke, L. Baudis, T. Bruch, et al. Background measurements in the Gran Sasso Underground Laboratory. *Nuclear Instruments and Methods in Physics Research, Section A: Accelerators, Spectrometers, Detectors and Associated Equipment*, 643(1):36–41, 2011.

[46] C. Bucci, S. Capelli, M. Carrettoni, et al. Background study and Monte Carlo simulations for large-mass bolometers. *European Physical Journal A*, 41(2):155–168, 2009.

[47] O. Behnke, K. Kröninger, and T. Schörner-Sadenius. *Data Analysis in High Energy Physics.*

[48] J. L. Campbell, L. McDonald, T. Hopman, and T. Papp. Simulations of Si(Li) x-ray detector response. *X-Ray Spectrometry*, 30(4):230–241, 2001.

[49] S. Okada. E570 analysis summary. Technical report, 2007.

[50] M. Krause and O. J. Natural Widths of Atomic K and L Levels, K-alpha X-Ray Lines and Several KLL Auger Lines. *Journal of Physical and Chemical Reference Data*, 8(2), 1979.

[51] R. Brun and F. Rademakers. ROOT - An object oriented data analysis framework. *Nuclear Instruments and Methods in Physics Research, Section A: Accelerators, Spectrometers, Detectors and Associated Equipment*, 389(1-2):81–86, 1997.

[52] C. Curceanu, H. Shi, S. Bartalucci, et al. Test of the Pauli Exclusion Principle in the VIP-2 Underground Experiment. *Entropy*, 19(7):300, 2017.

[53] S. Bartalucci, S. Bertolucci, M. Bragadireanu, et al. New experimental limit on the Pauli exclusion principle violation by electrons. *Physics Letters B*, 641(1):18–22, 2006.

[54] M. Bazzi, G. Beer, G. Bellotti, et al. K-series X-ray yield measurement of kaonic hydrogen atoms in a gaseous target. *Nuclear Physics A*, 954:7–16, oct 2016.

[55] K. Piscicchia, C. Curceanu, and E. Milotti. Bayesian model for the analysis of the VIP data. Technical report, 2010.

[56] Wolfram-Research. Mathematica 10.4, 2016.

[57] W. Verkerke and D. Kirkby. The RooFit toolkit for data modeling. 2003.

[58] L. Moneta, K. Belasco, K. Cranmer, et al. The RooStats Project. 2010.

[59] R. Barlow. Systematic Errors: facts and fictions. 2002.

[60] E. Milotti. Tests of the Pauli Exclusion Principle in bulk matter and their open problems: the case of the VIP experiment. Technical report, 2017.

List of Abbreviations

$\frac{\beta^2}{2}$ probability for a PEP violation

ADC   Analog to Digital Converter

APD   Avalanch PhotoDiode

BOREXINO   BORon solar neutrino EXperiment

BTF   Beam Test Facility

CDF   Cumulative Distribution Function

CERN   Conseil Européen pour la Recherche Nucléaire

CFD   Constant Fraction Discriminator

CL   Confidence Level

CPT   Charge, Parity and Time reversal symmetry

DAMA   DArk MAtter

DAΦNE   Double Annular Φ Factory for Nice Experiments

DAQ   Data Acquisition

FET   Field Effect Transistor

FOUT   Fast OUTput

FWF   Fonds zur Förderung der wissenschaftlichen Forschung

FWHM   Full Width Half Maximum

GEANT   GEometry ANd Tracking

GPIB   General Purpose Interface Bus

LNF   Laboratori Nazionali di Frascati

LNGS   Laboratori Nazionali del Gran Sasso

MC   Monte Carlo

MCDF   MultiConfiguration Dirac-Fock

MG superselection rule   Messiah-Greenberg superseletion rule

NI   National Instruments

PENELOPE   PENetration and Energy LOss of Positrons and Electrons

PEP   Pauli Exclusion Principle

PID   Proportional Integral Derivative

PIXE   Particle Induced X-ray Emission

PPD   Posterior Probability Density

QDC   Charge to Digital Converter

ROI   Region Of Interest

SDD   Silicon Drift Detector

SIDDHARTA   SIlicon Drift Detector for Hadronic Atom Research by Timing
Application

SiPM   Silicon Photomultiplier

SMI   Stefan Meyer Institute

TDC   Time to Digital Converter

USB   Universal Serial Bus

VIP(2)   VIolation of the Pauli Principle (2)

List of Tables

List of Figures

Appendices

A. Systematic Uncertainties

This section represents a preliminary analysis of systematic uncertainties in the calculation of the upper limit on the probability for the violation of the PEP. Two checks for systematic uncertainties have already been mentioned in the main text: Firstly, in section 6.1, the rate of background as a function of data taking time was analyzed. No deviation was found from the expected statistical fluctuation around a mean value. Secondly, this mean value of the rate of background events was compared to MC simulations (in section 6.5), where at least the constant part of the spectrum (which is interesting for the analysis), is comparable. These two checks exclude noise in the SDDs and other sources causing a fluctuation of the background event rate as a potential source of systematic errors. As was suggested in [59], this excluded potential source of systematics is not included in the total systematic error.

The formula for calculating the upper limit of a PEP violation is (see also equation 7.4):

$$\frac{\beta^2}{2} \leq \frac{10\mu e}{D\sum\left(I\Delta t\right)}\frac{\Delta N_x}{\left(\text{detection efficiency}\right)}. \tag{A.1}$$

Errors can influence the final value for $\frac{\beta^2}{2}$ on the one hand by changing the number of possible detected counts ΔN_x from PEP-violating transitions, which is obtained from the experimental data. On the other hand, systematic errors can influence the other terms in the equation, which correspond to characteristics of the setup.

In table A.1, the uncertainties for different systematic effects on ΔN_x are listed. The effect in the first line accounts for changes in binning. The value 3×3 in the case of the simultaneous fit means that ΔN_x varies with $\sigma = 3$ counts when changing the binning. Furthermore, the effect of a change in the peak position of the PEP-violating transition is explored. This accounts for the uncertainty of 10 eV in its calculation given in [53] and the fact that there is another possible PEP-forbidden transition at 7729 eV. Also this accounts for the effect that the energy spectrum might be slightly shifted due to uncertainties in the energy calibration (see for example table 6.3). The uncertainty in ΔN_x from the uncertainty in energy resolution (see equation 7.7) is given in the third line. The last considered effect

	Spectrum Subtraction	Simultaneous Fit	Bayesian Subtraction	Bayesian Fit
Binning	-	3×3	-	3×4
PEP-violating Peak Position	3×10	3×9	3×10	3×10
Energy Resolution	3×2	3×3	3×2	3×8
Tail Components	3×4	-	3×6	-
Total Systematic Error	3×11	3×10	3×12	3×13
Change in Upper Limit	2 / 0.7 %	1.8 / 0.7 %	1.8 / 0.5 %	2 / 0.5 %

Table A.1.: Preliminary calculations of the contribution of different systematic effects on ΔN_x. The effects are displayed as $3 \times \sigma_{sys}$ of ΔN_x. The total systematic error is calculated assuming uncorrelated individual errors.

deals with the influence of tails of the Cu Kα and Ni Kα, which one could subtract from the events in the ROI, as they potentially introduce an artificial difference between the histograms with and without current. Some analysis methods by definition are not sensible to certain systematic effects, which is noted by a "-" sign in the table. In particular, the spectrum subtraction method does not depend on the binning of the histogram, as it counts events in a certain energy region. Furthermore, fit methods do not depend on if tails are subtracted or not, as they take into account all features of the spectrum by default, including the tails.

Comparing these values with the ones given in chapter 7 for the statistical errors, it is obvious that the statistical errors are the dominant factor in the calculation of an upper limit for ΔN_x. Adding the statistical and the systematic error in quadrature to get the new upper limit for the spectral subtraction method gives

$$3 \times \sqrt{91^2 + 11^2} = 275. \tag{A.2}$$

This is a change from the pure statistical limit of $3 \times 91 = 273$ by only 0.7 %. Similar results are obtained for the other analysis methods, which are given in the table. This means that the inclusion of systematic effects on ΔN_x only changes the upper limit by a small amount.

Contributions of systematic uncertainties from experimental parameters to the cal-

culation of $\frac{\beta^2}{2}$ are listed in table A.2 Firstly the statistical uncertainty of the MC

	Detection Efficiency	Number of Scatterings
Systematic Error	0.01 %	possibly large

Table A.2.: Contribution of different systematic effects on experimental parameters.

simulation of the detection efficiency is given (see chapter 4). With 10^6 particles used in the simulation, the statistical uncertainty is 0.01 %. Therefore its contribution is minor. Another possible uncertainty comes from the amount of scattering events, which is estimated to be on the order of $\frac{D}{\mu}$ in equation A.1, where D is the target length and μ is the mean free path length. Recent calculation given in [60], which assume a random walk of the electron through the conductor, come to the conclusion that the number of scatterings might be higher than that by orders of magnitude. As this result is not yet published, it will not be further discussed.

As the analysis in this chapter is preliminary, it is not included in the main text.

B. Data Acquisition Layout
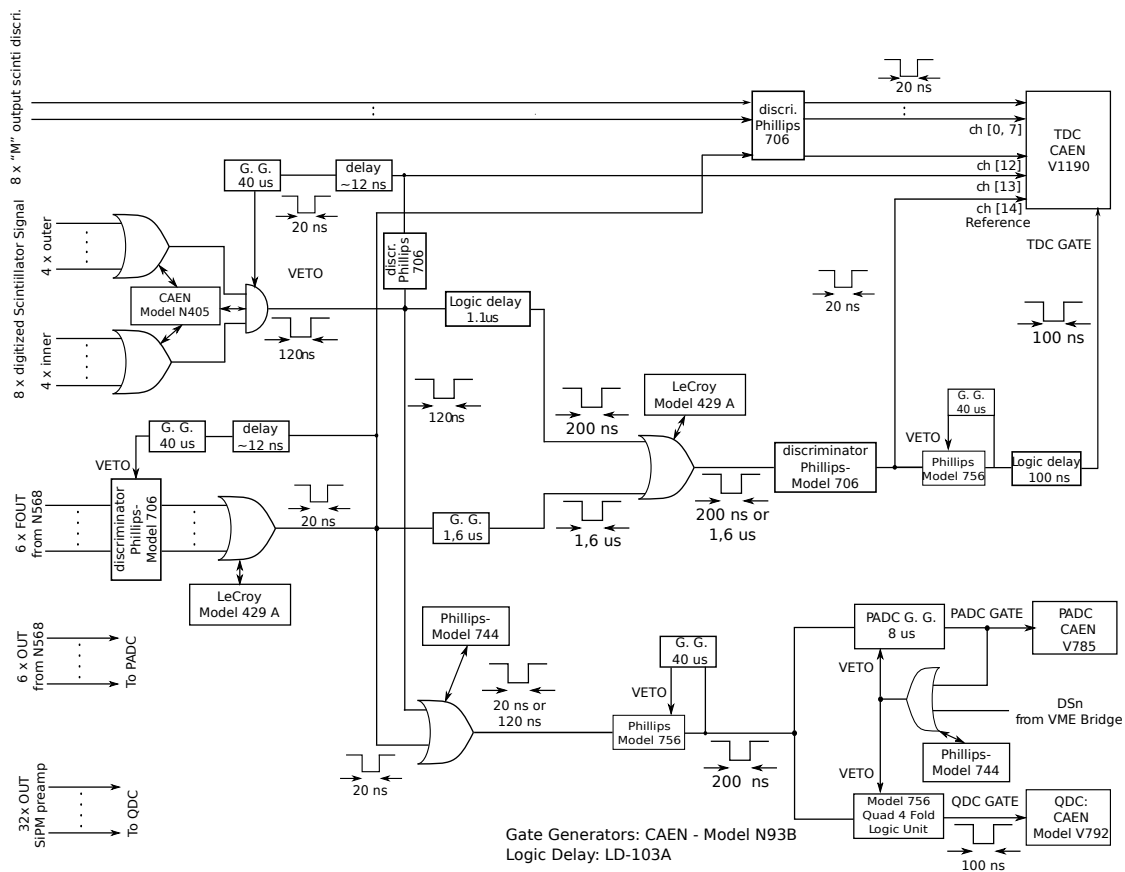
Figure B.1.: Layout of the data acquisition system for the VIP2 experiment

C. Code for Fit Function

```
Double_t TiMnCuFullFitFunc(Double_t *x, Double_t *par)
{
    Double_t timncu_function = 0.;
    Double_t arg[33] = {0.};


    Double_t slope = (par[9] - par[5])/(MnKa1 - TiKa1); // par[9] = init_mean_mn
        ↪ ; par[5]=init_mean_ti; slope in ch / eV

    Double_t mnka2m = par[9] - (MnKa1 - MnKa2) * slope; // mn ka2 start value
        ↪ channel
    Double_t mnka1e = par[9] - SiKa * slope; // channel with a mnka1 photon
        ↪ absorbed by Si -> lost energy not recorded
    Double_t mnka2e = mnka2m - SiKa * slope; // same for mn-ka2
    Double_t mnkbe = par[11]- SiKa * slope; // par[11]=init_mean_mnkb, same for
        ↪ mn-kb
    Double_t tmnka1m = par[9] - par[14] * slope; // par[14]=Tail mean shift [eV]
    Double_t tmnka2m = mnka2m - par[14] * slope; // same for mn-ka2
    Double_t tmnkbm = par[11]- par[14] * slope; // same for mn-kb

    Double_t sig_MnKa1 = sqrt( slope * par[9] * SiW * par[3] + par[4] * par[4] )
        ↪ ;
    Double_t sig_MnKa2 = sqrt( slope * mnka2m * SiW * par[3] + par[4] * par[4] )
        ↪ ;
    Double_t sig_MnKb = sqrt( slope * par[11]* SiW * par[3] + par[4] * par[4] );
    Double_t sig_MnKa1e = sqrt( slope * mnka1e * SiW * par[3] + par[4] * par[4]
        ↪ );
    Double_t sig_MnKa2e = sqrt( slope * mnka2e * SiW * par[3] + par[4] * par[4]
        ↪ );
    Double_t sig_MnKbe = sqrt( slope * mnkbe * SiW * par[3] + par[4] * par[4] );
    Double_t sig_tMnKa1 = sqrt( slope * tmnka1m* SiW * par[3] + par[4] * par[4]
        ↪ );
    Double_t sig_tMnKa2 = sqrt( slope * tmnka2m* SiW * par[3] + par[4] * par[4]
        ↪ );
    Double_t sig_tMnKb = sqrt( slope * tmnkbm * SiW * par[3] + par[4] * par[4] )
        ↪ ;

    Double_t tika2m = par[5] - (TiKa1 - TiKa2) * slope; // TiKa2 mean channel
```

```
Double_t tika1e = par[5] - SiKa * slope;
Double_t tika2e = tika2m - SiKa * slope;
Double_t tikbe = par[7] - SiKa * slope; // par[7]=Ti-Kb channel
Double_t ttika1m = par[5] - par[14] * slope;
Double_t ttika2m = tika2m - par[14] * slope;
Double_t ttikbm = par[7] - par[14] * slope;

Double_t sig_TiKa1 = sqrt( slope * par[5] * SiW * par[3] + par[4] * par[4] )
    ↪ ;
Double_t sig_TiKa2 = sqrt( slope * tika2m * SiW * par[3] + par[4] * par[4] )
    ↪ ;
Double_t sig_TiKb = sqrt( slope * par[7] * SiW * par[3] + par[4] * par[4] );
Double_t sig_TiKa1e = sqrt( slope * tika1e * SiW * par[3] + par[4] * par[4]
    ↪ );
Double_t sig_TiKa2e = sqrt( slope * tika2e * SiW * par[3] + par[4] * par[4]
    ↪ );
Double_t sig_TiKbe = sqrt( slope * tikbe * SiW * par[3] + par[4] * par[4] );
Double_t sig_tTiKa1 = sqrt( slope * ttika1m* SiW * par[3] + par[4] * par[4]
    ↪ );
Double_t sig_tTiKa2 = sqrt( slope * ttika2m* SiW * par[3] + par[4] * par[4]
    ↪ );
Double_t sig_tTiKb = sqrt( slope * ttikbm * SiW * par[3] + par[4] * par[4] )
    ↪ ;

Double_t cuka2m = par[22] - (CuKa1 - CuKa2) * slope; // cu ka2 start value
    ↪ channel
Double_t cuka1e = par[22] - SiKa * slope; // channel with a cuka1 photon
    ↪ absorbed by Si -> lost energy not recorded
Double_t cuka2e = cuka2m - SiKa * slope; // same for cu-ka2
Double_t cukbe = par[24]- SiKa * slope; // par[24]=init_mean_cukb, same for
    ↪ cu-kb
Double_t tcuka1m = par[22] - par[14] * slope; // par[14]=Tail mean shift [eV
    ↪ ]
Double_t tcuka2m = mnka2m - par[14] * slope; // same for cu-ka2
Double_t tcukbm = par[24]- par[14] * slope; // same for cu-kb

Double_t sig_CuKa1 = sqrt( slope * par[22] * SiW * par[3] + par[4] * par[4]
    ↪ );
Double_t sig_CuKa2 = sqrt( slope * cuka2m * SiW * par[3] + par[4] * par[4] )
    ↪ ;
Double_t sig_CuKb = sqrt( slope * par[24]* SiW * par[3] + par[4] * par[4] );
Double_t sig_CuKa1e = sqrt( slope * cuka1e * SiW * par[3] + par[4] * par[4]
    ↪ );
Double_t sig_CuKa2e = sqrt( slope * cuka2e * SiW * par[3] + par[4] * par[4]
    ↪ );
Double_t sig_CuKbe = sqrt( slope * cukbe * SiW * par[3] + par[4] * par[4] );

Double_t sig_tCuKa1 = sqrt( slope * tcuka1m* SiW * par[3] + par[4] * par[4]
    ↪ );
```

```
Double_t sig_tCuKa2 = sqrt( slope * tcuka2m* SiW * par[3] + par[4] * par[4]
    ↪ );
Double_t sig_tCuKb = sqrt( slope * tcukbm * SiW * par[3] + par[4] * par[4] )
    ↪ ;

if( sig_TiKa1 * sig_TiKa2 * sig_TiKb * sig_MnKa1 * sig_MnKa2 * sig_MnKb
        * sig_CuKa1 * sig_CuKa2 * sig_CuKb
        * sig_tTiKa1 * sig_tTiKa2 * sig_tTiKb * sig_tMnKa1 * sig_tMnKa2 *
            ↪ sig_tMnKb
        * sig_MnKa1e * sig_MnKa2e * sig_MnKbe * sig_TiKa1e * sig_TiKa2e *
            ↪ sig_TiKbe
        != 0){

    arg[0] = (x[0] - par[5])/sig_TiKa1;
    arg[1] = (x[0] - tika2m)/sig_TiKa2;
    arg[2] = (x[0] - par[7])/sig_TiKb;
    arg[21] = (x[0] - tika1e)/sig_TiKa1e; // Escape peak
    arg[22] = (x[0] - tika2e)/sig_TiKa2e;
    arg[23] = (x[0] - tikbe)/sig_TiKbe;

    arg[3] = (x[0] - par[9])/sig_MnKa1;
    arg[4] = (x[0] - mnka2m)/sig_MnKa2;
    arg[5] = (x[0] - par[11])/sig_MnKb;
    arg[6] = (x[0] - mnka1e)/sig_MnKa1e; // Escape peak
    arg[7] = (x[0] - mnka2e)/sig_MnKa2e;
    arg[20] = (x[0] - mnkbe) /sig_MnKbe;

    arg[24] = (x[0] - par[22])/sig_CuKa1; // cu ka1
    arg[25] = (x[0] - cuka2m)/sig_CuKa2;
    arg[26] = (x[0] - par[24])/sig_CuKb;
    arg[27] = (x[0] - cuka1e)/sig_CuKa1e; // Escape peak
    arg[28] = (x[0] - cuka2e)/sig_CuKa2e;
    arg[29] = (x[0] - cukbe) /sig_CuKbe;

    arg[11] = (x[0] - ttika1m)/sig_tTiKa1/SQRT2;
    Double_t argtika1B1 = (x[0] - ttika1m)/sig_tTiKa1/par[19]; //par[19]=
        ↪ tail beta slope
    Double_t argtika1B2 = 1./par[19]/SQRT2;
    Double_t argtika1B3 = 1./2./par[19]/par[19];
    Double_t normtika1 = 1./2./sig_tTiKa1/par[19]*TMath::Exp(argtika1B3);
    arg[12] = (x[0] - ttika2m)/sig_tTiKa2/SQRT2;
    Double_t argtika2B1 = (x[0] - ttika2m)/sig_tTiKa2/par[19];
    Double_t argtika2B2 = 1./par[19]/SQRT2;
    Double_t argtika2B3 = 1./2./par[19]/par[19];
    Double_t normtika2 = 1./2./sig_tTiKa2/par[19]*TMath::Exp(argtika2B3);
    arg[13] = (x[0] - ttikbm) /sig_tTiKb/SQRT2;
    Double_t argtikbB1 = (x[0] - ttikbm)/sig_tTiKb/par[19];
    Double_t argtikbB2 = 1./par[19]/SQRT2;
    Double_t argtikbB3 = 1./2./par[19]/par[19];
```

```
        Double_t normtikb = 1./2./sig_tTiKb/par[19]*TMath::Exp(argtikbB3);

        arg[17] = (x[0] - tmnka1m)/sig_tMnKa1/SQRT2;
        Double_t argmnka1B1 = (x[0] - tmnka1m)/sig_tMnKa1/par[20];
        Double_t argmnka1B2 = 1./par[20]/SQRT2;
        Double_t argmnka1B3 = 1./2./par[20]/par[20];
        Double_t normmnka1 = 1./2./sig_tMnKa1/par[20]*TMath::Exp(argmnka1B3);
        arg[18] = (x[0] - tmnka2m)/sig_tMnKa2/SQRT2;
        Double_t argmnka2B1 = (x[0] - tmnka2m)/sig_tMnKa2/par[20];
        Double_t argmnka2B2 = 1./par[20]/SQRT2;
        Double_t argmnka2B3 = 1./2./par[20]/par[20];
        Double_t normmnka2 = 1./2./sig_tMnKa2/par[20]*TMath::Exp(argmnka2B3);
        arg[19] = (x[0] - tmnkbm) /sig_tMnKb/SQRT2;
        Double_t argmnkbB1 = (x[0] - tmnkbm)/sig_tMnKb/par[20];
        Double_t argmnkbB2 = 1./par[20]/SQRT2;
        Double_t argmnkbB3 = 1./2./par[20]/par[20];
        Double_t normmnkb = 1./2./sig_tMnKb/par[20]*TMath::Exp(argmnkbB3);


        arg[30] = (x[0] - tcuka1m)/sig_tCuKa1/SQRT2;
        Double_t argcuka1B1 = (x[0] - tcuka1m)/sig_tCuKa1/par[20];
        Double_t argcuka1B2 = 1./par[20]/SQRT2;
        Double_t argcuka1B3 = 1./2./par[20]/par[20];
        Double_t normcuka1 = 1./2./sig_tCuKa1/par[20]*TMath::Exp(argcuka1B3);
        arg[31] = (x[0] - tcuka2m)/sig_tCuKa2/SQRT2;
        Double_t argcuka2B1 = (x[0] - tcuka2m)/sig_tCuKa2/par[20];
        Double_t argcuka2B2 = 1./par[20]/SQRT2;
        Double_t argcuka2B3 = 1./2./par[20]/par[20];
        Double_t normcuka2 = 1./2./sig_tCuKa2/par[20]*TMath::Exp(argcuka2B3);
        arg[32] = (x[0] - tcukbm) /sig_tCuKb/SQRT2;
        Double_t argcukbB1 = (x[0] - tcukbm)/sig_tCuKb/par[20];
        Double_t argcukbB2 = 1./par[20]/SQRT2;
        Double_t argcukbB3 = 1./2./par[20]/par[20];
        Double_t normcukb = 1./2./sig_tCuKb/par[20]*TMath::Exp(argcukbB3);



timncu_function = backFunc(x,par)
        + par[6] / sig_TiKa1* TMath::Exp(-0.5 * arg[0] * arg[0]) //par[6] =
          ↪ ti ka1 gain Ti ka1 gauss
        + TiKa2_RI/ TiKa1_RI * par[6] / sig_TiKa2 * TMath::Exp(-0.5 * arg[1]
          ↪ * arg[1]) // 100/50 for ti
        + par[8] * par[6] / sig_TiKb * TMath::Exp(-0.5 * arg[2] * arg[2]) //
          ↪ par[8]=ti kb to ka gain ratio
        + par[6] * par[15] * normtika1 * TMath::Exp(argtika1B1) * TMath::
          ↪ Erfc(arg[11] + argtika1B2)// par[15]=ti tail gain ratio ka1
        + par[6] * par[15] * TiKa2_RI / TiKa1_RI * normtika2 * TMath::Exp(
          ↪ argtika2B1) * TMath::Erfc(arg[12] + argtika2B2) // ka2
```

```
        + par[6] * par[16] * par[8] * normtikb * TMath::Exp(argtikbB1) *
        ↪ TMath::Erfc(arg[13] + argtikbB2) // kb

        + par[10] / sig_MnKa1* TMath::Exp(-0.5 * arg[3] * arg[3]) // par[10]
        ↪ = mn ka1 gain
        + MnKa2_RI/ MnKa1_RI * par[10] / sig_MnKa2 * TMath::Exp(-0.5 * arg
        ↪ [4] * arg[4])
        + par[12] * par[10] / sig_MnKb * TMath::Exp(-0.5 * arg[5] * arg[5])
        ↪ // par[12]=mn kb to ka gain ratio (0.7 in one fit for lngs)
        + par[10] * par[17] * normmnka1 * TMath::Exp(argmnka1B1) * TMath::
        ↪ Erfc(arg[17] + argmnka1B2)
        + par[10] * par[17] * MnKa2_RI / MnKa1_RI * normmnka2 * TMath::Exp(
        ↪ argmnka2B1) * TMath::Erfc(arg[18] + argmnka2B2)
        + par[10] * par[18] * par[12] * normmnkb * TMath::Exp(argmnkbB1) *
        ↪ TMath::Erfc(arg[19] + argmnkbB2)

        + par[23] / sig_CuKa1* TMath::Exp(-0.5 * arg[24] * arg[24]) // cu
        ↪ ka1 peak
        + CuKa2_RI/ CuKa1_RI * par[23] / sig_CuKa2 * TMath::Exp(-0.5 * arg
        ↪ [25] * arg[25]) // cu ka2
        + par[25] * par[23] / sig_CuKb * TMath::Exp(-0.5 * arg[26] * arg
        ↪ [26]) // par[12]=mn kb to ka gain ratio (0.7 in one fit for
        ↪ lngs) - cu kb
        + par[23] * par[26] * normcuka1 * TMath::Exp(argcuka1B1) * TMath::
        ↪ Erfc(arg[30] + argcuka1B2) // cu ka1 tail
        + par[23] * par[26] * CuKa2_RI / CuKa1_RI * normcuka2 * TMath::Exp(
        ↪ argcuka2B1) * TMath::Erfc(arg[31] + argcuka2B2) // cu ka2 tail
        + par[23] * par[25] * par[26] * normcukb * TMath::Exp(argcukbB1) *
        ↪ TMath::Erfc(arg[32] + argcukbB2) // cu kb tail

        + par[13] * par[10] / sig_MnKa1e * TMath::Exp(-0.5 * arg[6] * arg
        ↪ [6]) // Escape peak ... mn ka1
        + par[13] * par[10] / sig_MnKa2e * TMath::Exp(-0.5 * arg[7] * arg
        ↪ [7]) // mn ka 2
        + par[13] * par[10] / sig_MnKbe * TMath::Exp(-0.5 * arg[20]* arg
        ↪ [20]) // mn kb


        + par[13] * par[6] / sig_TiKa1e * TMath::Exp(-0.5 * arg[21] * arg
        ↪ [21]) // escape peak ti ka1
        + par[13] * par[6] / sig_TiKa2e * TMath::Exp(-0.5 * arg[22] * arg
        ↪ [22]) // ka2
        + par[13] * par[6] / sig_TiKbe * TMath::Exp(-0.5 * arg[23] * arg
        ↪ [23]) // kb

        + par[21] * par[10] * (1./2) * TMath::Erfc( (x[0]-par[9])/(SQRT2*
        ↪ sig_MnKa1) ) // mn ka1 shelf
        + par[21] * MnKa2_RI/ MnKa1_RI * par[10] * (1./2) * TMath::Erfc( (x
        ↪ [0]-mnka2m)/(SQRT2*sig_MnKa2) ) // ka2
```

```
            + par[21] * par[12] * par[10] * (1./2) * TMath::Erfc( (x[0]-par[11])
                ↪ /(SQRT2*sig_MnKb) ) // kb

            + par[21] * par[6] * (1./2) * TMath::Erfc( (x[0]-par[5])/(SQRT2*
                ↪ sig_TiKa1) ) // ti ka1 shelf
            + par[21] * TiKa2_RI/ TiKa1_RI * par[6] * (1./2) * TMath::Erfc( (x
                ↪ [0]-tika2m)/(SQRT2*sig_TiKa2) )
            + par[21] * par[8] * par[6] * (1./2) * TMath::Erfc( (x[0]-par[7])/(
                ↪ SQRT2*sig_TiKb) );

    }
    return timncu_function;
}
```

D. Code for Simultaneous Fit

```
Double_t funcBg(Double_t *x, Double_t *par){

    // fit of the region of roi, nickel, and cu ka kb
    // this is for fitting an already scaled histogram


    Double_t xx = x[0];

    //par[0] = background constant
    //par[10] = background slope

    Double_t back = par[0] + (xx - 7000) * par[10];

    //par[1] = cu ka1 gain
    //par[2] = cu ka1 mean
    //par[3] = cu ka1 sigma

    Double_t cuKa1 = par[1]/(sqrt(2*TMath::Pi())*par[3])*TMath::Exp(-((xx-par
        ↪ [2])*(xx-par[2]))/(2*par[3]*par[3]));

    Double_t cuKa2Gain = par[1] * 0.51;
    Double_t cuKa2Mean = par[2] - 19.95;

    Double_t cuKa2 = cuKa2Gain/(sqrt(2*TMath::Pi())*par[3])*TMath::Exp(-((xx-
        ↪ cuKa2Mean)*(xx-cuKa2Mean))/(2*par[3]*par[3]));

    //par[4] = cu kb gain
    //par[5] = cu kb mean
    //par[6] = cu kb sigma

    Double_t cuKb = par[4]/(sqrt(2*TMath::Pi())*par[6])*TMath::Exp(-((xx-par[5])
        ↪ *(xx-par[5]))/(2*par[6]*par[6]));

    //par[7] = ni ka1 gain
    //par[8] = ni ka1 mean
    //par[9] = ni ka1 sigma
```

```
    Double_t niKa1 = par[7]/(sqrt(2*TMath::Pi())*par[9])*TMath::Exp(-((xx-par
        ↪ [8])*(xx-par[8]))/(2*par[9]*par[9]));

    Double_t niKa2Gain = par[7] * 0.51;
    Double_t niKa2Mean = par[8] - 17.3;

    Double_t niKa2 = niKa2Gain/(sqrt(2*TMath::Pi())*par[9])*TMath::Exp(-((xx-
        ↪ niKa2Mean)*(xx-niKa2Mean))/(2*par[9]*par[9]));


    Double_t roiCuFunc = back + cuKa1 + cuKa2 + cuKb + niKa1 + niKa2;


    return roiCuFunc;
}

Double_t funcSigBg(Double_t *x, Double_t *par){

    // fit of the region of roi, nickel, and cu ka kb
    // this is for fitting an already scaled histogram


    Double_t xx = x[0];

    //par[0] = background constant
    //par[10] = background slope

    Double_t back = par[0] + (xx - 7000) * par[10];

    //par[1] = cu ka1 gain
    //par[2] = cu ka1 mean
    //par[3] = cu ka1 sigma

    Double_t cuKa1 = par[1]/(sqrt(2*TMath::Pi())*par[3])*TMath::Exp(-((xx-par
        ↪ [2])*(xx-par[2]))/(2*par[3]*par[3]));

    Double_t cuKa2Gain = par[1] * 0.51;
    Double_t cuKa2Mean = par[2] - 19.95;

    Double_t cuKa2 = cuKa2Gain/(sqrt(2*TMath::Pi())*par[3])*TMath::Exp(-((xx-
        ↪ cuKa2Mean)*(xx-cuKa2Mean))/(2*par[3]*par[3]));

    //par[4] = cu kb gain
    //par[5] = cu kb mean
    //par[6] = cu kb sigma

    Double_t cuKb = par[4]/(sqrt(2*TMath::Pi())*par[6])*TMath::Exp(-((xx-par[5])
        ↪ *(xx-par[5]))/(2*par[6]*par[6]));
```

```
    //par[7] = ni ka1 gain
    //par[8] = ni ka1 mean
    //par[9] = ni ka1 sigma


    Double_t niKa1 = par[7]/(sqrt(2*TMath::Pi())*par[9])*TMath::Exp(-((xx-par
        ↪ [8])*(xx-par[8]))/(2*par[9]*par[9]));

    Double_t niKa2Gain = par[7] * 0.51;
    Double_t niKa2Mean = par[8] - 17.3;

    Double_t niKa2 = niKa2Gain/(sqrt(2*TMath::Pi())*par[9])*TMath::Exp(-((xx-
        ↪ niKa2Mean)*(xx-niKa2Mean))/(2*par[9]*par[9]));

    //par[11] = forbidden gauss gain
    // mean of forbidden transition fixed at 7747 eV

    Double_t forbGauss = par[11]/(sqrt(2*TMath::Pi())*par[3])*TMath::Exp(-((xx
        ↪ -7747)*(xx-7747))/(2*par[3]*par[3]));

    Double_t roiCuFunc = back + cuKa1 + cuKa2 + cuKb + niKa1 + niKa2 + forbGauss
        ↪ ;


    return roiCuFunc;
}

struct GlobalChi2 {
   GlobalChi2( ROOT::Math::IMultiGenFunction & f1, ROOT::Math::
       ↪ IMultiGenFunction & f2) :
     fChi2_1(&f1), fChi2_2(&f2) {}

  // parameter vector is first background (in common 1 and 2) and then is
      ↪ signal (only in 2)
  double operator() (const double *par) const {
    double p1[11]; // p1 is for background = without current histogram
    p1[0] = par[0]; // bg constant ..common parameter
    p1[1] = par[1]; // cu ka1 gain ... free
    p1[2] = par[2]; // cu ka1 mean ... fixed
    p1[3] = par[3]; // cu ka1 sigma ... free
    p1[4] = par[4]; // cu kb gain ... free
    p1[5] = par[5]; // cu kb mean ... fixed
    p1[6] = par[6]; // cu kb sigma ... free
    p1[7] = par[7]; // ni ka1 gain ... free
    p1[8] = par[8]; // ni ka1 mean ... fixed
    p1[9] = par[9]; // ni ka1 sigma ... free
    p1[10] = par[10]; // background slope ... common

    double p2[12]; // parameters for the fit with signal with current
```

```
      p2[0] = par[0]; // bg constant ..common parameter
      p2[1] = par[11]; // cu ka1 gain ... free
      p2[2] = par[12]; // cu ka1 mean ... fixed
      p2[3] = par[13]; // cu ka1 sigma ... free
      p2[4] = par[14]; // cu kb gain ... free
      p2[5] = par[15]; // cu kb mean ... fixed
      p2[6] = par[16]; // cu kb sigma ... free
      p2[7] = par[17]; // ni ka1 gain ... free
      p2[8] = par[18]; // ni ka1 mean ... fixed
      p2[9] = par[19]; // ni ka1 sigma ... free
      p2[10] = par[10]; // background slope ... common
      p2[11] = par[20]; // forbidden gauss gain ... free
      return (*fChi2_1)(p1) + (*fChi2_2)(p2);
   }

   const ROOT::Math::IMultiGenFunction * fChi2_1;
   const ROOT::Math::IMultiGenFunction * fChi2_2;
};

Double_t combinedFit(Int_t reBin) {

  TFile *fIN = new TFile("energyHistograms.root");
  Int_t nPar = 21;
  Int_t lowerL = 7000;
  Int_t upperL = 9500;

  TH1F *hSB = (TH1F*)fIN->Get("withCurrentSum");
  TH1F *hB = (TH1F*)fIN->Get("noCurrentSmallSum");

  // setting the initial parameters for the fit
  Double_t parInit[21] = { 510. * reBin/25 , 310000. * reBin/25 , 8047.78 , 75.
      ↪  , 79000. * reBin/25 , 8905.29 , 80. , 14900. * reBin/25 , 7478.15 ,
      ↪ 72. , -0.02 , 312000. * reBin/25 , 8047.78 , 80. , 78500. * reBin/25 ,
      ↪ 8905.29 , 78. , 12000. * reBin/25 , 7478.15 , 71. , 0. };

  hSB->Rebin(reBin);
  hB->Rebin(reBin);


  TF1 *fB = new TF1("fB", funcBg, lowerL, upperL, 11 );
  TF1 *fSB = new TF1("fSB", funcSigBg, lowerL, upperL, 12 );


  // perform global fit


  ROOT::Math::WrappedMultiTF1 wfB(*fB,1);
  ROOT::Math::WrappedMultiTF1 wfSB(*fSB,1);
```

```
ROOT::Fit::DataOptions opt;
ROOT::Fit::DataRange rangeB;
rangeB.SetRange(lowerL,upperL);
ROOT::Fit::BinData dataB(opt,rangeB);
ROOT::Fit::FillData(dataB, hB);

ROOT::Fit::DataRange rangeSB;
rangeSB.SetRange(lowerL,upperL);
ROOT::Fit::BinData dataSB(opt,rangeSB);
ROOT::Fit::FillData(dataSB, hSB);

ROOT::Fit::Chi2Function chi2_B(dataB, wfB);
ROOT::Fit::Chi2Function chi2_SB(dataSB, wfSB);

GlobalChi2 globalChi2(chi2_B, chi2_SB);

ROOT::Fit::Fitter fitter;



// create before the parameter settings in order to fix or set range on them
fitter.Config().SetParamsSettings(21,parInit);
// fix some parameters
fitter.Config().ParSettings(2).Fix();
fitter.Config().ParSettings(5).Fix();
fitter.Config().ParSettings(8).Fix();
fitter.Config().ParSettings(12).Fix();
fitter.Config().ParSettings(15).Fix();
fitter.Config().ParSettings(18).Fix();


fitter.Config().ParSettings(0).SetName("Common Background Constant");
fitter.Config().ParSettings(1).SetName("Cu Ka1 Gain BG");
fitter.Config().ParSettings(2).SetName("Cu Ka1 Mean");
fitter.Config().ParSettings(3).SetName("Cu Ka1 Sigma BG");
fitter.Config().ParSettings(4).SetName("Cu Kb Gain BG");
fitter.Config().ParSettings(5).SetName("Cu Kb Mean");
fitter.Config().ParSettings(6).SetName("Cu Kb Sigma BG");
fitter.Config().ParSettings(7).SetName("Ni Ka1 Gain BG");
fitter.Config().ParSettings(8).SetName("Ni Ka1 Mean");
fitter.Config().ParSettings(9).SetName("Ni Ka1 Sigma BG");
fitter.Config().ParSettings(10).SetName("Common Background Slope");
fitter.Config().ParSettings(11).SetName("Cu Ka1 Gain SIG");
fitter.Config().ParSettings(12).SetName("Cu Ka1 Mean");
fitter.Config().ParSettings(13).SetName("Cu Ka1 Sigma SIG");
fitter.Config().ParSettings(14).SetName("Cu Kb Gain SIG");
fitter.Config().ParSettings(15).SetName("Cu Kb Mean");
fitter.Config().ParSettings(16).SetName("Cu Kb Sigma SIG");
fitter.Config().ParSettings(17).SetName("Ni Ka1 Gain SIG");
```

```
fitter.Config().ParSettings(18).SetName("Ni Ka1 Mean");
fitter.Config().ParSettings(19).SetName("Ni Ka1 Sigma SIG");
fitter.Config().ParSettings(20).SetName("Forbidden Gauss Gain");


// set limits
fitter.Config().ParSettings(0).SetLimits(400. * reBin/25,600. * reBin/25);
fitter.Config().ParSettings(1).SetLimits(200000. * reBin/25,400000. * reBin
    ↪ /25);

fitter.Config().ParSettings(3).SetLimits(72.,80.);
fitter.Config().ParSettings(4).SetLimits(70000. * reBin/25,90000. * reBin/25)
    ↪ ;

fitter.Config().ParSettings(6).SetLimits(75.,85.);
fitter.Config().ParSettings(7).SetLimits(10000. * reBin/25,20000. * reBin/25)
    ↪ ;

fitter.Config().ParSettings(9).SetLimits(60. ,85. );
fitter.Config().ParSettings(10).SetLimits(-0.05,0.05);
fitter.Config().ParSettings(11).SetLimits(200000. * reBin/25,400000. * reBin
    ↪ /25);

fitter.Config().ParSettings(13).SetLimits(75.,85.);
fitter.Config().ParSettings(14).SetLimits(70000. * reBin/25,90000. * reBin
    ↪ /25);

fitter.Config().ParSettings(16).SetLimits(75.,85.);
fitter.Config().ParSettings(17).SetLimits(10000. * reBin/25,15000. * reBin
    ↪ /25);

fitter.Config().ParSettings(19).SetLimits(65.,75.);
//fitter.Config().ParSettings(20).SetLimits(0.,5000.); // no limits on
    ↪ forbidden gauss gain

fitter.Config().SetMinosErrors();
fitter.Config().MinosErrors();
fitter.FitFCN(nPar,globalChi2,parInit,dataB.Size()+dataSB.Size());

ROOT::Fit::FitResult result = fitter.Result();
result.Print(std::cout);
```

E. Code for Bayesian Analysis

E.1. Count Based Analysis

```
RndList = {};
xs = 4202;
xbg = 4105;
lbgList = {};
expect = xs - xbg;
xValList = Range[0, 700];
For[i = 1, i < 1000000, i++,
  lbg = RandomVariate[GammaDistribution[xbg + 1, 1]];
  probDist = ProbabilityDistribution[(lsg + lbg)^xs*Exp[-lsg]/
  (Exp[lbg]* Gamma[1 + xs, lbg]), {lsg, 0, Infinity}];
  yValList = {};
  yValList = N[PDF[probDist, xValList]];
  empDistTemp = EmpiricalDistribution[yValList -> xValList];
  r = N[RandomVariate[empDistTemp]];
  AppendTo[RndList, r];
  AppendTo[lbgList, lbg];
]
```

E.2. Fit Based Analysis

```
RooRealVar backC("backC","number␣of␣bg␣events␣without␣current"
    ↪ ,31838.4,10000.,50000.);
backC.setConstant(kTRUE);

RooRealVar backSl("backSl","slope␣of␣the␣bg␣without␣current",-0.05176,-1.,1.)
    ↪ ;
backSl.setConstant(kTRUE);
// set the background parameters to the values from the fit without current
// set them also constant for the fit

 //CuKa1
```

```
RooRealVar meanCuKa1("meanCuKa1","mean␣of␣Cu␣Ka1␣gaussian"
    ↪ ,8047.78,8040.,8080.);
RooRealVar sigmaCuKa("sigmaCuKa","width␣of␣Cu␣Ka1␣gaussian",75.,70.,90.);
RooGaussian gaussCuKa1("gaussCuKa1","Cu␣Ka1␣PDF",energy,meanCuKa1,sigmaCuKa);

RooRealVar cuKa1N("cuKa1N","cu␣Ka1␣Events",15000,0,100000);

//Cuka2

RooRealVar CuKa2Diff("CuKa2Diff","diff␣Ka1␣-␣Ka2",19.95,19.,20.);
RooRealVar CuKa2Ratio("CuKa2Ratio","ratio␣Ka1␣/␣Ka2",0.51,0.,1.);

RooGenericPdf meanCuKa2("meanCuKa2","diff␣Cu␣Ka1␣-␣Ka2␣␣PDF","meanCuKa1␣-␣
    ↪ CuKa2Diff",RooArgSet(meanCuKa1,CuKa2Diff));
RooGaussian gaussCuKa2("gaussCuKa2","Cu␣Ka2␣PDF",energy,meanCuKa2,sigmaCuKa);

RooGenericPdf cuKa2N("CuPdfRatio","ratio␣Cu␣Ka1␣/␣Ka2␣␣PDF","cuKa1N*
    ↪ CuKa2Ratio",RooArgSet(cuKa1N,CuKa2Ratio));

//NiKa1

RooRealVar meanNiKa1("meanNiKa1","mean␣of␣Ni␣Ka1␣gaussian"
    ↪ ,7478.15,7470.,7500.);
RooRealVar sigmaNiKa("sigmaNiKa","width␣of␣Ni␣Ka1␣gaussian",70.,50.,90.);
RooGaussian gaussNiKa1("gaussNiKa1","Ni␣Ka1␣PDF",energy,meanNiKa1,sigmaNiKa);

RooRealVar niKa1N("niKa1N","Nickel␣Ka1␣Events",200,0,1000);

//Nika2

RooRealVar NiKa2Diff("NiKa2Diff","diff␣Ka1␣-␣Ka2",17.26,17.,18.);
RooRealVar NiKa2Ratio("NiKa2Ratio","ratio␣Ka1␣/␣Ka2",0.51,0.,1.);

RooGenericPdf meanNiKa2("meanNiKa2","diff␣Ni␣Ka1␣-␣Ka2␣␣PDF","meanNiKa1␣-␣
    ↪ NiKa2Diff",RooArgSet(meanNiKa1,NiKa2Diff));
RooGaussian gaussNiKa2("gaussNiKa2","Cu␣Ka2␣PDF",energy,meanNiKa2,sigmaNiKa);

RooGenericPdf niKa2N("NiPdfRatio","ratio␣Ni␣Ka1␣/␣Ka2␣␣PDF","niKa1N*
    ↪ NiKa2Ratio",RooArgSet(niKa1N,NiKa2Ratio));

//Background


//the variables for the background function are defined earlier

RooChebychev backgF("backgF","Background",energy,RooArgSet(backSl));

// PEP violating tranistion
```

```
RooRealVar meanForbidden("meanForbidden","mean␣of␣the␣forbidden␣tranistion",
    ↪ 7747, 7746.,7748.);
RooGaussian gaussForbidden("gaussForbidden","Forbidden␣pdf",energy,
    ↪ meanForbidden,sigmaCuKa);

RooRealVar Nsig("Nsig","signal␣Events",10.,0.,500.);

RooAddPdf PDFtot_nuis("PDFtot_nuis","PDFtot_nuis",RooArgList(gaussCuKa1,
    ↪ gaussCuKa2,gaussNiKa1,gaussNiKa2,backgF,gaussForbidden),RooArgList(
    ↪ cuKa1N,cuKa2N,niKa1N,niKa2N,backC,Nsig));

CuKa2Diff.setConstant(kTRUE);
CuKa2Ratio.setConstant(kTRUE);
NiKa2Diff.setConstant(kTRUE);
NiKa2Ratio.setConstant(kTRUE);
meanForbidden.setConstant(kTRUE);
meanCuKa1.setConstant(kTRUE);
meanNiKa1.setConstant(kTRUE);

PDFtot_nuis.fitTo(*withAD); // fit to data with current

backC.setConstant(kFALSE);
// set Background to parameters without current
backC.setError(252.7);
backSl.setConstant(kFALSE);
backSl.setError(0.010902);

nuisW->import(PDFtot_nuis);
ModelConfig sbModel;
sbModel.SetWorkspace(*nuisW);
sbModel.SetPdf("PDFtot_nuis");
sbModel.SetName("S+B␣Model");
RooRealVar* poi = nuisW->var("Nsig");
poi->setRange(0.,500.);
sbModel.SetParametersOfInterest(*poi);
sbModel.SetNuisanceParameters(RooArgSet(backC,backSl));

nuisW->factory("Uniform::prior(Nsig)");
sbModel.SetPriorPdf(*nuisW->pdf("prior"));

//Construct the bayesian calculator
BayesianCalculator bc(*(wConst->data("withDH")), sbModel); // initialize with
    ↪  data taken with current
bc.SetConfidenceLevel(0.997);
bc.SetLeftSideTailFraction(0.);
bc.SetIntegrationType("plain");
bc.SetNumIters(10000);
// set number of iterations (i.e. number of toys for MC integrations)
bc.SetScanOfPosterior(100);
```

```
SimpleInterval* bcInt = bc.GetInterval();
RooPlot *bcPlot = bc.GetPosteriorPlot(true);
```

Curriculum Vitae

<u>Personal data:</u>

First name: Andreas
Last name: Pichler
Date of birth: 11.08.1986
Nationality: Austria
Degree: Master of Science
Contact: +43 664 4256085

<u>Education:</u>

March 2014 - Present: PhD studies at the Stefan-Meyer-Institute about the violation of the Pauli principle – in the context of the VIP project

8/2010 - 11/2013: Master studies in engineering physics at the Vienna University of Technology

- Master thesis finished with grade "A"
- Specialized in Computational Physics and Particle Physics

3/2007 - 8/2010: Bachelor studies in engineering physics at the Vienna University of Technology

- Passed with distinction
- Bachelor thesis finished with grade "A"

3/2006 - 2/2007: Studies of process engineering at the Vienna University of Technology

9/1996 - 6/2004: High school in Krems

- Finishing with A-levels (passed with distinction)
- Curriculum with special emphasis on science classes

9/1992 - 6/1996: Primary school in Krems

Programming:

C/C++, Root, Python, Matlab, LabView, Mathematica

Text processing:

Word, Latex

Languages:

English (fluent), French (basic knowledge)

Miscallaneous:

1/2012 - 6/2012: Semester abroad in Uppsala (Sweden)

2/2005 - 2/2006: Civil service at the Red Cross in Krems

9/2004: Driver's license